NATIONAL ADVISORY COMMITTEE FOR AERONAUTICS

WARTIME REPORT

ORIGINALLY ISSUED
November 1944 as
Memorandum Report L4K09

AN INVESTIGATION OF THE MUTUAL INTERFERENCE EFFECTS OF A TAIL-SURFACE - STERN PROPELLER INSTALLATION ON A MODEL SIMULATING THE DOUGLAS XB-42 EMPENNAGE

By Walter A. Bartlett, Jr., and Alfred A. Marino

Langley Memorial Aeronautical Laboratory
Langley Field, Va.

WASHINGTON

MR No. L4K09

NATIONAL ADVISORY COMMITTEE FOR AERONAUTICS

MEMORANDUM REPORT

for the

Army Air Forces, Air Technical Service Command

AN INVESTIGATION OF THE MUTUAL INTERFERENCE EFFECTS OF A TAIL-SURFACE - STERN PROPELLER INSTALLATION ON A MODEL SIMULATING THE DOUGLAS XB-42 EMPENNAGE

By Walter A. Bartlett, Jr. and Alfred A. Marino

SUMMARY

The mutual interference effects of tail surfaces and a stern propeller were investigated on a model representative of the empennage and propeller installation of the XB-42 airplane. The tests were conducted primarily to determine the effect of tail-surface - propeller spacing upon the periodic tail-surface loading coincident with propeller blade passage.

In the static-thrust condition, instantaneous pressure data were obtained at propeller blade angles of 20°, 30°, and 40° over a range of propeller rotational speeds and tail-surface - propeller spacings. The effect of blade angle, tail-surface - propeller spacing, angle of attack, and control-surface deflections on the instantaneous and average pressures on the tail surface and on propeller aerodynamic characteristics were obtained in both positive and negative dynamic thrust.

The pressure impulses on the control surfaces due to propeller blade passage were found to increase with propeller rotational speed or blade angle, or with decreased tail-surface - propeller spacing in both static and positive dynamic thrust. The effect of blade-angle change was not investigated in negative thrust, but otherwise the behavior of the pressure impulse was comparable to that in positive thrust.

Average pressure distributions obtained at two chordwise stations on the left elevator indicated that

the control-surface effectiveness increased with increasing thrust coefficient and decreased with increasing negative-thrust coefficient.

An elevator deflection of 20° decreased the envelope efficiency of the six-blade dual-rotating propeller in the low V/nD range, increased it in the high V/nD range, and only slightly affected the negative-thrust characteristics. Within the angle-of-attack range investigated, there was no change in the negative-thrust characteristics of the six-blade dual-rotating propeller.

INTRODUCTION

At the request of the Army Air Forces, Materiel Command, tests have been conducted in the propeller-research tunnel at the Langley Memorial Aeronautical Laboratory to obtain information applicable to the XB-42 airplane concerning the mutual interference effects of tail surfaces and a stern propeller. A simplified model used in this investigation simulated only the propeller and empennage arrangement of the airplane.

The Douglas XB-42 airplane is a light, midwing bomber powered by two Allison W-1710-93(E11) engines which drive a dual-rotating propeller mounted behind the tail surfaces. The propeller is made up of two three-blade units of the Curtiss 836-17C2-18 and 837-17C2-18 design, right- and left-hand, respectively. The engines, mounted side by side in the fuselage, are individually connected to the three-blade units of the propeller. It is advantageous to locate the propeller as close to the tail surfaces as possible from weight and balance considerations; in this position, however, the control surfaces experience severe instantaneous loads.

It was the primary purpose of these tests to determine the effect of tail-surface - propeller spacing on the magnitude of the periodic tail-surface loading coincident with propeller blade passage. The average pressure distributions on the elevator for various combinations of control-surface deflection and the aerodynamic characteristics of the propeller operating at both positive and negative thrust were also measured.

A previous investigation of the periodic tail-surface loadings applicable to the XB-42 airplane was presented in reference 1.

APPARATUS AND TESTS

Model.- The XB-42 tail-propeller interference model consisted of a streamline body upon which pusher propellers were mounted directly behind vertical and horizontal surfaces as shown in figure 1. The propellers were driven by two 25-horsepower motors mounted within the nacelle.

The tail surfaces were constructed of wooden spars and ribs covered with sheet aluminum. A lead weight was mounted at the tip of each surface to reduce the natural frequency of the tail surfaces. The ordinates of the tail surfaces conform to the NACA 0009 section. The mean geometric chord of the elevator was 46.6 percent of the mean geometric chord of the entire horizontal tail surface. The mean geometric chord of the rudder was 41.4 percent of the mean geometric chord of the entire vertical tail surface. It was possible to set the elevators in 5° increments from -20° to 20° and the rudders in 5° increments from -10° to 10°. Rudder and elevator angles are considered positive when the trailing edges are deflected to the left and down, respectively. The gaps between the fixed and movable tail surfaces were unsealed. The longitudinal position of the tail surfaces could be changed as shown in figure 1.

A right-hand one-blade propeller (Hamilton Standard 3155-6 design) was used in all tests in which the changes in tail-surface instantaneous pressures caused by blade passage were measured. The use of a single-blade propeller was necessary to provide adequate spacing of pressure impulses as recorded on the films. The geometric characteristics of the blade are given in figure 2, and a photograph of the propeller installed on the model for wind-tunnel tests, in figure 3.

A six-blade dual-rotating propeller was used in the investigation of the propulsive efficiency, negative-thrust characteristics, and average pressure distributions on the tail surfaces. The propeller blades were of the Hamilton Standard 3155-6 and 3156-6 design, right- and

left-hand, respectively; their geometric characteristics are given in figure 2. In all tests at positive thrust, the right-hand (front) propeller was set at even values of blade angle, while the left-hand (rear) propeller was set to absorb the same power as the front propeller at peak efficiency. In the tests at negative thrust, both propellers were set at the same blade angle. The distance between center lines of the propeller disks was approximately 10 inches. The rotational speeds of both the front and rear propellers were equal throughout the tests. A photograph of the six-blade dual-rotating propeller installed on the model is shown in figure 4.

Instrumentation.- Two methods were used to measure effect of blade passage on the loading of the tail surfaces:

1. Orifices on opposite sides of the control surfaces at the points shown in figure 1 were differentially connected to pressure cells located as close to the orifices as feasible. A pressure impulse at either orifice displaced a diaphragm of the individual cells; this movement, except for the cells attached to the trailing-edge orifices on the rudder, was relayed mechanically to the photographic recording equipment. At orifices 1, rows A and B, the diaphragm movement effected changes in the inductance of an electrical circuit and this change was recorded. Installation photographs are presented in figure 5.

2. Balsa-wood tabs mounted in each elevator were attached to the tail surfaces with dural springs upon which Baldwin Southwark type C-10 strain gages were attached. (See fig. 6.) Direct current was fed into the gages and any instantaneous pressure differential acting on the tabs effected changes in voltage across the gages. This fluctuating voltage was amplified in a Sperry amplifier and recorded on a Miller oscillograph.

To reduce the possibility of resonance error being introduced into readings taken with the instantaneous pressure measuring devices, the frequency of the impressed instantaneous pressure was held well below the resonant range of the instruments. The natural frequencies of the various instruments were 120 cycles per second for the pressure pickups and 250 cycles per second for the strain-gage (tab) installation. The natural frequency

of the tail surfaces was held to 8 cycles per second so that any pulsations due to surface vibration could be differentiated easily from the pressure impulse wave.

The frequency response of the instantaneous pressure devices was kept as high as practicable. Static orifices, 1/8 inch in diameter, were connected to the various pickup elements with $\frac{3}{16}$-inch inside-diameter tubing. The lengths of tubing used to connect the various orifices to the pickup elements were 4 feet for the trailing-edge orifices and 8 feet for all other orifices. The shorter length of tubing would tend to increase the accuracy of the trailing-edge pressure recorders as there would be less lag between the orifice and measuring device. The complete installation was calibrated for attenuation of the pressure wave by applying a known pressure at several frequencies to the installation.

The occurrence of instantaneous loads was correlated with propeller position by a timing device consisting of two stationary copper brushes riding on a steel ring which rotated with the propeller shaft. A bakelite insert in the ring caused a break in the timing circuit for each shaft revolution tripping timing solenoids in the various recording instruments.

The average chordwise pressure distributions at two spanwise stations on the left elevator were obtained by the pressure belt technique described in reference 2. The location of the pressure belts on the model is shown in figure 1; the inboard and the outboard belts were located at 52 and 82 percent of the propeller radius, respectively. A photograph of the installation is given as figure 7.

Tests.- Static thrust tests were conducted on a ground stand and measurements of thrust, power, and instantaneous pressure were obtained. Tests were run at wind speeds not exceeding 5 miles per hour. In this range, the slopes of the thrust and power curves vary directly with air velocity, permitting a simple velocity correction to the coefficients.

The dynamic thrust tests were conducted in the propeller-research tunnel at airspeeds up to 90 miles per hour. Thrust and power were measured over the

operating range of the propeller in addition to measurements of instantaneous and average pressures on the tail surfaces. The angle-of-attack range for these tests was from 5° to -10°. To minimize the effects of strut interference, larger negative than positive angles of attack were tested.

SYMBOLS

The following symbols are used in this report:

Δp	peak pressure differential, measured at static orifices, pounds per square foot, considered positive if it imparts a positive rolling moment to the model
ρ	mass density of air, slugs per cubic foot
σ	relative density ($\rho/0.002378$)
q_o	free-stream dynamic pressure, pounds per square foot
$\Delta p/q_o$	peak pressure coefficient
p	local static pressure, pounds per square foot, subscripts U and L denote upper and lower surfaces, respectively
p_o	free-stream static pressure, pounds per square foot
W_t	total peak load on tab, pounds
A_t	area of tab (0.429 square foot)
$\Delta p_t = \frac{W_t}{A_t}$	average peak pressure impulse on tab, pounds per square foot
$\Delta p_t/q_o$	peak pressure coefficient on tab
V	velocity of air stream, feet per second
T_e	effective thrust, pounds
P	power absorbed by propeller, foot-pounds per second

N	propeller rotational speed, rpm
n	propeller rotational speed, rps
R	propeller radius, feet
D	propeller diameter, feet
β	blade angle at 0.75R, degrees, subscripts F and R denote front and rear propellers, respectively
V/nD	propeller advance-diameter ratio
d	distance between point of pressure measurement and center line of the single-blade propeller, inches
α	angle of attack, vertical angle between thrust axis and air stream, degrees
δ_e	elevator deflection, degrees, trailing edge down is positive
δ_r	rudder deflection, degrees, trailing edge to left is positive
$C_T = \frac{T_e}{\rho n^2 D^4}$	thrust coefficient
$T_c = \frac{T_e}{\rho V^2 D^2}$	thrust disk loading coefficient
$C_P = \frac{P}{\rho n^3 D^5}$	power coefficient
$\eta = \frac{C_T}{C_P} \frac{V}{nD}$	propulsive efficiency

RESULTS AND DISCUSSION

The discussion of the results of the tail-propeller interference model tests dealing with the effect of the

propeller on the tail surfaces is presented in two sections dealing in turn with instantaneous pressure impulses and average tail-surface pressure distributions.

The results of tests made to determine the effect of the position of the tail-surface and control-surface deflection on the aerodynamic characteristics of a six-blade dual-rotating propeller are presented in the final section of this discussion.

A list of figures which present test results is given in table I.

Instantaneous Pressures

The aerodynamic load on a surface mounted ahead of and very close to an operating propeller may be considered in two parts: (1) a steady load which is determined by the geometry of the surface, the attitude, and average velocity in which it operates; and (2) an impulse load experienced when the surface is in the immediate proximity of the individual propeller blades. The greater part of this investigation is concerned with evaluating the second component which is caused by the sudden change in flow over the surface as the flow field about the propeller blades is superimposed on the steady flow in the free stream.

Typical pressure records, presented in figure 8, show that the surface is subjected to alternating impulses with each blade passage. The position of the blade relative to the tail surface at the occurrence of the peak pressures was obtained from strain-gage records by correlation with the timer marks impressed on film as the blade passed a known position in its revolution. The first peak pressure differential occurred when the center line of the approaching blade was approximately 15° from the trailing edge of the tail surface; the second peak occurred when the blade center line was nearly parallel to the trailing edge of the tail surface. The period of the pressure cycle, determined from strain-gage data, was found to vary from 14 to 17 percent of the propeller period. The strain-gage system was used in determining the position of the blade at the time of the maximum impulses because of its very small time lag. Records obtained in the wind-tunnel tests show that these

values were approximately independent of operating conditions.

Static-thrust tests.- Tests to determine the effects of the propeller rotational speed, tail-surface - propeller spacing, and blade angle were made at static thrust because the pressure differential between orifices on opposite sides of the surfaces would be greatest in this condition. The angle of attack was 0° and the control surfaces were locked in the neutral position.

The thrust and power coefficients at static thrust presented in figure 9 were independent of tail-surface - propeller spacings over the range of these tests.

It was observed in the typical pressure records of figure 8 that with each blade passage the tail surface experienced two impulses in opposite directions. In the static-thrust condition the first impulse was invariably greater than the second (fig. 10) and for this reason the following analysis of pressure variations at static thrust is based on the magnitude of the first impulse.

The variation of the first pressure impulse at the trailing-edge orifices on the elevator with propeller speed is shown in figure 11. From these data, taken with the tail surfaces in position 1, the following expression relating the magnitude of the impulse to the rotational speed of the propeller was obtained:

$$\sigma\Delta p = K_1 N^{1.45}$$

where the constant K_1 increases with increasing blade angle and decreases with distance from the propeller to the orifice.

The effect of tail-surface - propeller spacing upon the peak positive pressure at the orifices of rows C and D is shown in figure 12. These data were obtained at four tail-surface - propeller spacings for several blade angles and propeller rotational speeds. The peak pressure differential as a function of tail-surface - propeller spacing can be expressed as

$$\sigma\Delta p = \frac{K_2}{d^{1.82}}$$

where K_2 is dependent upon blade angle and propeller rotational speed.

Combining the above expressions we find

$$\sigma\Delta p = K_3 \frac{N^{1.45}}{d^{1.82}}$$

The value of K_3 is dependent only upon the blade angle, as shown in figure 13.

The effect of blade angle upon the peak positive pressure differential for several constant propeller rotational speeds is shown in figure 14. This figure was constructed from points taken from the faired data presented in figure 10. Figure 14 clearly shows that, for any constant rpm, $\sigma\Delta p$ increases with increasing blade angle and, likewise, with decreasing distance between the blade and the orifice.

Wind-tunnel tests in positive thrust.- The instantaneous loads in the tail surfaces were determined in the wind tunnel over a range of propeller advance-diameter ratios from 0.4 to 0 thrust at blade angles of 20°, 30°, and 40°. These tests were made at several angles of attack and control-surface deflections.

The aerodynamic characteristics of the single-blade propeller expressed in forms of C_T, C_P, and η as functions of V/nD are shown in figure 15. These data were taken with the tail in position 1, the angle of attack and control surfaces at 0°, and the propeller operating at 500 rpm.

In the wind-tunnel tests at positive thrust, as in tests at static thrust, the first pressure impulse was somewhat larger than the second. (See fig. 16.) The results of tests over the range of propeller advance-diameter ratios from 0.55 to 1.75 at $\beta = 40^\circ$ show that the variation with V/nD of the pressure impulse coefficient $\Delta p/q_o$ measured at the rearmost orifices in the elevator was independent of propeller rotational speed (fig. 17). These data were obtained with the tail in position 3, the model at 0° angle of attack, and the elevator and rudder in neutral.

The results obtained from the pressure records at all orifices are plotted against V/nD in figure 18 for $\beta = 20^\circ$, 30°, and 40°. A reversal of sign of the pressure differential as the propeller goes from positive to negative thrust is shown at the blade angles of 20° and 30°.

The peak pressure $\Delta p/q_o$ as a function of distance from the propeller is shown in figure 19. These curves were obtained from faired data of figure 18 using the pressures measured at the first and second orifices only. These data, obtained with the tail in position 1, are supplemented at $\beta = 40^\circ$ by data obtained from tests with tail in position 3 (fig. 17). Pressures recorded at the foremost orifices were neglected because of inconsistencies in the data. The peak pressure coefficients for both the inboard and outboard rows fall on a single curve, except in the case of $\beta = 40^\circ$ at values of V/nD below 1. This divergence from a single curve is probably associated with the stalling of the propeller blades.

The results obtained with the strain gages mounted integral with the tabs are presented in the form of the coefficient $\Delta p_t/q_o$ as a function of propeller advance-diameter ratio in figure 20 for $\beta = 30^\circ$. Pressure impulses on the right tab are appreciably greater than those experienced on the left tab and those measured at the adjacent orifices. Because of the wide spread in the loads recorded on the right and left tabs at $\alpha = 0^\circ$, the strain-gage data are of qualitative interest only. Qualitatively these data are in agreement with the local pressure variations recorded at the orifices which are presented in figure 18.

An investigation of the peak pressure impulse on the elevator was conducted at elevator deflections from 0° to 20° and angles of attack from 0° to -10° with the rudder in the neutral position. The results of these tests, plotted in figure 21, show the change in pressure impulse at the six orifices on the elevator as a function of V/nD for the various test conditions.

These data were taken at $\beta = 40^\circ$ with the tail in position 1; the propeller rotational speed was 500 rpm and the wind speed was varied to obtain data in

a small range of V/nD near peak efficiency of the propeller. To facilitate comparison of the curves, a composite is presented in figure 22 for constant angle of attack and in figure 23 for constant values of elevator deflection. It is observed that the magnitude of the peak pressure impulse generally increased with positive elevator deflection and decreased with increasing negative angle of attack.

Results obtained with strain gages on both right and left tabs for the above elevator deflections and angles of attack are presented in figure 24. The effect of these variables on the instantaneous loading of the tab is shown clearly in the composite curves of figures 25 and 26.

To determine the effect of rudder deflection and angle of attack on the peak pressure impulse imposed on the rudder, tests were conducted at rudder deflections of -10°, 0°, and 10° and angles of attack from 0° to -10°; the elevator was in neutral. Results of these tests, presented in figure 27, show the change in $\Delta p/q_o$ with V/nD for the six orifices on the top rudder. The curves for orifice 1 (rows A and B) indicate that the pressure coefficient increases as the rudder deflection goes from negative to neutral to positive. The curves for the remaining orifices also show that the pressure coefficient is greatest at a rudder position of 10°, but also that the pressure coefficient is greater with a rudder position of -10° than it is with the rudder in neutral. As the trend of the pressure coefficients with rudder deflection is not consistent between the six orifices on the rudder, no attempt is made to correlate the behavior of the pressure coefficients on the deflected rudder with those on the deflected elevator.

To determine the effect of rudder deflection on the loading of the elevator and the effect of elevator deflection on the loading of the rudder, tests were made at the following combinations of elevator and rudder deflections with the model at 0° angle of attack.

(a)		(b)	
Measurements on elevator		Measurements on rudder	
δ_e (deg)	δ_r (deg)	δ_e (deg)	δ_r (deg)
0	10	5	0
5	10	10	0
10	10	20	0
20	10	5	10
0	-10	10	10
5	-10	20	10
10	-10	5	-10
20	-10	10	-10
		20	-10

The pressure impulses measured at the two rearmost orifices on the elevator are shown in figure 29. The curves obtained with the rudder in neutral (fig. 22) are superimposed on the experimental points. The close agreement between the two indicates that rudder deflection has a negligible effect on the pressure impulse on the elevator. In figure 30 the results obtained from the strain-gage measurements are presented in the same manner as the pressure measurements for the same deflection conditions. The agreement here is not as good as that obtained from the pressure data.

The pressure impulses recorded on the rudder at elevator deflections outlined in the above table (part (b)) are presented in figure 31. Here, also, there is close agreement between the experimental points and the curves obtained with elevators in neutral, indicating that elevator deflection has a negligible effect on the instantaneous loading of the rudder.

Wind-tunnel tests in negative thrust.- To determine the severity of the peak pressure impulses incurred with the propeller operating as an air brake, an investigation was conducted with a blade angle of -15°. These tests were made with tail in position 1, elevators and rudders in neutral, over a limited range of angles of attack. The propeller speed was 500 rpm and the wind speed varied from 29 to 100 miles per hour. The aerodynamic

characteristics of the propeller operating under these conditions are presented in figure 32 in the form of thrust and power curves.

In negative thrust the first pressure impulse, occurring as the blade approaches the tail surface, was in the direction of motion of the propeller. The second impulse which occured immediately after the blade passed the surface was of opposite direction and was somewhat larger than the first and, for this reason, the results obtained from measurements of the second peak are presented throughout the discussion. A comparison of the two pressure peaks is presented in figure 33.

The results in the form of the nondimensional coefficient $\Delta p/q_o$ are plotted against V/nD in figure 34 for the orifices on both the horizontal and vertical tail surfaces. Examination of the curves reveals that, as in positive thrust, the peak pressure impulse decreases with distance in front of the propeller. The results obtained with the strain-gage measurements are presented in figure 35. It is observed that, although the values of $\Delta p/q_o$ in negative thrust decrease with V/nD in a manner similar to positive thrust, the actual value of the pressure impulse Δp at a constant propeller speed increases with V/nD because of the increase in blade loading with V/nD.

Average Pressure Distribution on the Left Elevator

An investigation of the effects of propeller operation on the average pressure distribution over the left elevator has been made at several control-surface deflections. These tests were conducted at an angle of attack of 0° with the tail in the most forward position. Data were taken in the propeller-removed condition and with the six-blade dual-rotating propeller operating in both the positive-and negative-thrust regions.

Wind-tunnel tests in positive thrust.- With the control surfaces neutral, the blades of the front propeller set at 20°, and those of the rear at 19.9°, the effects of power on the average pressures over the left elevator were small (fig. 36(a)). At an elevator deflection of 20°, however, increasing the thrust coefficient resulted in substantial increases in the load

on this control surface (fig. 36(b)). It is observed that the greater part of the change in loading which occurred at $\delta_e = 20^\circ$ resulted from reduction of the pressure over the upper surface of the elevator.

The effect of changes in elevator deflection with propellers removed and at the T_c corresponding to peak efficiency at $\beta_F = 40^\circ$ and $\beta_R = 39.9^\circ$ is shown in figure 37. Comparison of the curves at the various elevator angles indicates that the effectiveness of the control surfaces is appreciably greater with the propellers operating.

Variations in rudder deflection are shown in figure 38 to have effected equal changes in the pressure over the upper and lower surfaces of the elevator at $\delta_e = 0^\circ$. At $\delta_e = 20^\circ$, however, the distribution of pressure over the pressure side of the surface of the left elevator was independent of rudder angle, whereas the pressure on the suction side of the surface increased negatively with rudder angle.

Wind-tunnel tests in negative thrust.- The investigation of average pressures was also extended into the negative-thrust region of propeller operation. The tests were made with the tail surfaces in position 4, the model at an angle of attack of 0°, and all six blades of the dual-rotating propeller set at -15°. The effect of changes in thrust coefficient on the pressure distributions on the left elevator is presented in figure 39 for elevator deflections of -20°, 0°, and 20°. The marked increase in pressure indicates a substantial reduction in the dynamic pressure over the tail surface when the propeller is operating in the negative thrust region. With the control surfaces deflected, the pressure change on the suction side of the surface was much greater than that on the pressure side. The effect of positive and negative thrust on the control-surface effectiveness is presented in figure 40 for three elevator deflections. In this figure an indication of the force at the inboard belt on the left elevator was found as

$$\left(\frac{p_L - p_U}{q_o}\right) = \frac{\int_{0.169}^{1} \frac{p_L - p_U}{q_o}\, dc}{0.831}$$

where c is the percent chord of the elevator. The effectiveness of the control surfaces is increased in positive thrust and decreased in negative thrust. A reversal in control for the $\delta_e = 20^\circ$ condition occurred at a value of $T_c = -0.73$.

Propeller Characteristics

Because the efficiency of a propeller is a function of the velocity field in which it operates, the aerodynamic characteristics of the six-blade dual-rotating propeller were determined for several elevator and rudder deflections. These tests were made with the tail surfaces in position 4 simulating the tail-surface - propeller spacing proposed for the first flight airplane.

Positive dynamic thrust.- The maximum efficiency of the propeller at $\beta_F = 40^\circ$ and $\beta_R = 39.3^\circ$ is shown in figure 41 to have been increased approximately 3 percent by deflecting the elevator from the 0° to the -20° position. A composite of the propulsive efficiency curves for figure 41 is presented in figure 42.

The thrust upon which these efficiencies were based is defined as the difference between the drag of the model with power on and with the propeller removed for the same configuration; thus, any reduction in separation from the deflected surfaces influenced by the propeller will appear as increased propulsive efficiency.

A comparison of operational characteristics of the propeller at blade angles of 20°, 30°, and 40°, and elevator deflections of 0° and 20° is shown in figure 43. Efficiency envelopes for each of these conditions, given in figure 44, indicate as much as 2 percent higher efficiency when the elevator is deflected from the neutral position to 20° in the V/nD range of 1.0 to 2.2, but as much as 4 percent lower efficiency below V/nD = 1.0.

The influence of rudder deflection on the aerodynamic characteristics of the propeller (fig. 45) was negligible. A composite of the propulsive efficiency curves from figure 45 is presented in figure 46. Differences in the effect of rudder and elevator deflections on the propulsive efficiency are probably associated with differences in the ratio of the control

surface span to propeller diameter and to the fact that the lower rudder on the test setup operated in the wake of the support strut.

Negative thrust.- Data concerning the negative-thrust characteristics of the six-blade dual-rotating propeller in the negative-thrust region were also requested. The angles of attack of the model selected from data furnished by the Douglas company were -6.6°, -2.6°, and 0.4°, corresponding to angles of attack of the horizontal tail at airplane lift coefficients of approximately 0.5, 1.0, and 1.5.

Negative-thrust characteristics of the six-blade dual-rotating propeller were not affected by a change of angle of attack within the range of angles of attack tested. (See fig. 47.) The test points obtained at $\alpha = 0.4^\circ$ are plotted in figure 47 with the curve drawn through these test points common to the angles of attack of -6.6° and -2.6°.

The model was set at an angle of attack of 0° in tests to determine the effect of elevator deflections upon the negative-thrust characteristics of the six-blade dual-rotating propeller. The results of these tests, presented in figure 48, show that elevator deflections of $\pm 20^\circ$ reduce the value of C_T by not more than 3 percent at a value of $V/nD = 3.0$.

SUMMARY OF RESULTS

The results of this investigation are summarized as follows:

1. With every blade passage, the control surfaces experienced unequal pressure impulses in opposite directions. In positive thrust the first impulse imparted a positive rolling moment to the model, while in negative thrust the reverse was true.

2. Increases in blade angle or rotational speed for a given advance ratio and decreases in tail-surface - propeller spacing increased the pressure impulse coefficients on the tail surfaces in positive dynamic thrust and, to a greater degree, in static thrust.

3. Deflecting the control surface away from the advancing blade increased the pressure impulse coefficient on the elevator.

4. The pressure impulse coefficient on the elevator decreased with increasing negative angle of attack.

5. In negative thrust, the peak instantaneous pressure on the tail surfaces increased with propeller advance-diameter ratio and decreased with increasing tail-surface - propeller spacing.

6. The control-surface effectiveness increased with positive propeller thrust.

7. The resultant loading on the left elevator at $\delta_e = 0^\circ$ was independent of rudder angle. With the elevators deflected 20°, the distribution on the pressure surface of the left elevator was independent of rudder angle while the pressure on the suction side of the surface increased negatively with increasing rudder angle.

8. The effectiveness of the control surfaces was considerably reduced in the negative-thrust condition, and at a value of T_c, which might be encountered in using the propeller as a brake in landing, a reversal in control was indicated.

9. The envelope efficiency of the six-blade dual-rotating propeller decreased as much as 4 percent when the elevator is deflected from the neutral position to 20° in the low V/nD range and increased as much as 2 percent in the high V/nD range.

10. A 3-percent increase in the peak propulsive efficiency of the six-blade dual-rotating propeller was realized when the elevator was deflected from the neutral position to -20° for the blade settings of $\beta_F = 40^\circ$, $\beta_R = 39.3^\circ$.

11. The negative-thrust characteristics of the six-blade dual-rotating propeller were not affected by changes in angle of attack within the range of these tests but were affected slightly by deflection of the elevators.

Langley Memorial Aeronautical Laboratory
National Advisory Committee for Aeronautics
Langley Field, Va., November 9, 1944

REFERENCES

1. Laschever, N. L., and Strickland, John T.: Vibration and Strain Measurements in the A-17 Airplane as Set up in the Whirl Rig to Simulate the XA-42 Airplane. Confidential Memo. Rep. No. ENG-51-584-1, Materiel Command, Army Air Forces, Nov. 15, 1943.

2. Corson, Blake W., Jr.: The Belt Method for Measuring Pressure Distribution. NACA RB, Feb. 1943.

TABLE I.- TABLE OF TEST RESULT FIGURES

Figure	Thrust	No. of blades	Type of curve	Ordinate	Variables							Comments
					d	β	N	$\frac{V}{nD}$	α	δ_e	δ_r	
9	Static	1	Test data	Propeller characteristics	X	X						
10 to 11	---do.--	1	-----do.-----	Peak pressures		X	X					
12	---do.--	1	-----do.-----	------do.------	X	X						
13	---do.--	1	Constants			X						
14	---do.--	1	Comparison	Peak pressures	X	X	X					
15	Positive dynamic	1	Test data	Propeller characteristics		X		X				
16	---do.--	1	-----do.-----	Peak pressure coefficient		X		X				Magnitude of first and second peaks
17	---do.--	1	-----do.-----	------do.------			X					
18 to 20	---do.--	1	-----do.-----	Peak pressure coefficient	X	X		X				
21 to 26	---do.--	1	Test data and comparison	------do.------				X	X	X		Effect of α and δ_e on elevator peak pressures
27 to 28	---do.--	1	-----do.-----	------do.------				X	X		X	Effect of α and δ_r on peak pressures on rudder
29 to 30	---do.--	1	-----do.-----	------do.------				X		X	X	Effect of combinations of δ_e and δ_r on peak pressures on elevator

TABLE I.- Concluded

Figure	Thrust	No. of blades	Type of curve	Ordinate	Variables							Comments
					d	β	N	$\frac{V}{nD}$	α	δ_e	δ_r	
31	Positive dynamic	1	Test data and comparison	Peak pressure coefficient				X		X	X	Effect of combination of δ_e and δ_r on peak pressures on rudder
32	Negative dynamic	1	-----do.-----	Propeller characteristics				X	X			
33	---do.---	1	Test data	Peak pressure coefficient				X				Magnitudes of first and second peaks
34 to 35	---do.--	1	-----do.-----	------do.------				X	X			
36 to 38	Positive dynamic	6	Test data and comparison	Average pressures		X		X		X	X	
39	Negative dynamic	6	Test data	------do.------				X		X		
40	Positive and negative dynamic	6	Comparison	Integrated average pressures						X		
41 to 42	Positive dynamic	6	Test data and comparison	Propeller characteristics				X		X		
43 to 44	---do.--	6	-----do.-----	------do.------		X		X		X		
45 to 46	---do.--	6	-----do.-----	-----do.------		X		X			X	
47	Negative dynamic	6	Test data	-----do.------				X	X			
48	---do.--	6	Test data and comparison	-----do.------				X		X		

NATIONAL ADVISORY COMMITTEE FOR AERONAUTICS

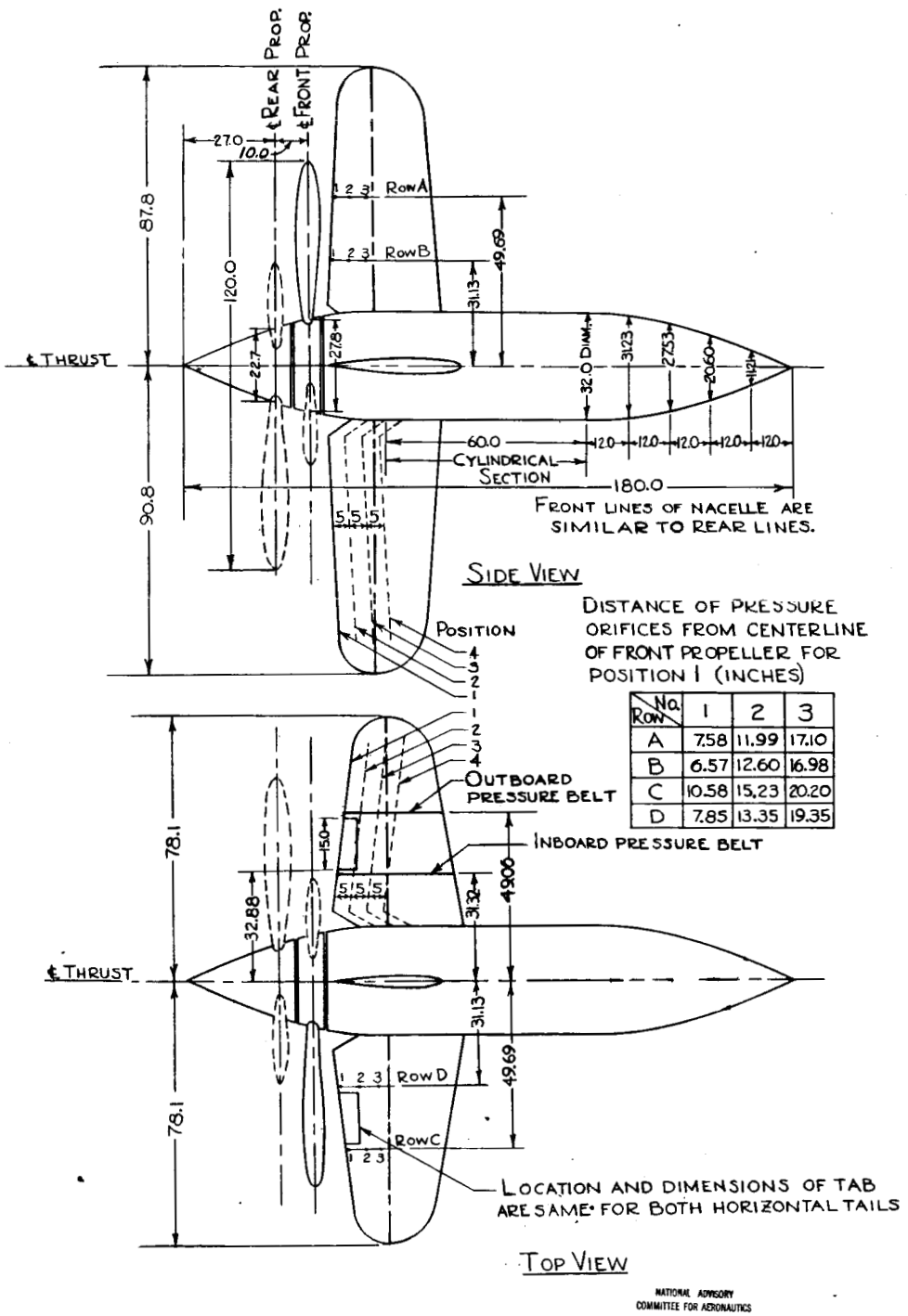

Row \ No.	1	2	3
A	7.58	11.99	17.10
B	6.57	12.60	16.98
C	10.58	15.23	20.20
D	7.85	13.35	19.35

Figure 1.- General arrangement of the XB-42 tail surface-propeller interference model showing orifice and tab locations.

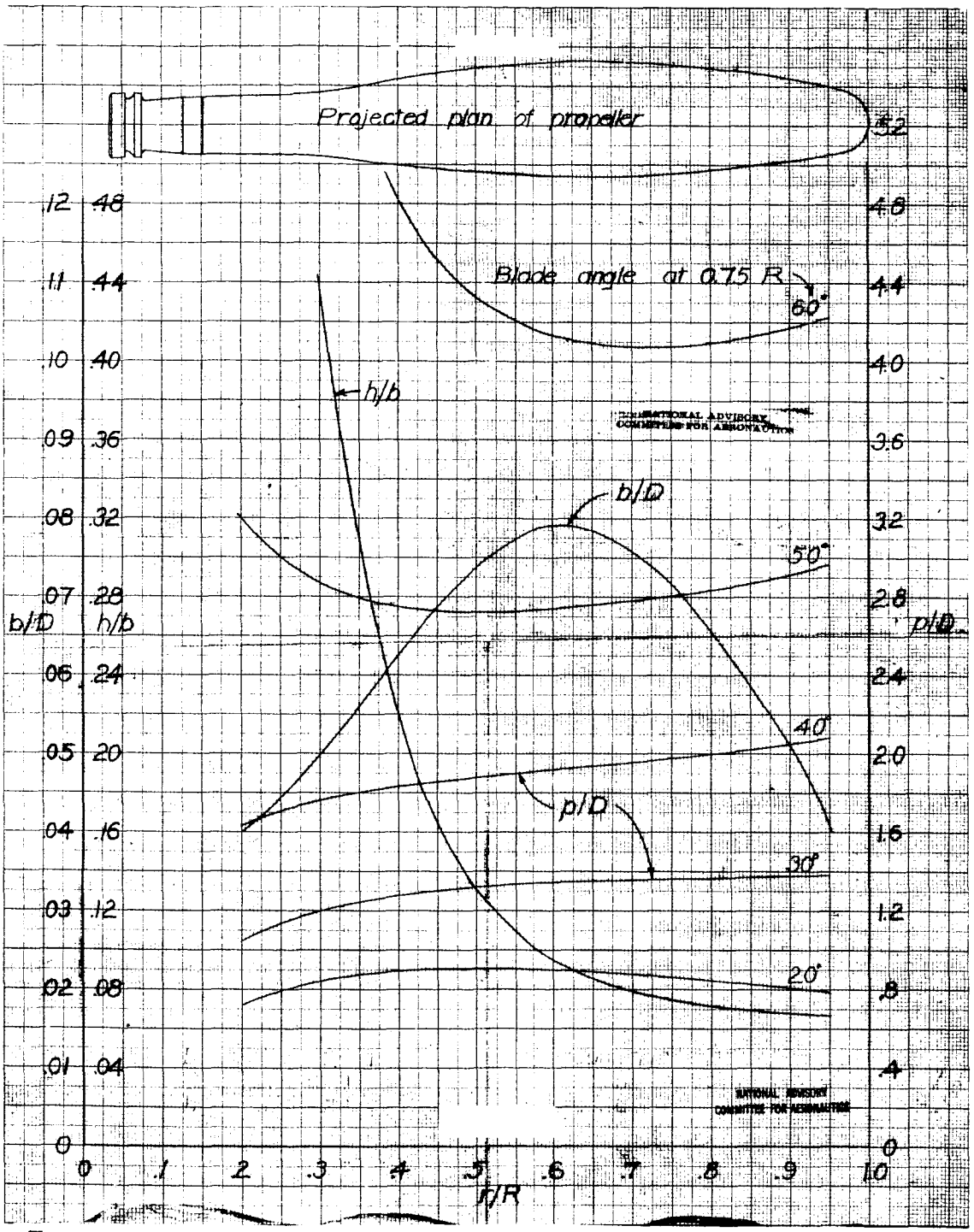

Figure 2.- Plan-form and blade-form curves for propellers 3155-6 (right hand) and 3156-6 (left hand) D, diameter; R, radius to the tip; r, station radius; b, section chord, h, section thickness; p, geometric pitch.

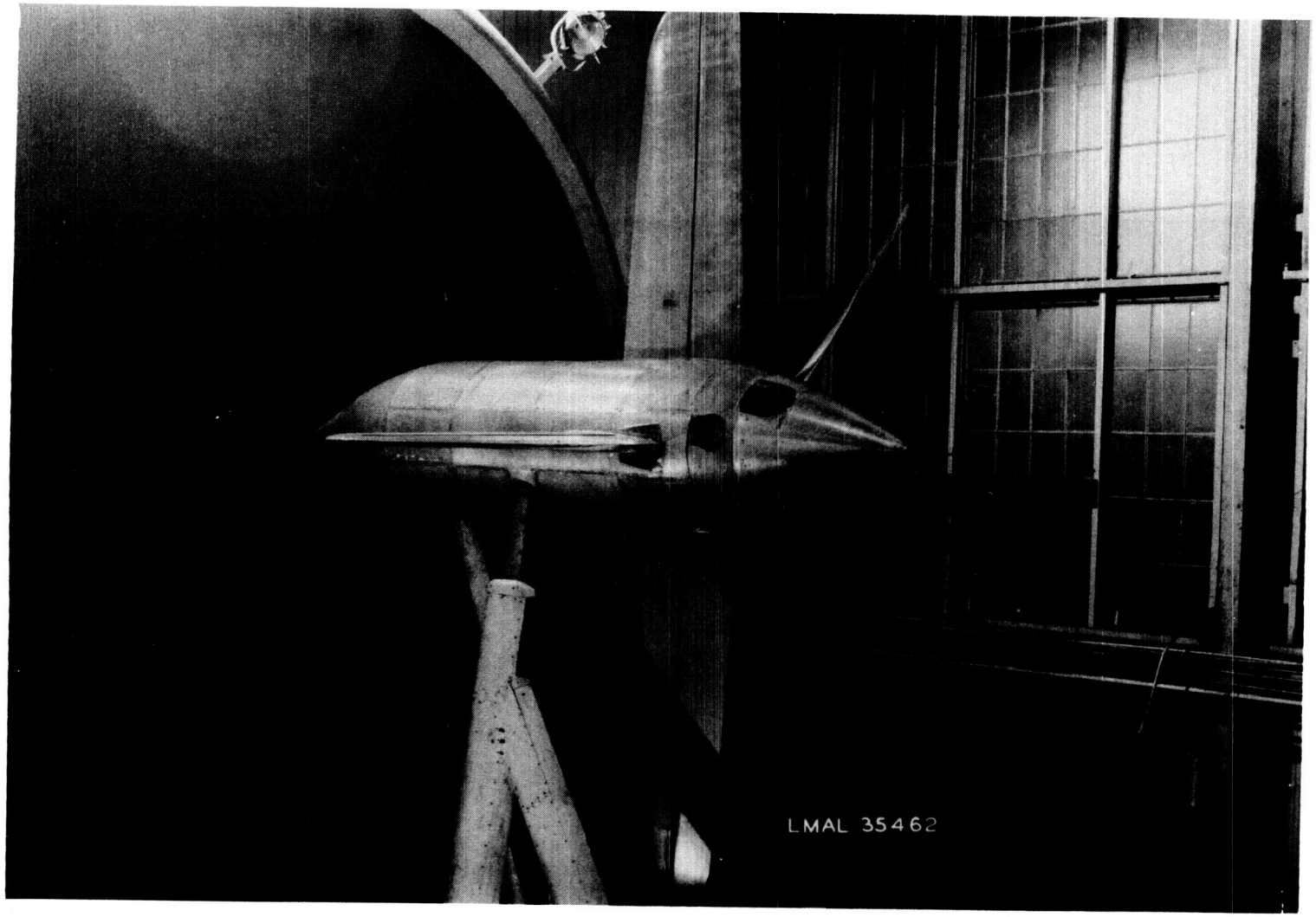

Figure 3.- The one-blade propeller installed on the tail surface-propeller interference model. Tail surfaces in position 1; $\beta = 40^{\circ}$; $\alpha = 0^{\circ}$; $\delta_e = 0^{\circ}$; $\delta_r = 0^{\circ}$.

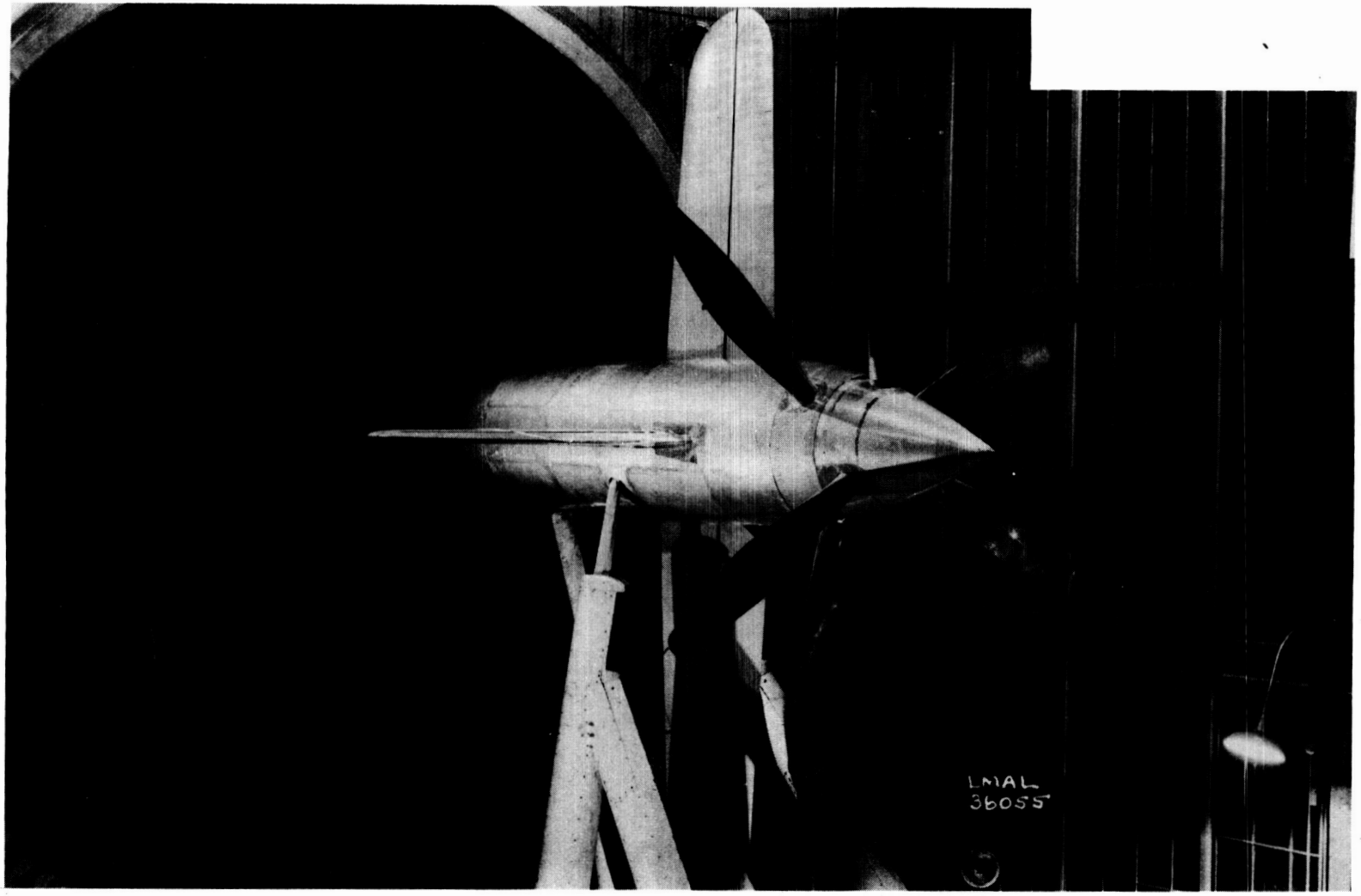

Figure 4.- The six-blade dual-rotating propeller installed on the tail surface-propeller interference model. Tail surfaces in position 4; $\beta_F = \beta_R = -15^\circ$; $\alpha = 0^\circ$; $\delta_e = 0^\circ$; $\delta_r = 0^\circ$.

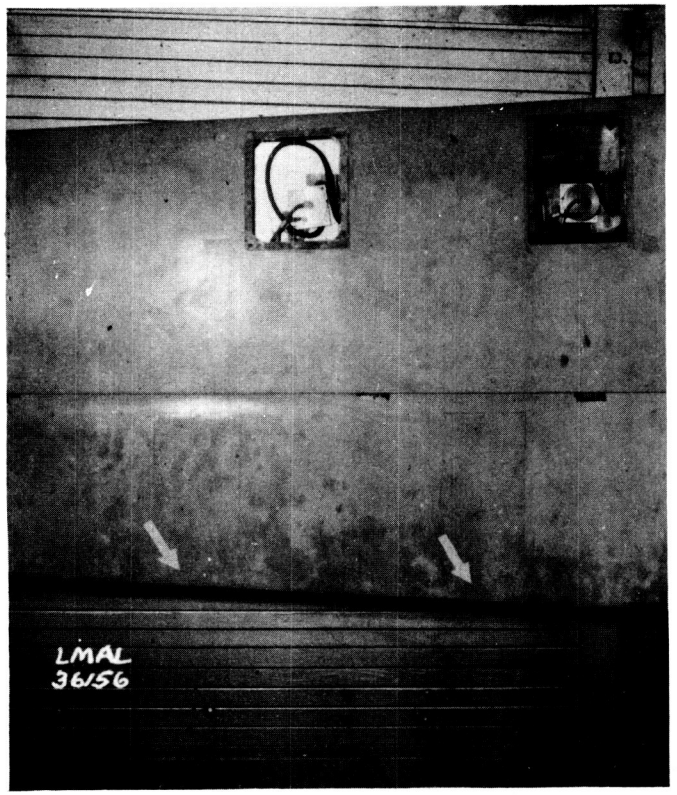

(a) Electrical pressure pick-ups; Top rudder.

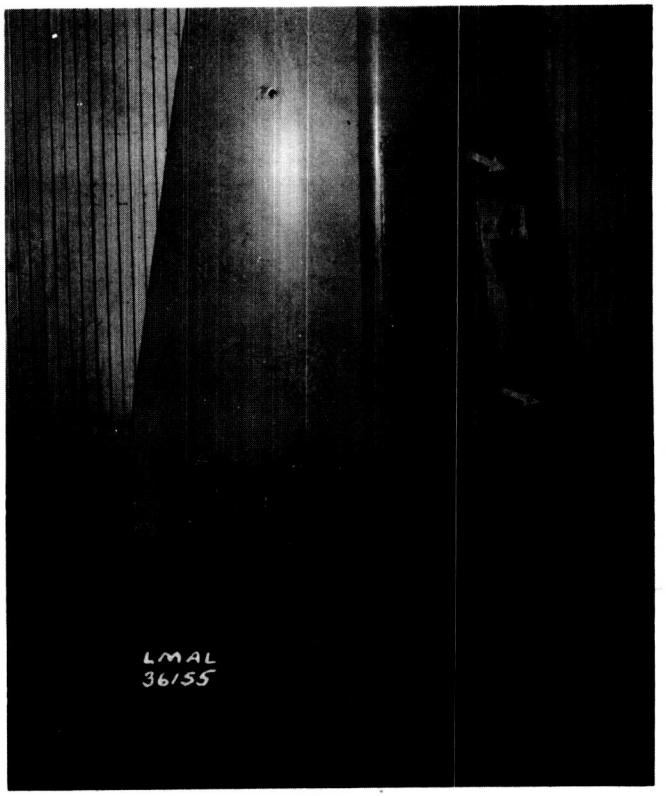

(b) Single capsule recorders; Right elevator.

Figure 5.- The instantaneous pressure measuring devices installed in the tail surfaces with arrows pointing to the connecting trailing edge orifices.

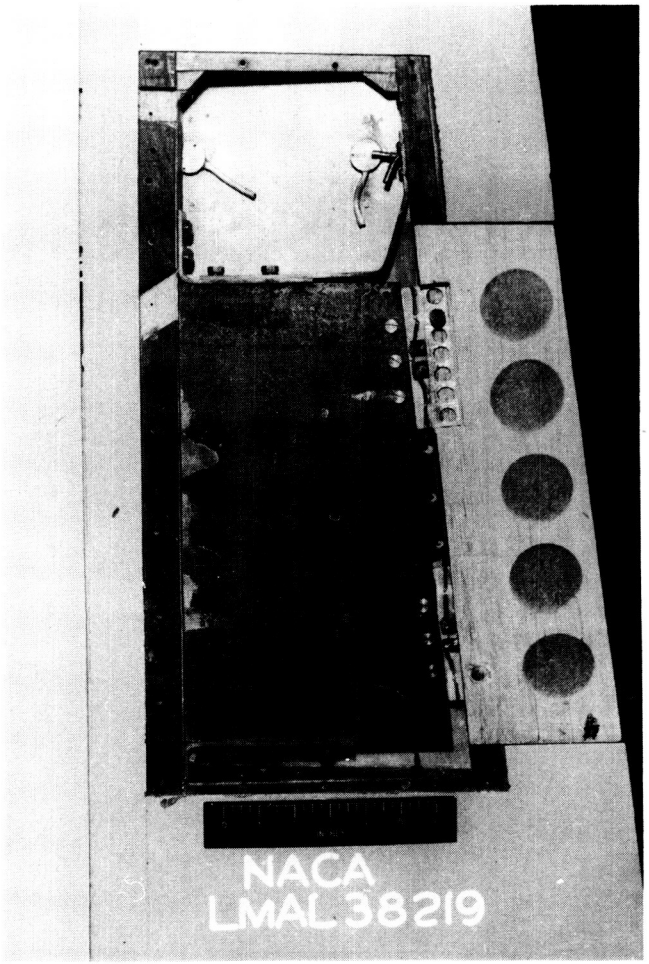

Figure 6.- The balsa wood tab installation in the left elevator with tab cut open to show details of spring.

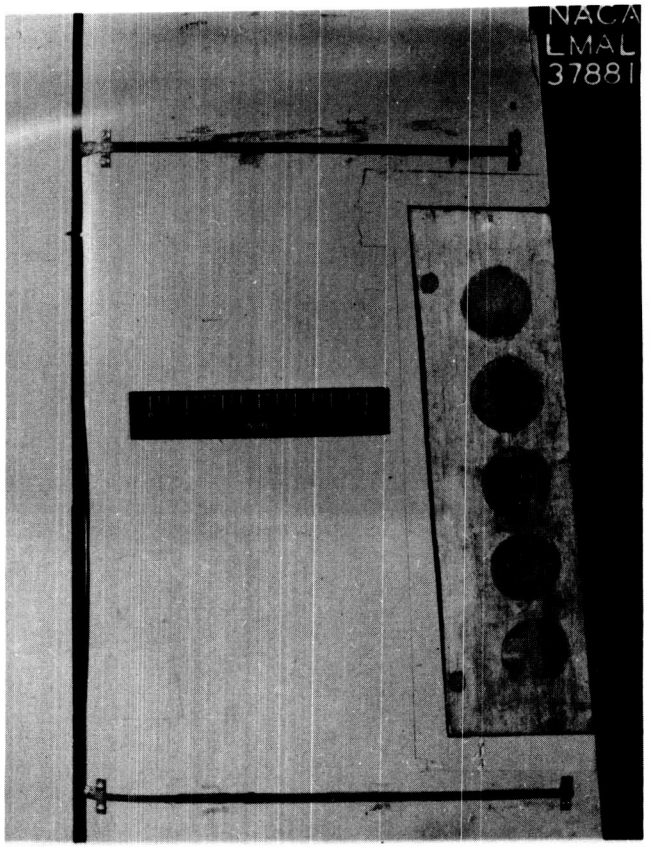

Figure 7.- Pressure belt installation on the lower surface of the left elevator.

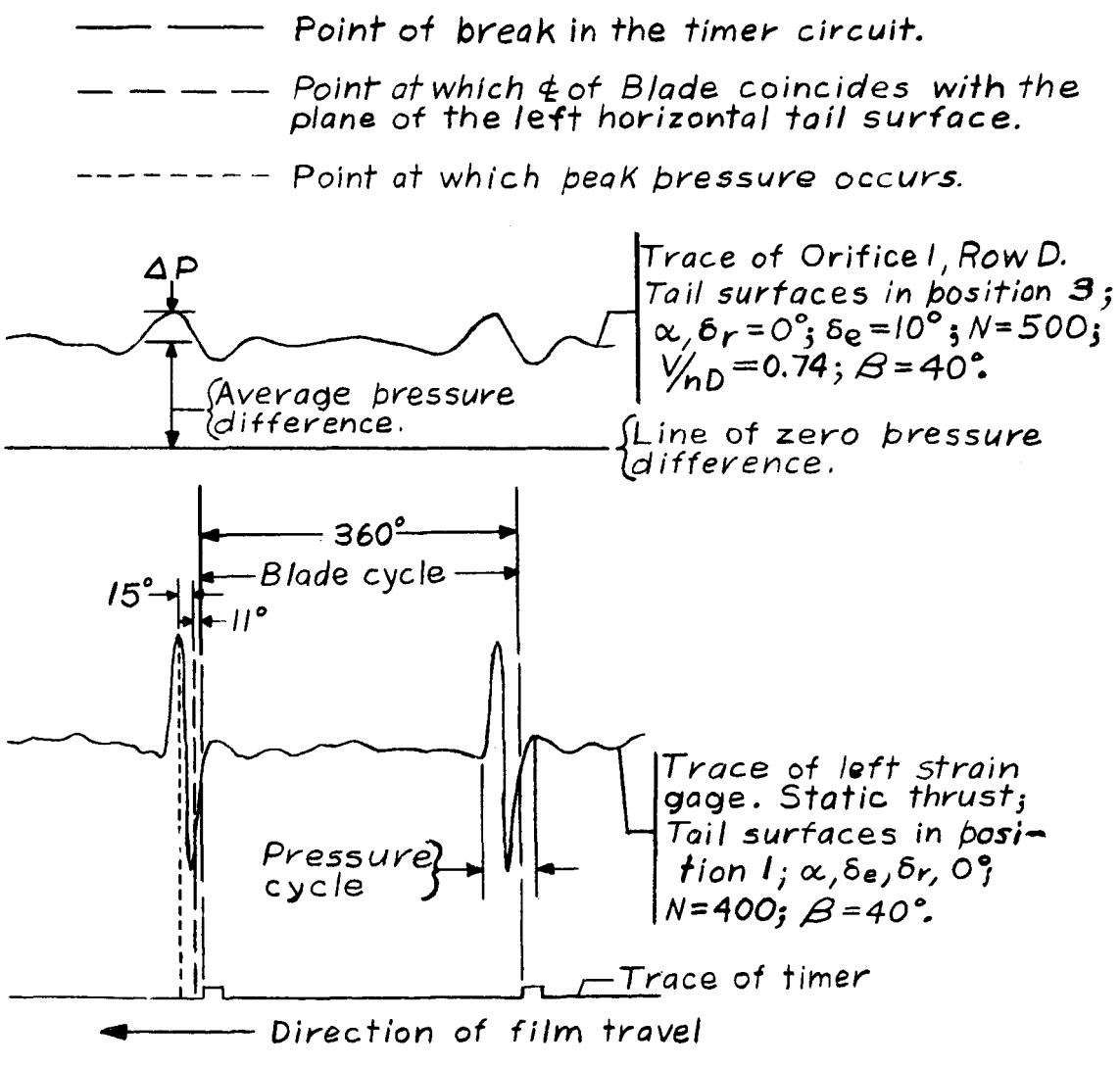

NATIONAL ADVISORY
COMMITTEE FOR AERONAUTICS

Figure 8.- Typical test records showing the correlation of the pressure peaks with blade position.

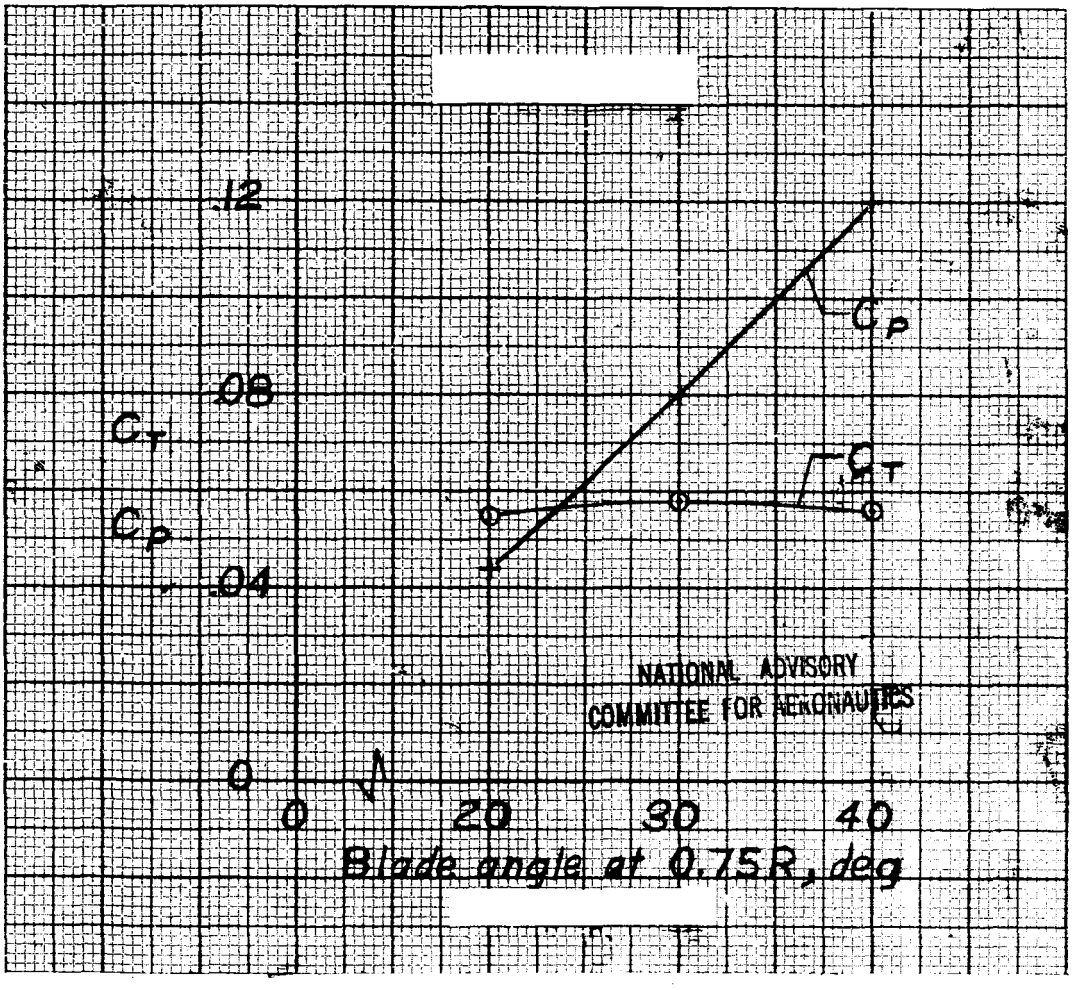

Figure 9.- Static-thrust characteristics of the one-bladed propeller. All tail surface positions; $\alpha = 0^\circ$; $\delta_e = 0^\circ$; $\delta_r = 0^\circ$.

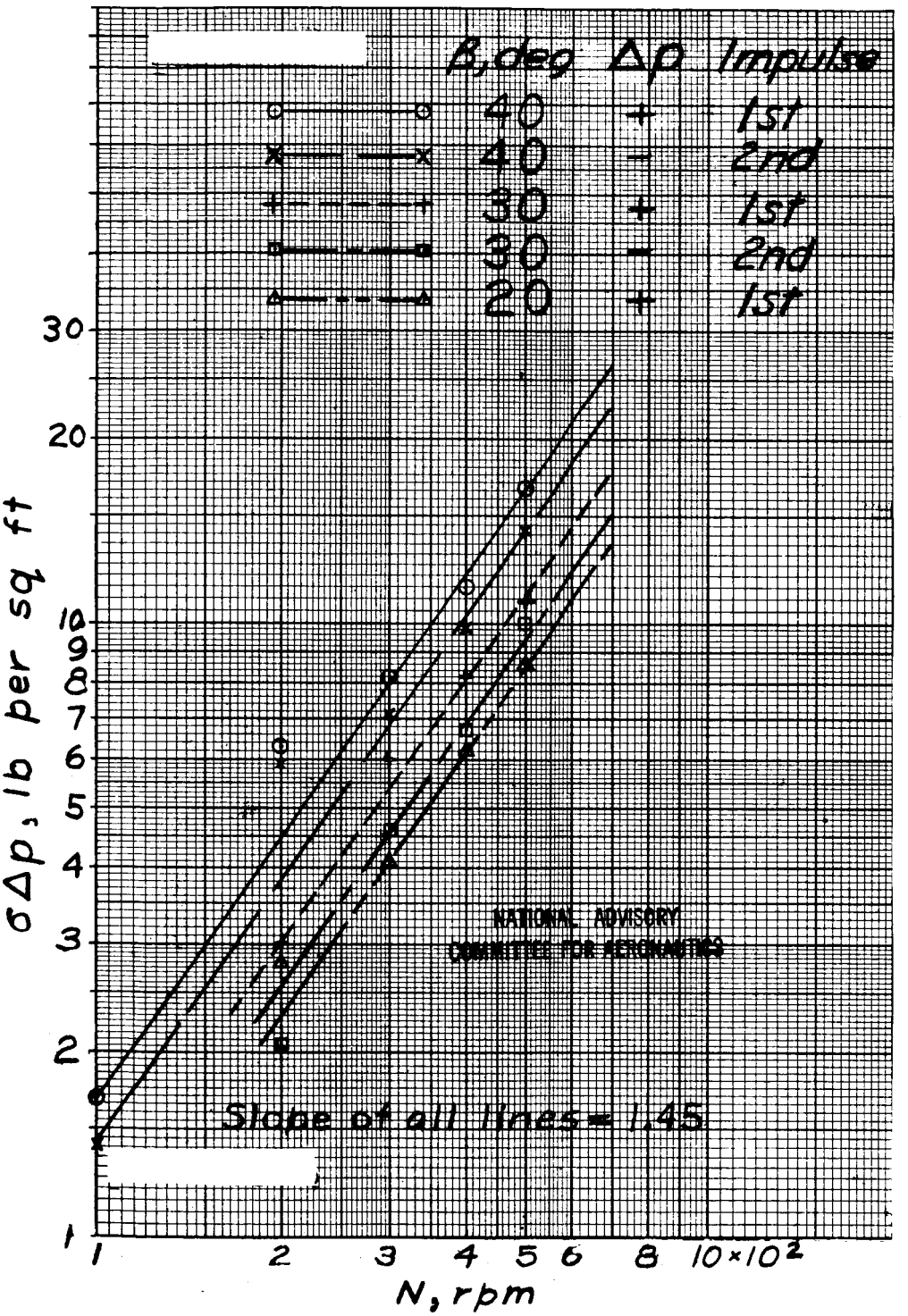

Figure 10.- A comparison of the magnitudes of the first and second pressure impulse at static thrust. Tail surfaces in position 1; $\alpha = 0^{\circ}$; $\delta_e = 0^{\circ}$; $\delta_r = 0^{\circ}$.

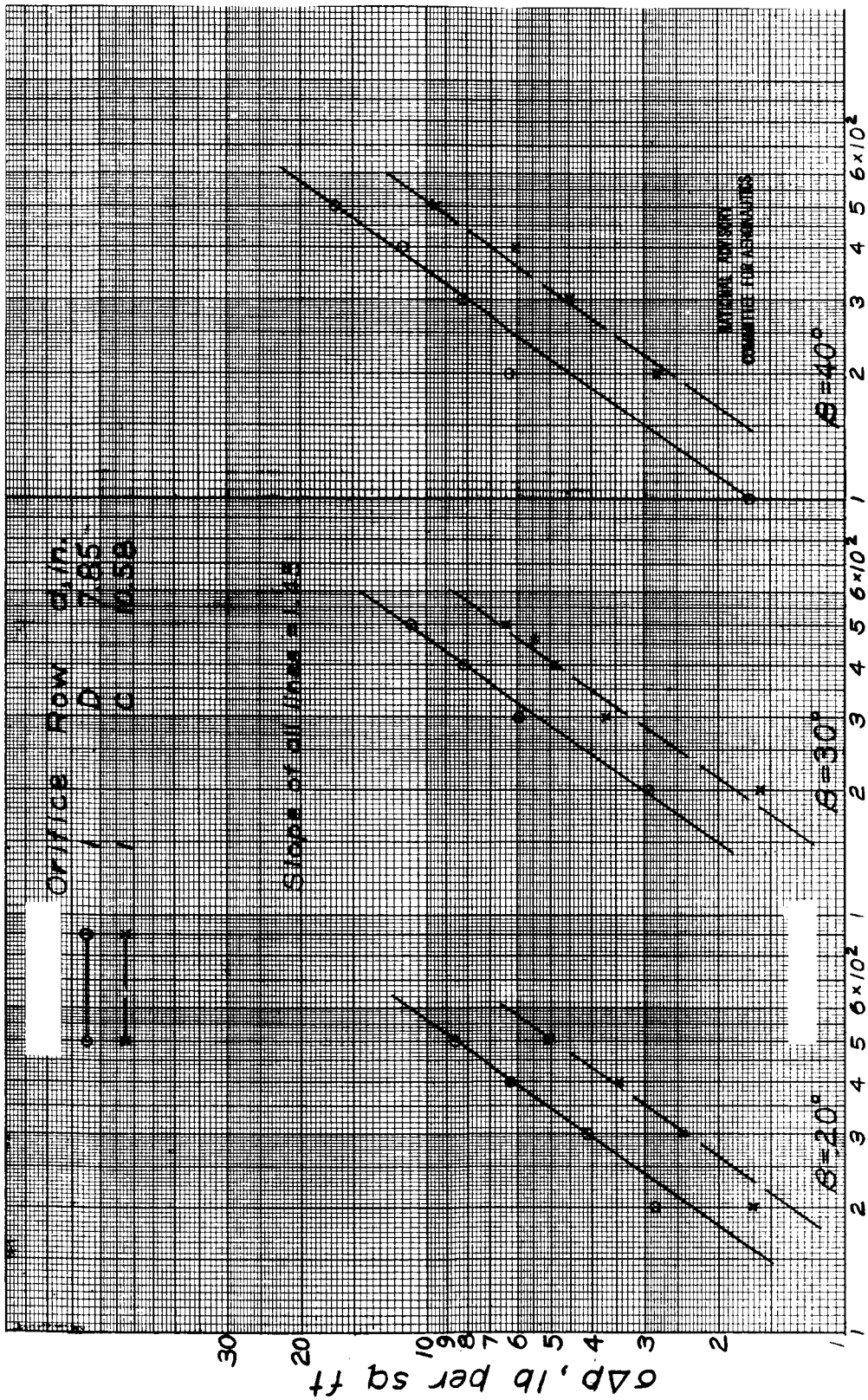

Figure 11.- The effect of propeller rotational speed on the peak pressure differential on the right elevator in static thrust. Tail surfaces in position 1; $\alpha = 0^{\circ}$; $\delta_e = 0^{\circ}$; $\delta_r = 0^{\circ}$.

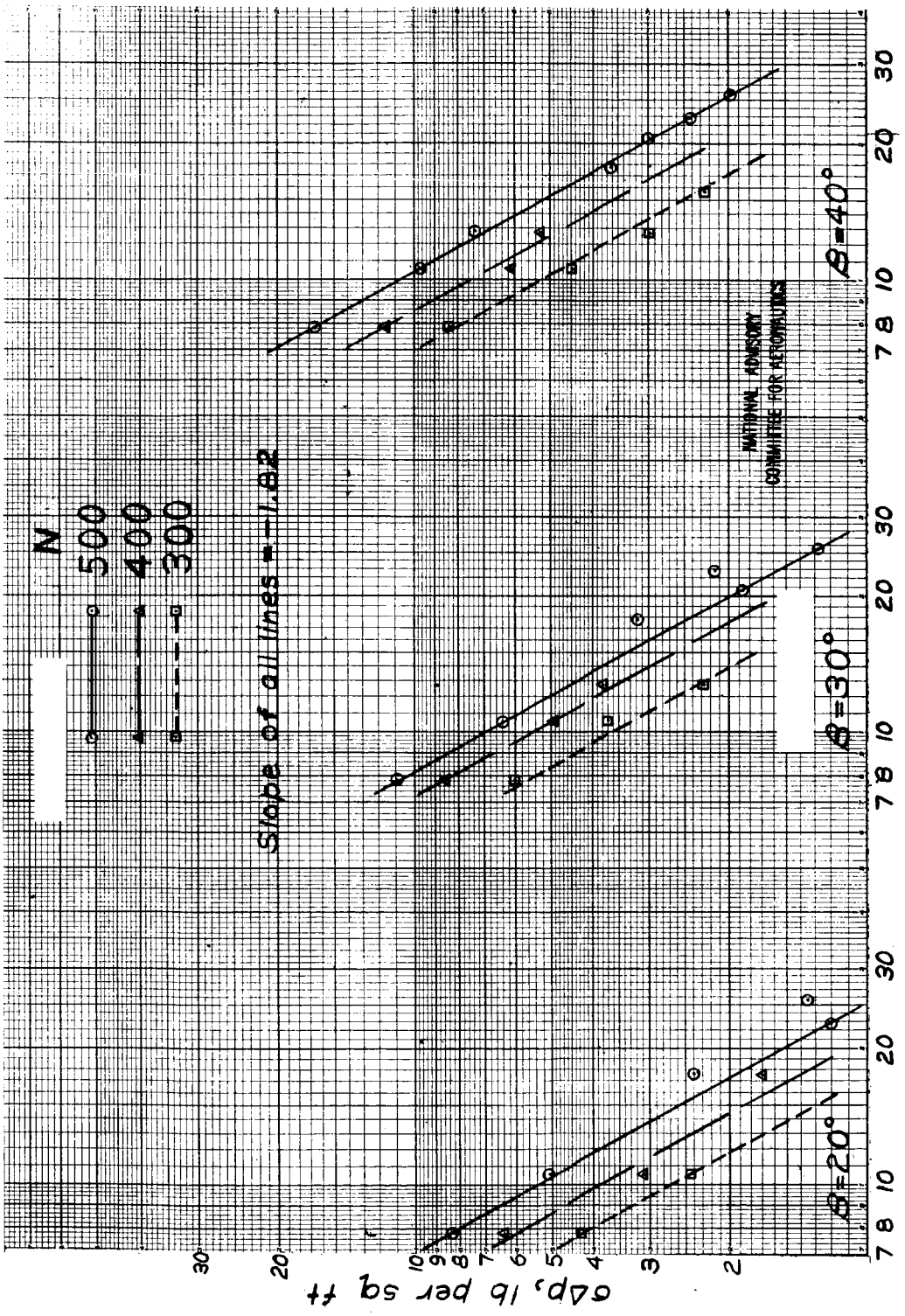

Figure 12.- The effect of tail surface-propeller spacing on the peak pressure differential on the right elevator in static thrust. $\alpha = 0^{\circ}$; $\delta_e = 0^{\circ}$; $\delta_r = 0^{\circ}$.

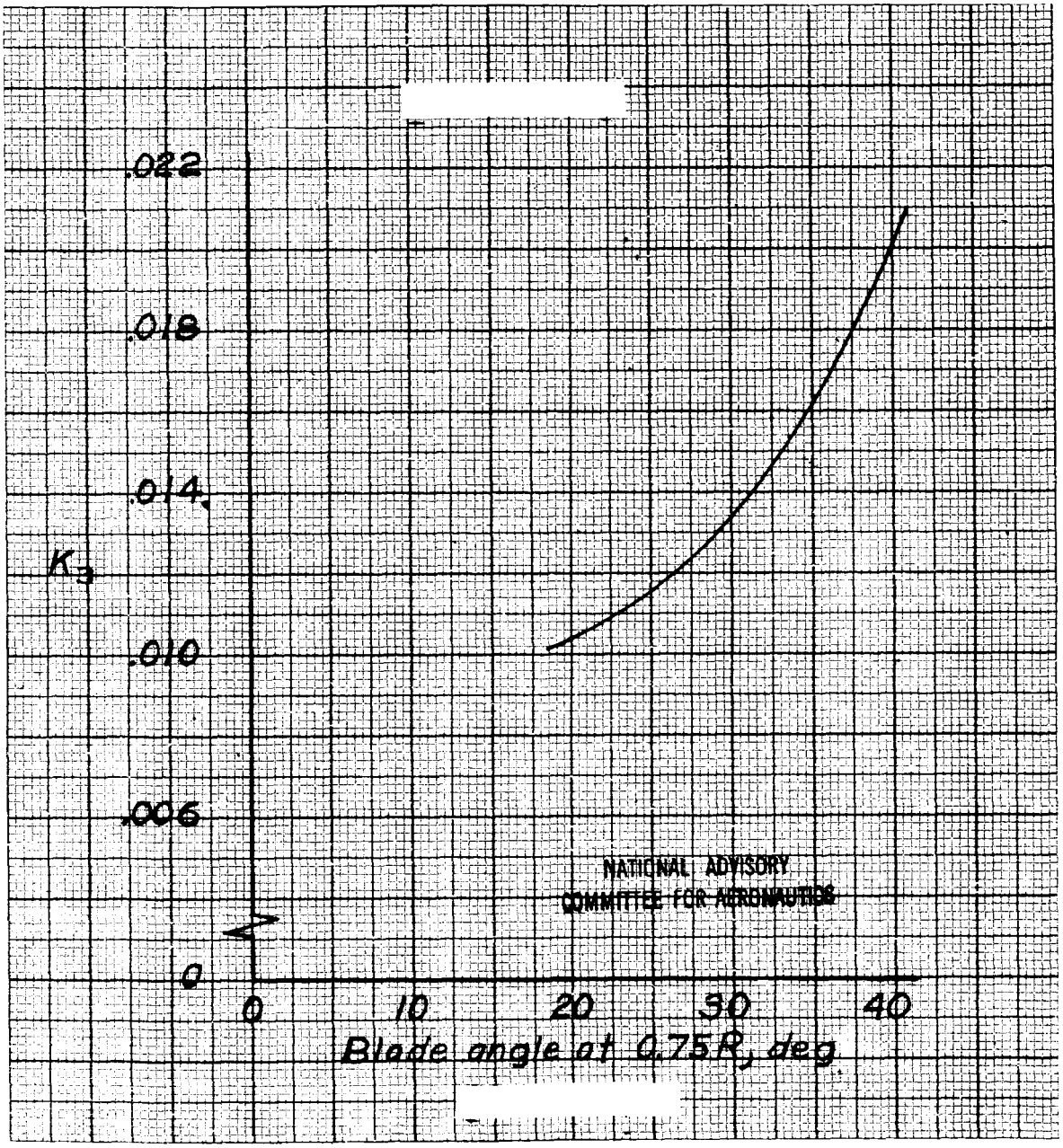

Figure 13.- Values of K_3 computed from static-thrust results.

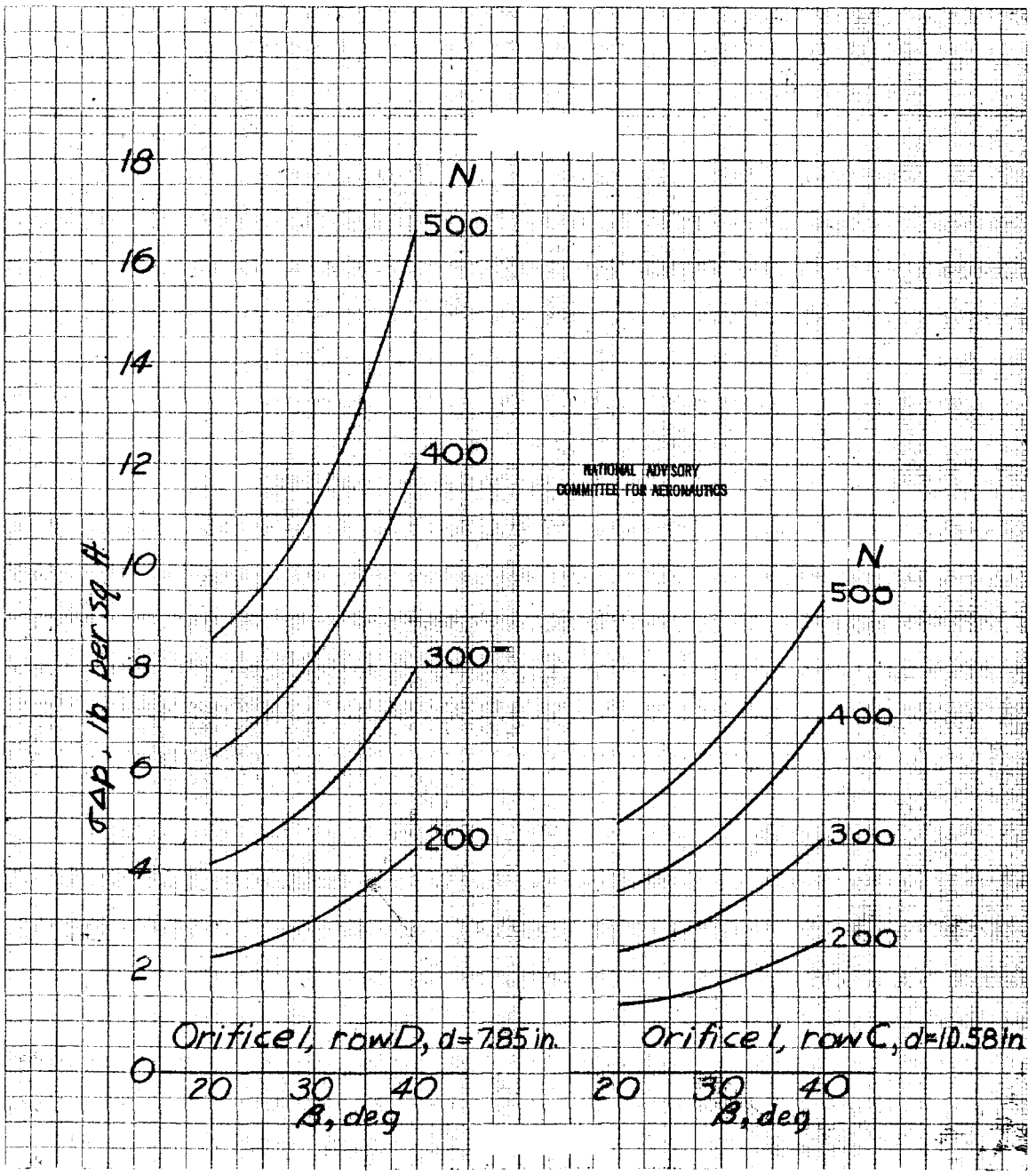

Figure 14.- The peak positive pressure differential on the horizontal elevator as a function of β for constant values of propeller-rotational speed. Tail surfaces in position 1; $\alpha = 0^{\circ}$; $\delta_e = 0^{\circ}$; $\delta_r = 0^{\circ}$.

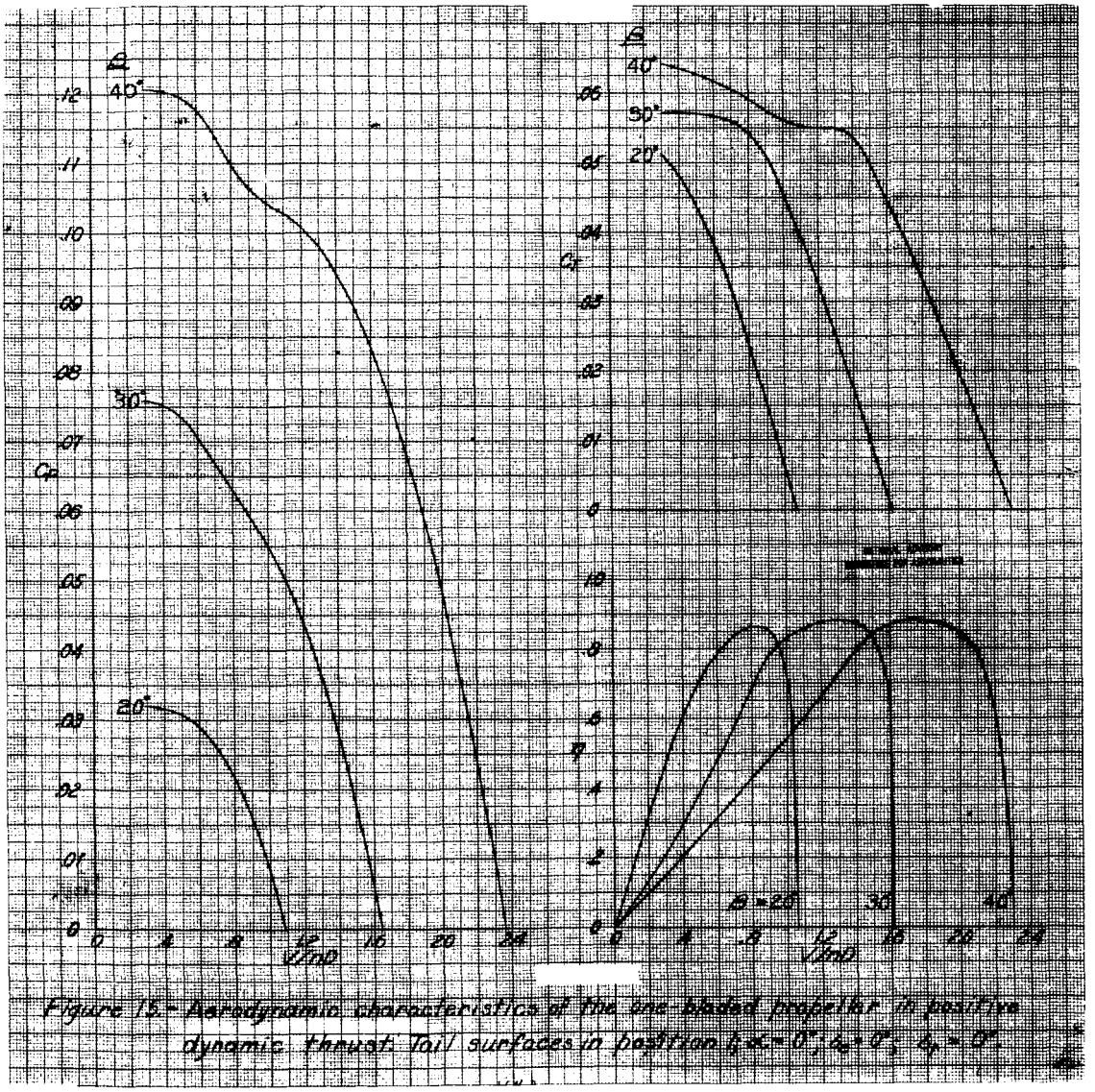

Figure 15.- Aerodynamic characteristics of the one-bladed propeller in positive dynamic thrust. Tail surfaces in position $i_t = 0°$; $\delta_e = 0°$; $\delta_r = 0°$.

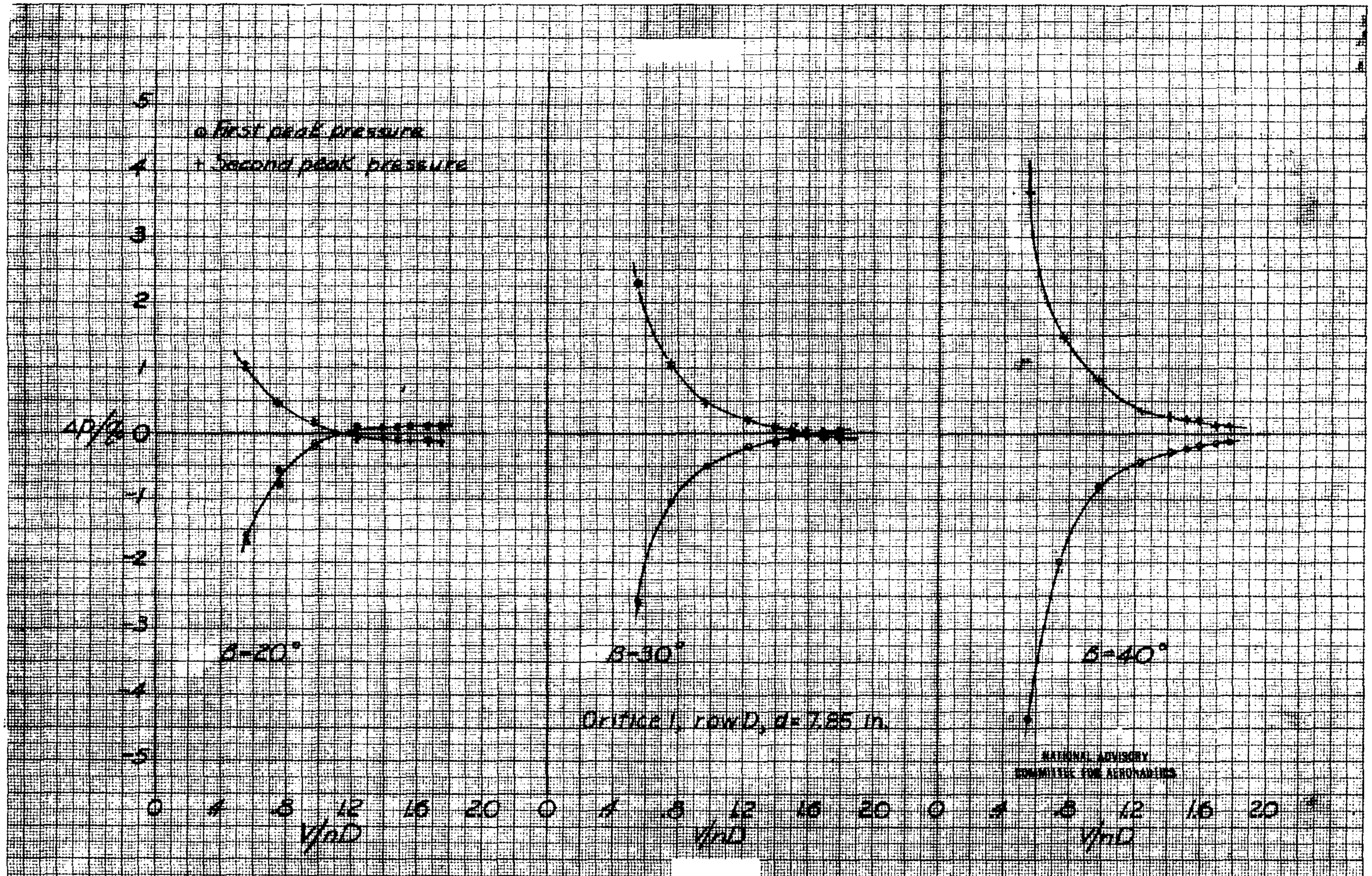

Figure 15 - Representative curves showing the relative magnitudes of the first and second pressure impulse. Tail surfaces in position 1; $\beta = 40^\circ$; $\alpha = 0^\circ$; $\delta_e = 0^\circ$; $\delta_r = 0^\circ$.

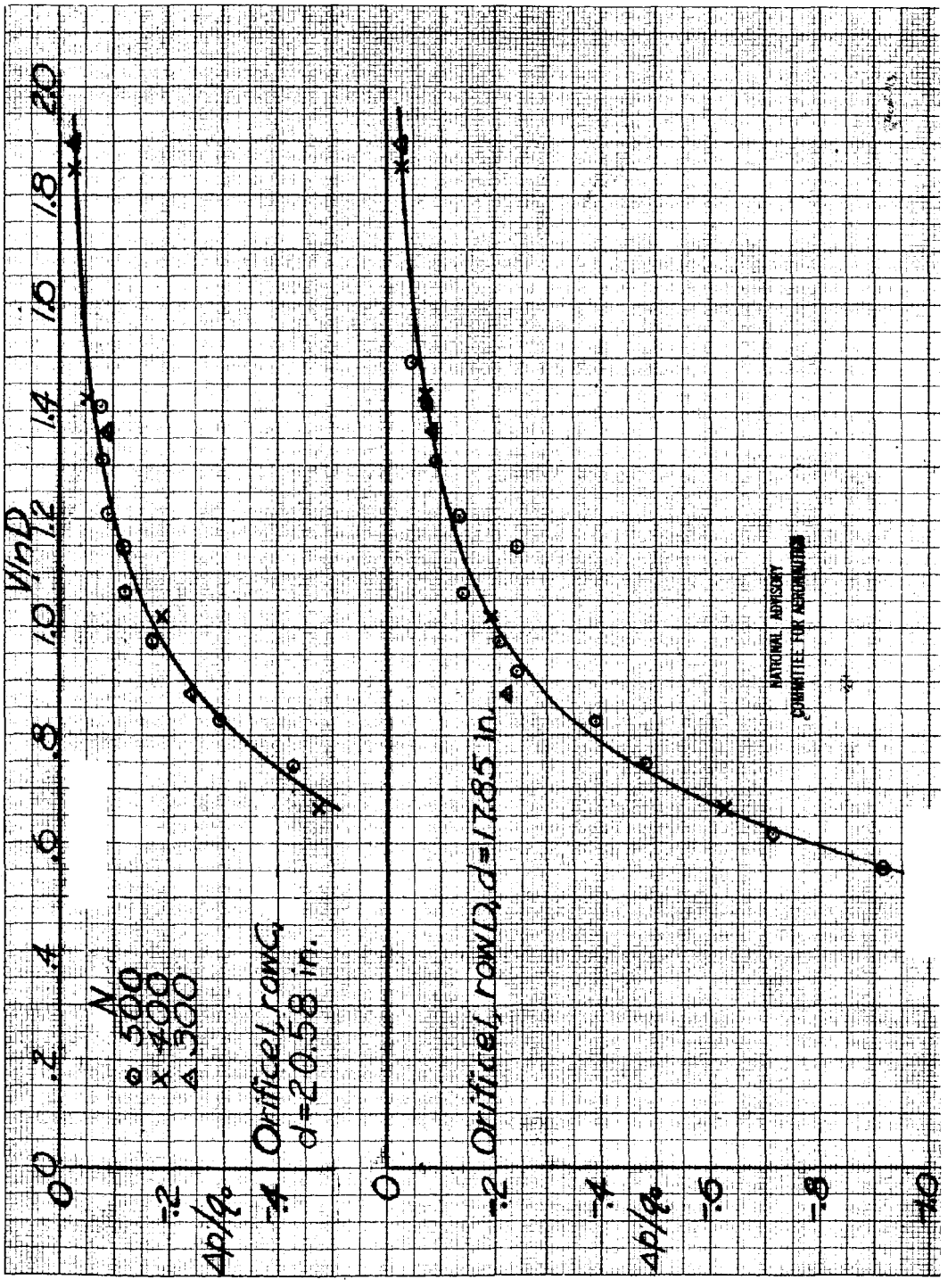

Figure 17.- Peak pressure coefficients as a function of V/nD at several propeller-rotational speeds. Tail surfaces in position 3; $\beta = 40^{\circ}$; $\alpha = 0^{\circ}$; $\delta_e = 0^{\circ}$; $\delta_r = 0^{\circ}$.

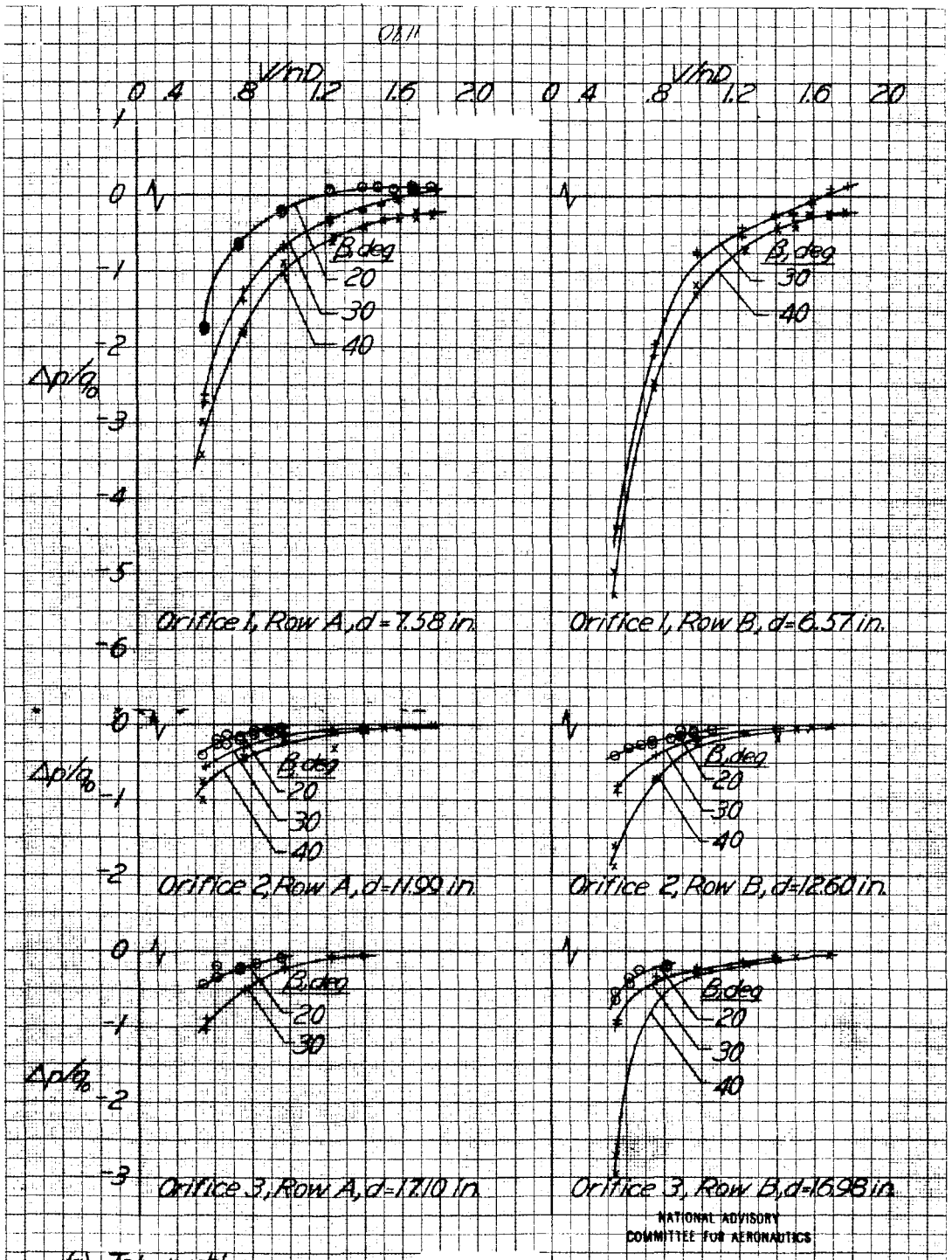

(a) Top rudder.

Figure 18.- Peak pressure coefficients on the control surfaces as affected by blade angle. Tail surfaces in position 1; $\alpha = 0°$; $\delta_e = 0°$; $\delta_r = 0°$.

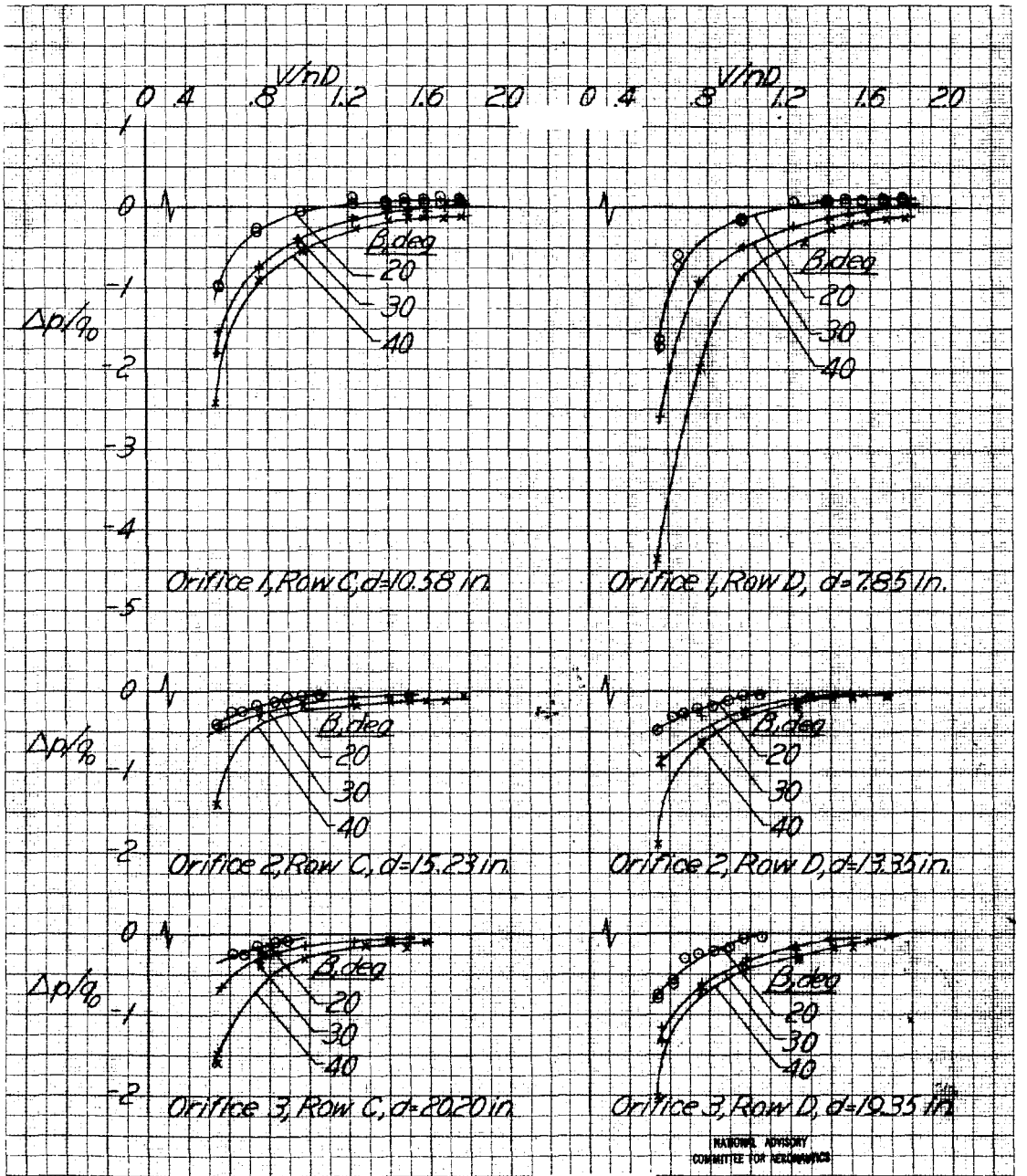

(b) Right elevator.

Figure 18.- Concluded.

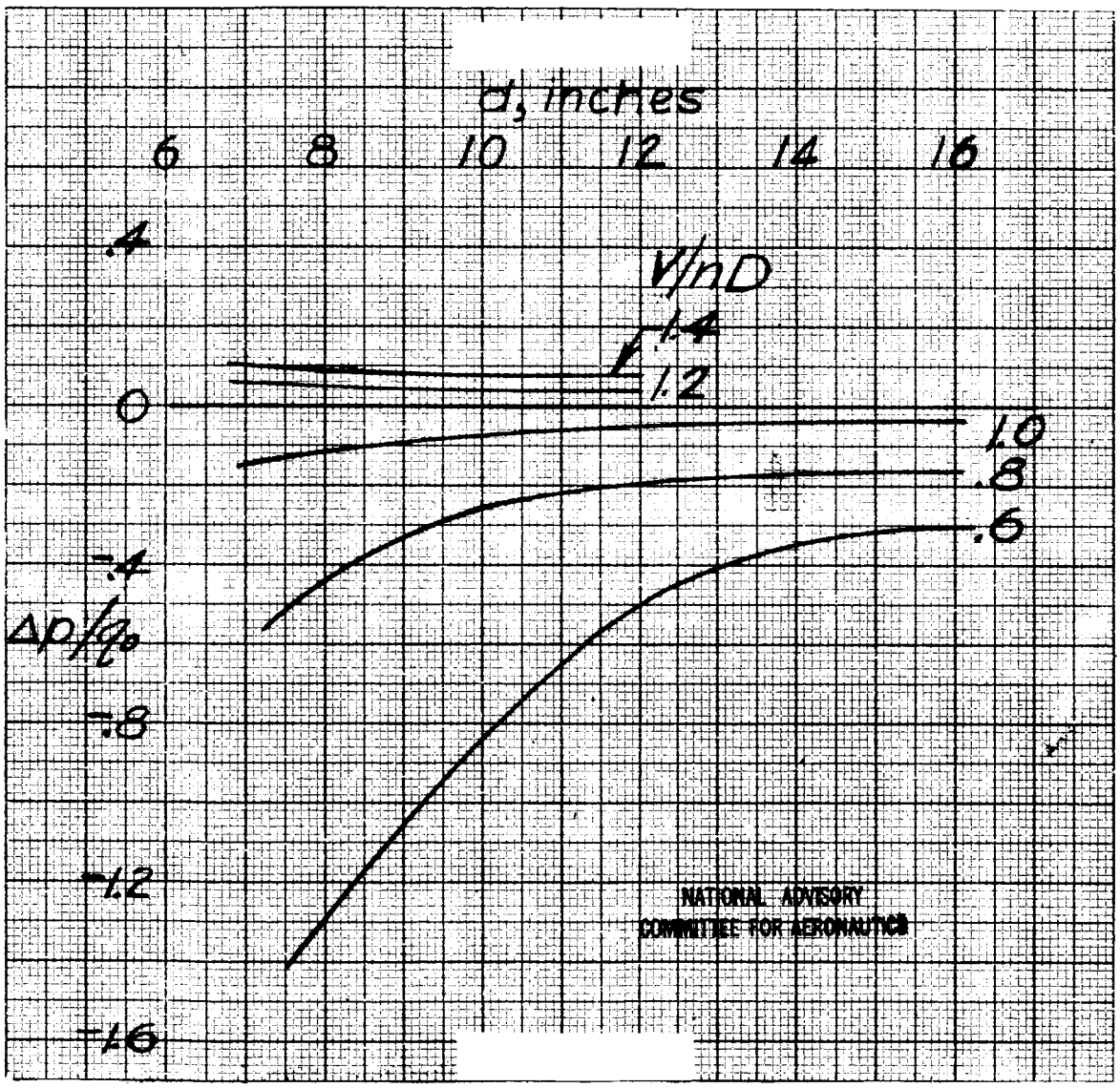

(a) $\beta = 20^{\circ}$.

Figure 19.- Variation of the peak pressure coefficient with distance from the propeller for constant values of V/nD. $\alpha = 0^{\circ}$; $\delta_e = 0^{\circ}$; $\delta_r = 0^{\circ}$.

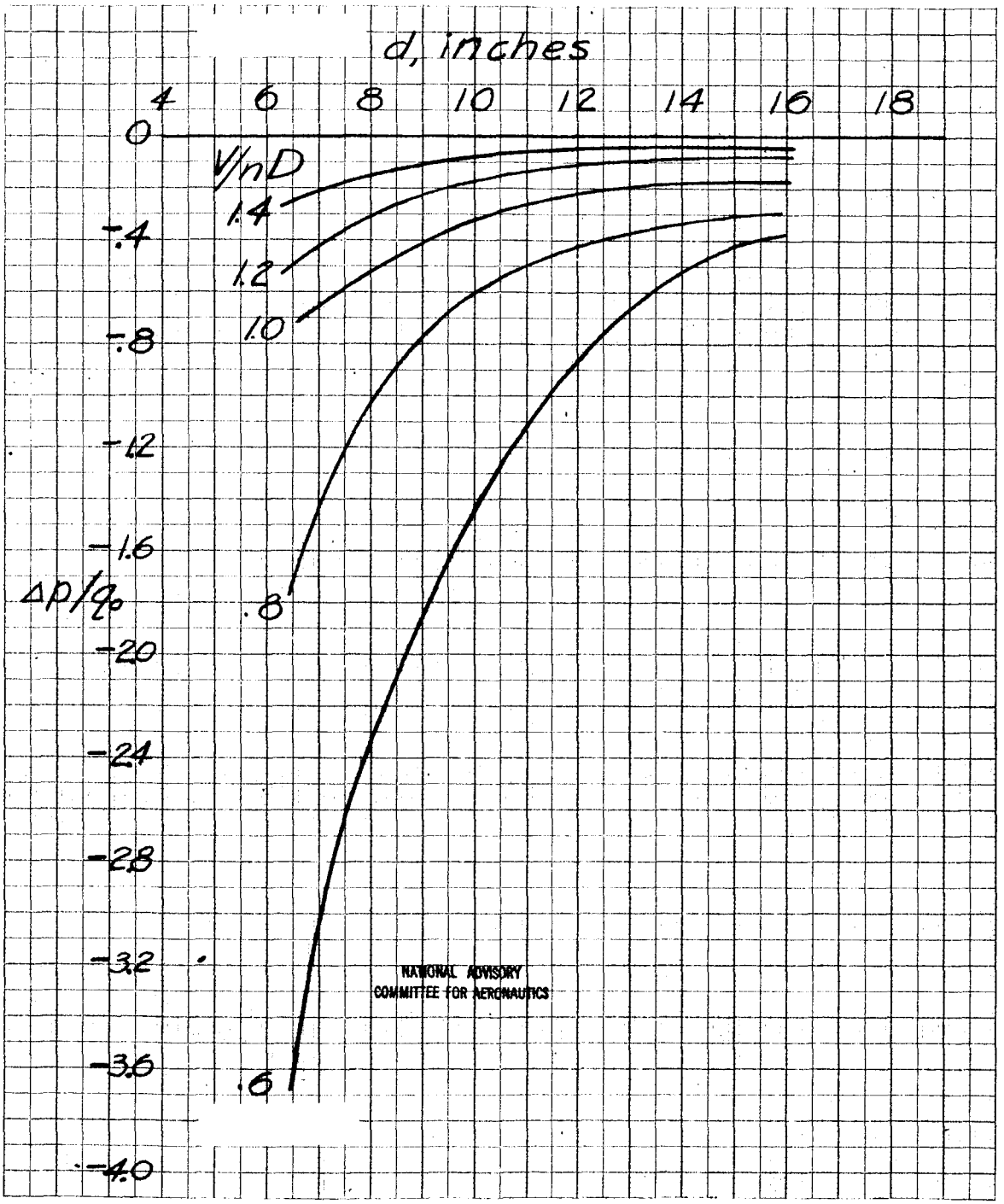

(b) $\beta = 30^{\circ}$.

Figure 19.- Continued.

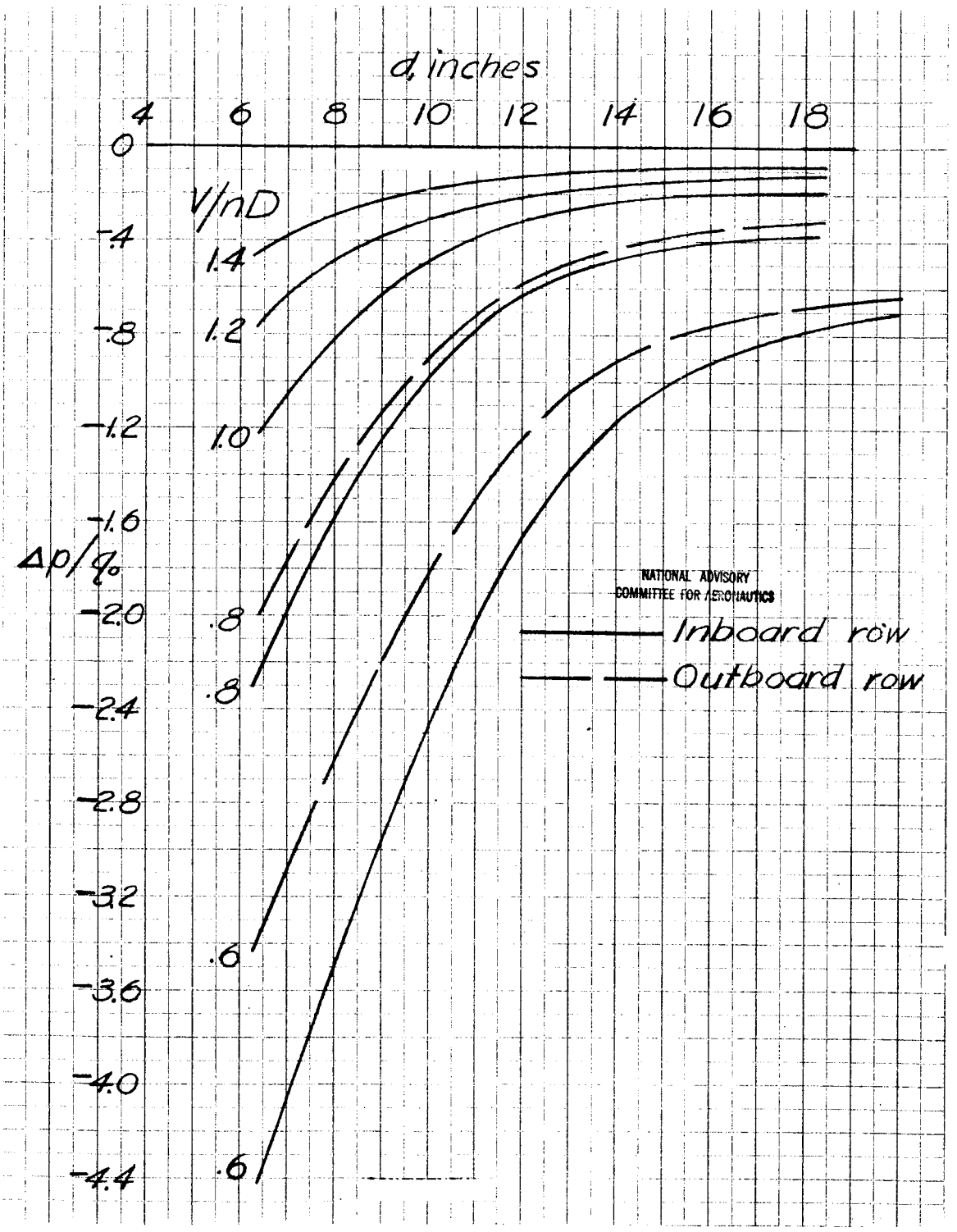

(c) $\beta = 40^{\circ}$.

Figure 19. Concluded.

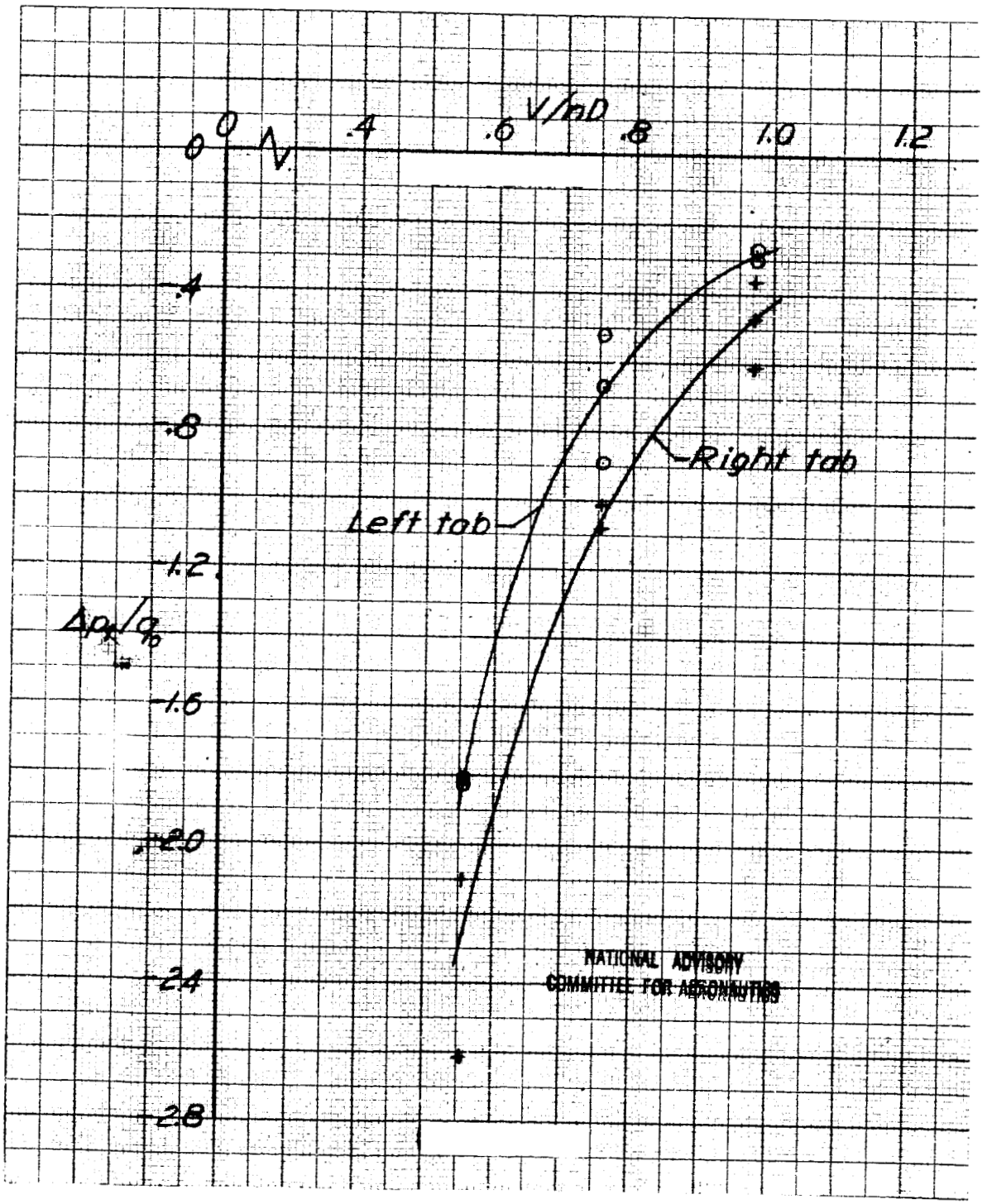

Figure 20.- Peak pressure coefficients on the tabs as a function of V/nD. Tail surfaces in position I; $\beta = 30^{\circ}$; $\alpha = 0^{\circ}$; $\delta_e = 0^{\circ}$; $\delta_r = 0^{\circ}$.

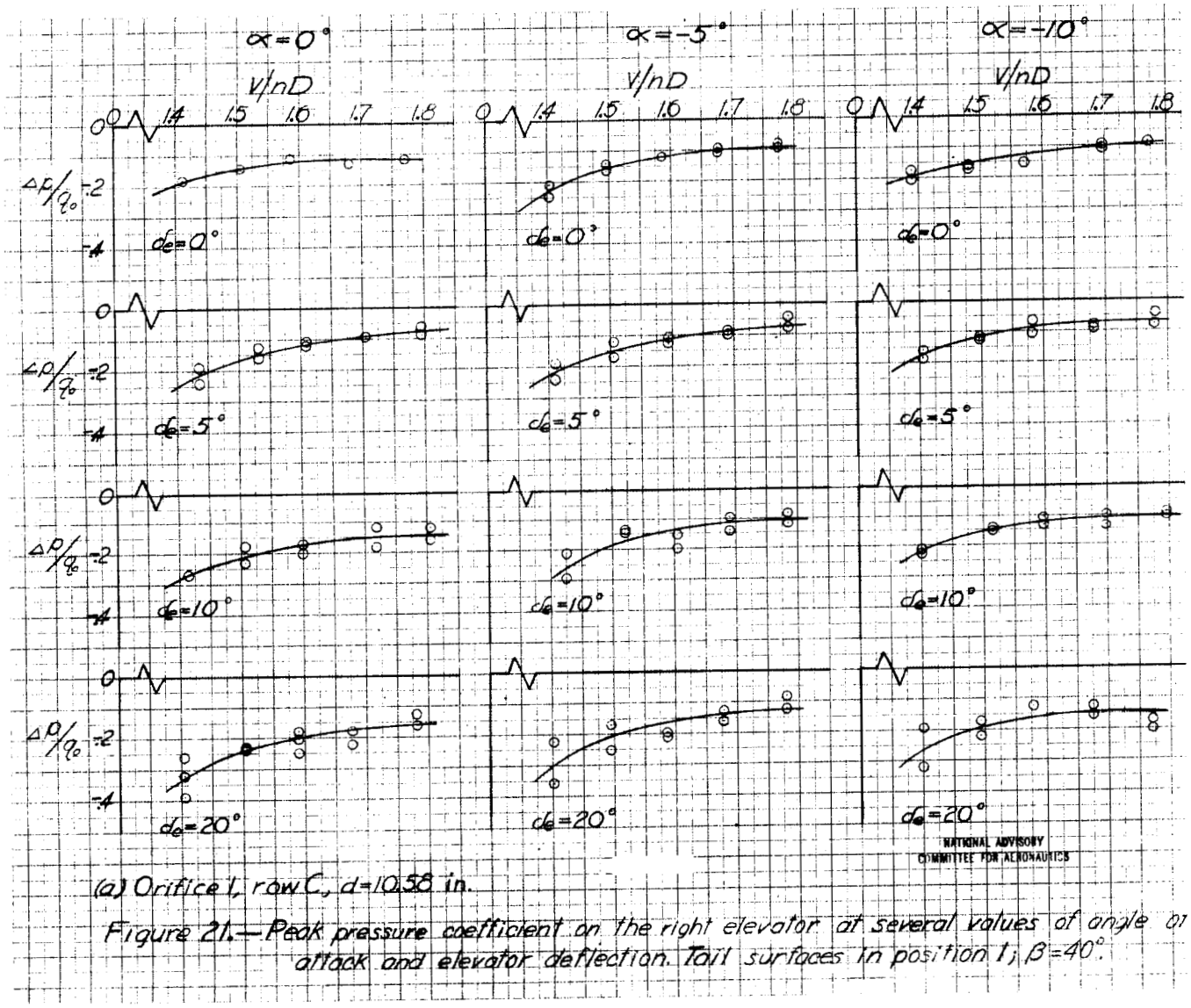

(a) Orifice 1, row C, d=10.58 in.

Figure 21.—Peak pressure coefficient on the right elevator at several values of angle of attack and elevator deflection. Tail surfaces in position 1; β=40°.

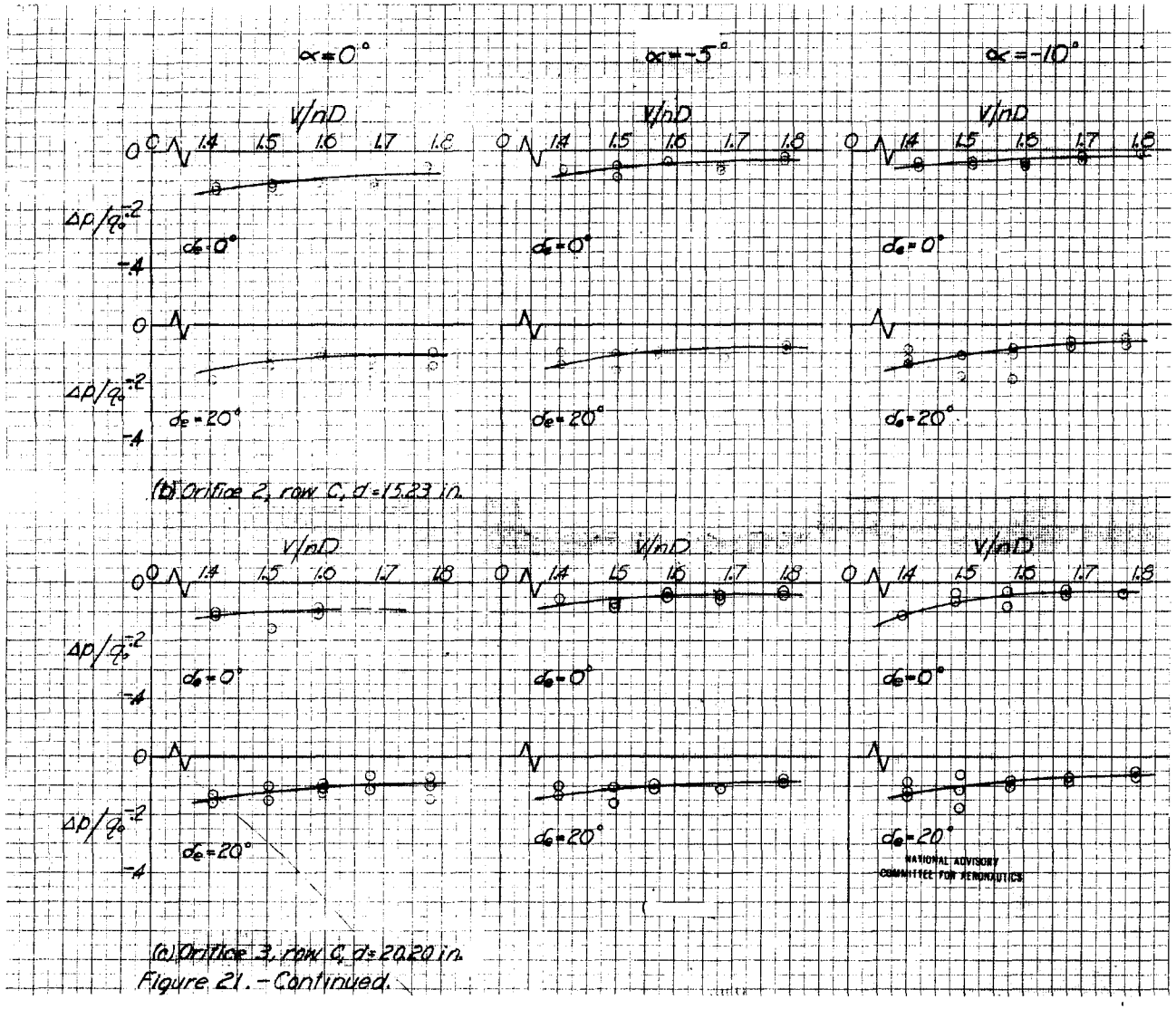

(b) Orifice 2, row C, d = 15.23 in.

(c) Orifice 3, row C, d = 20.20 in.

Figure 21. - Continued.

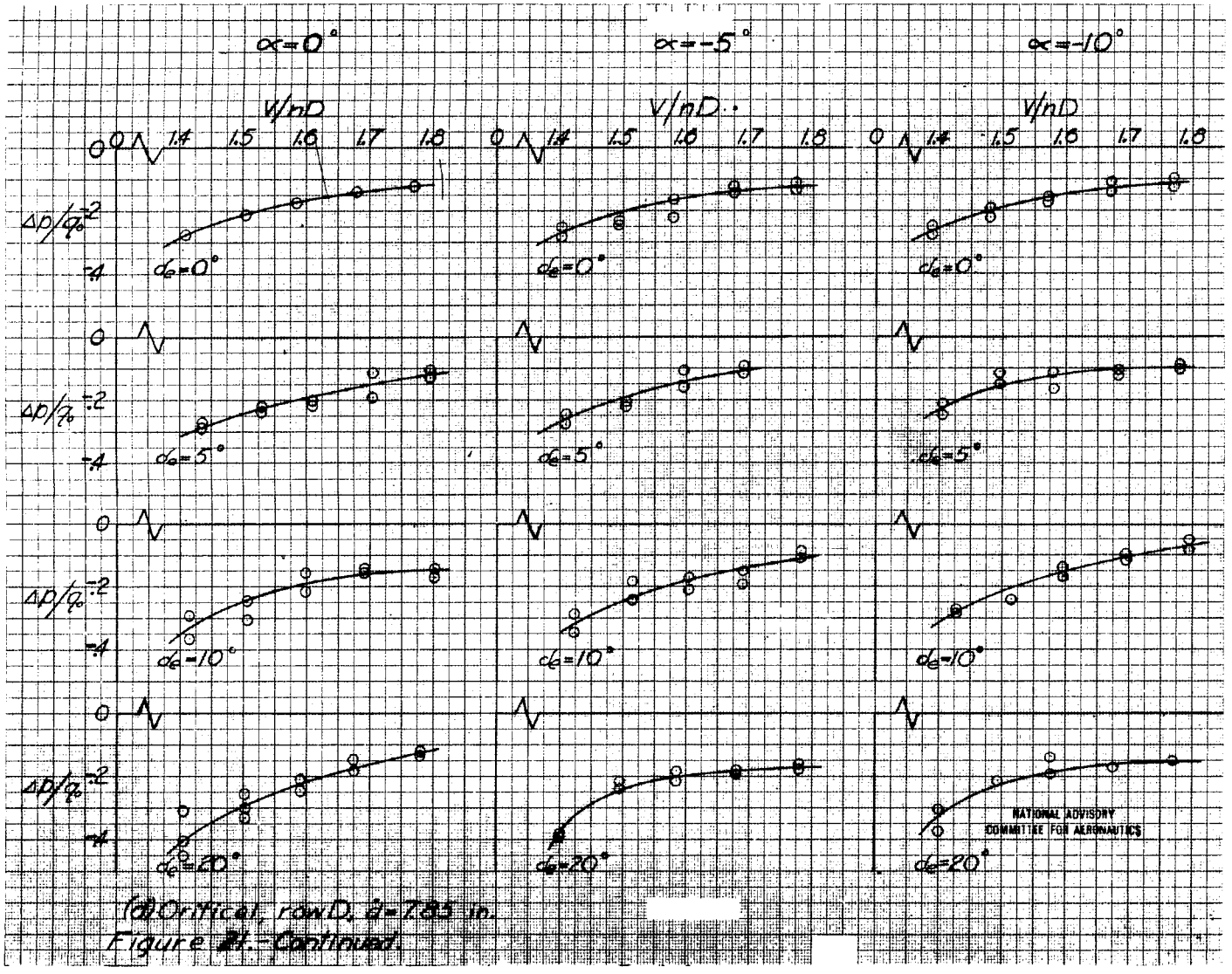

(d) Orifical, rowD, d = .785 in.

Figure 11.- Continued.

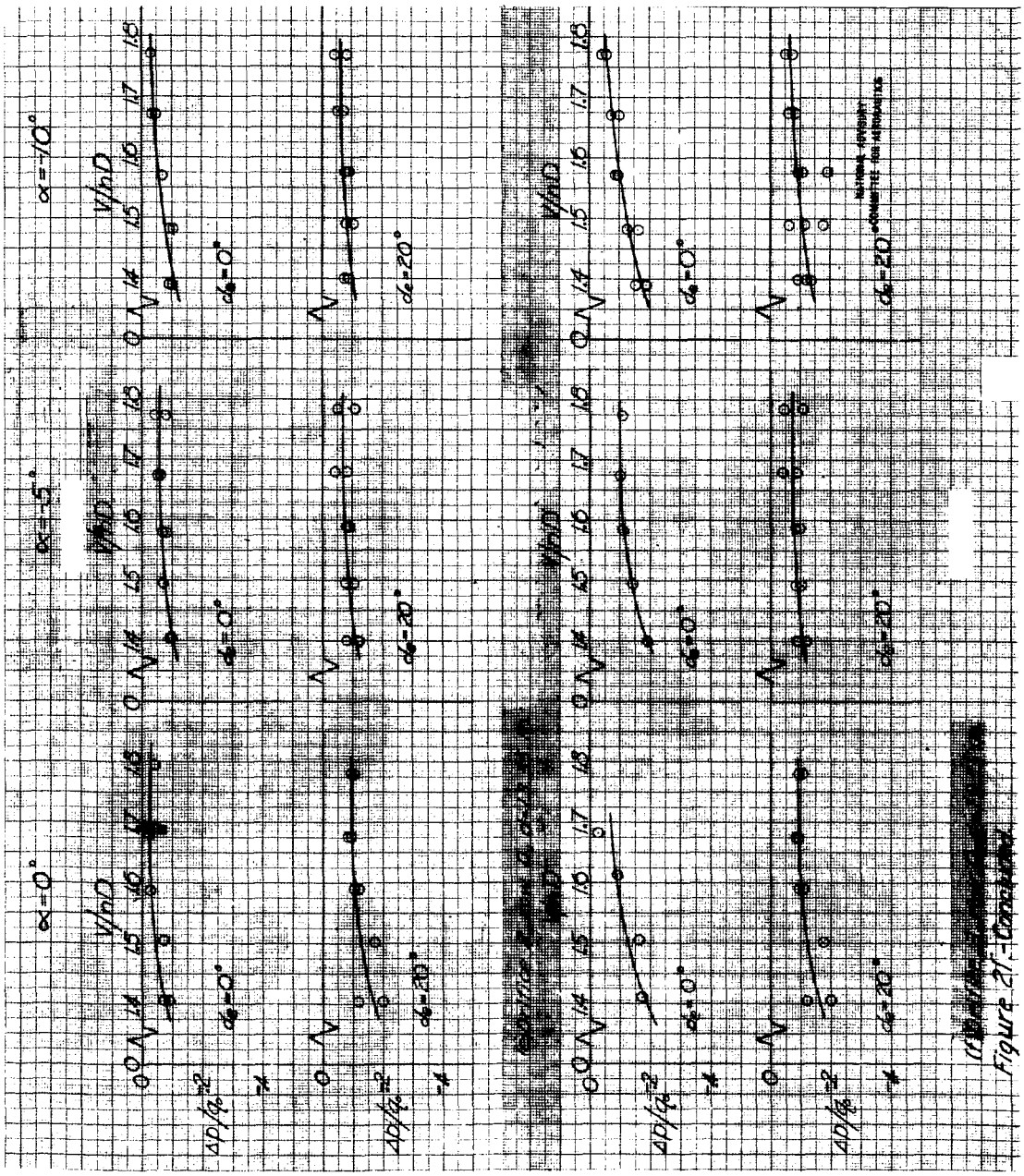

Figure 21.- Concluded.

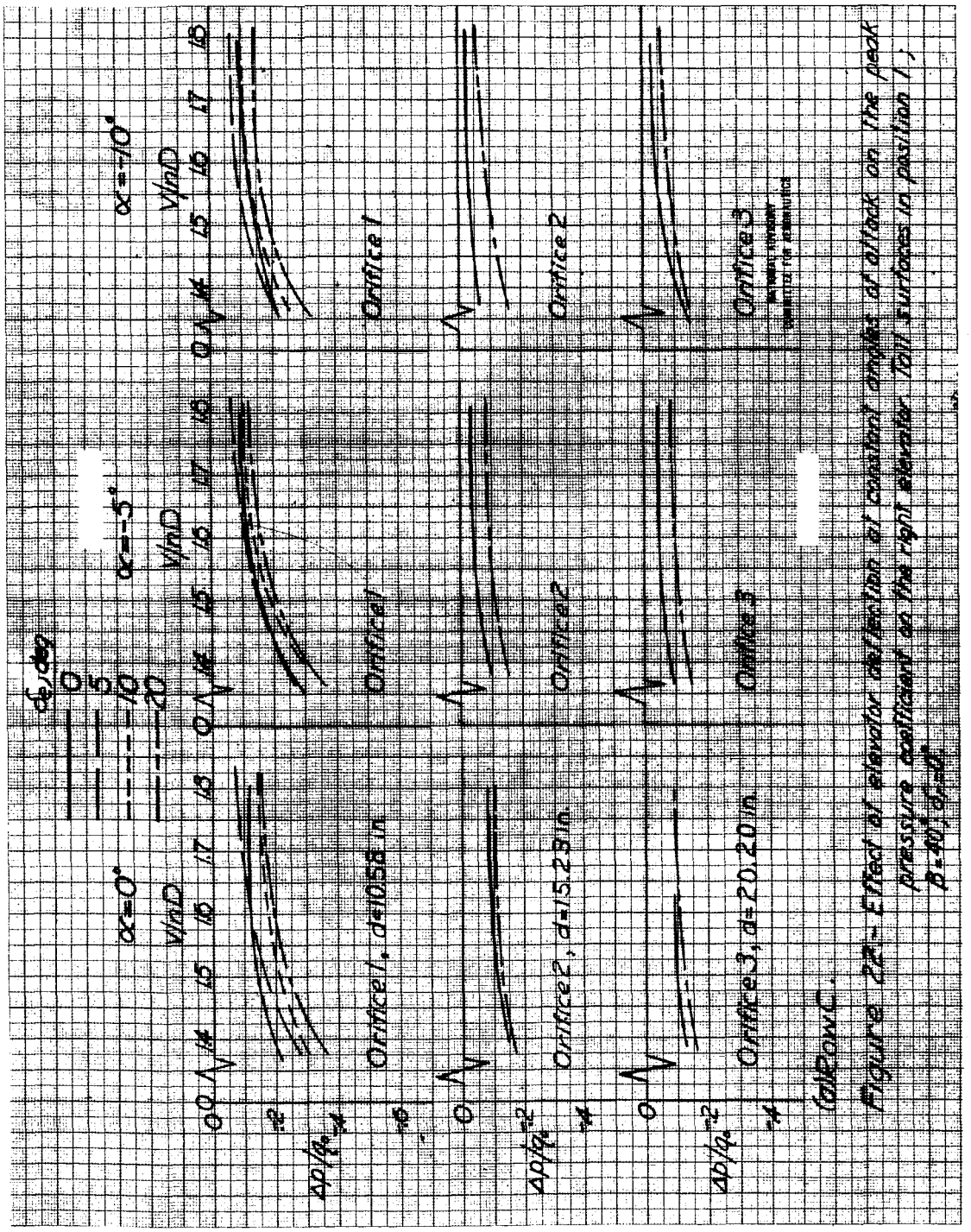

Figure 22.- Effect of elevator deflection at constant angles of attack on the peak pressure coefficient on the right elevator roll surfaces in position 1; $\beta = 40°$, $\delta_r = 0°$.

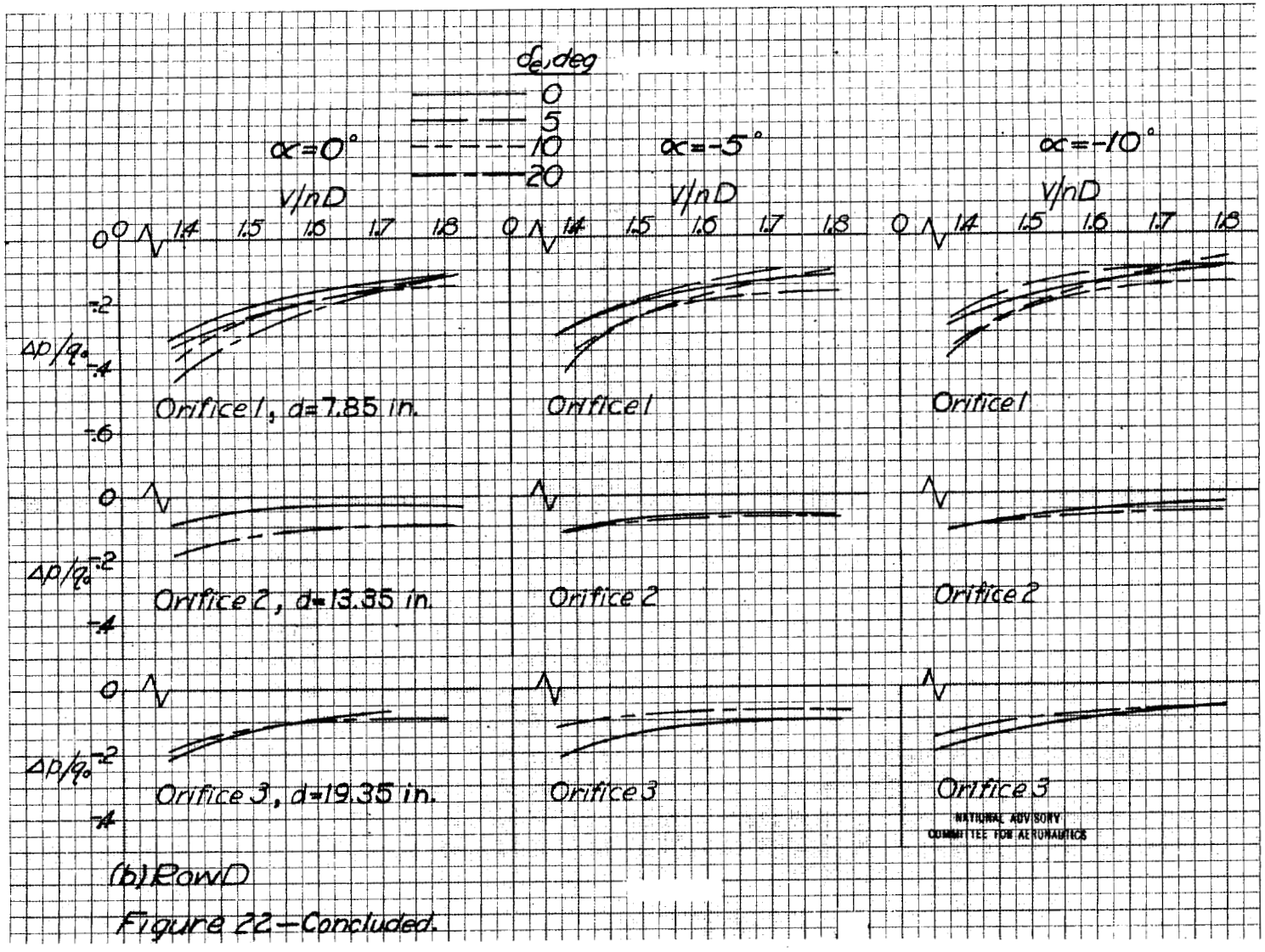

(b) R on D

Figure 22—Concluded.

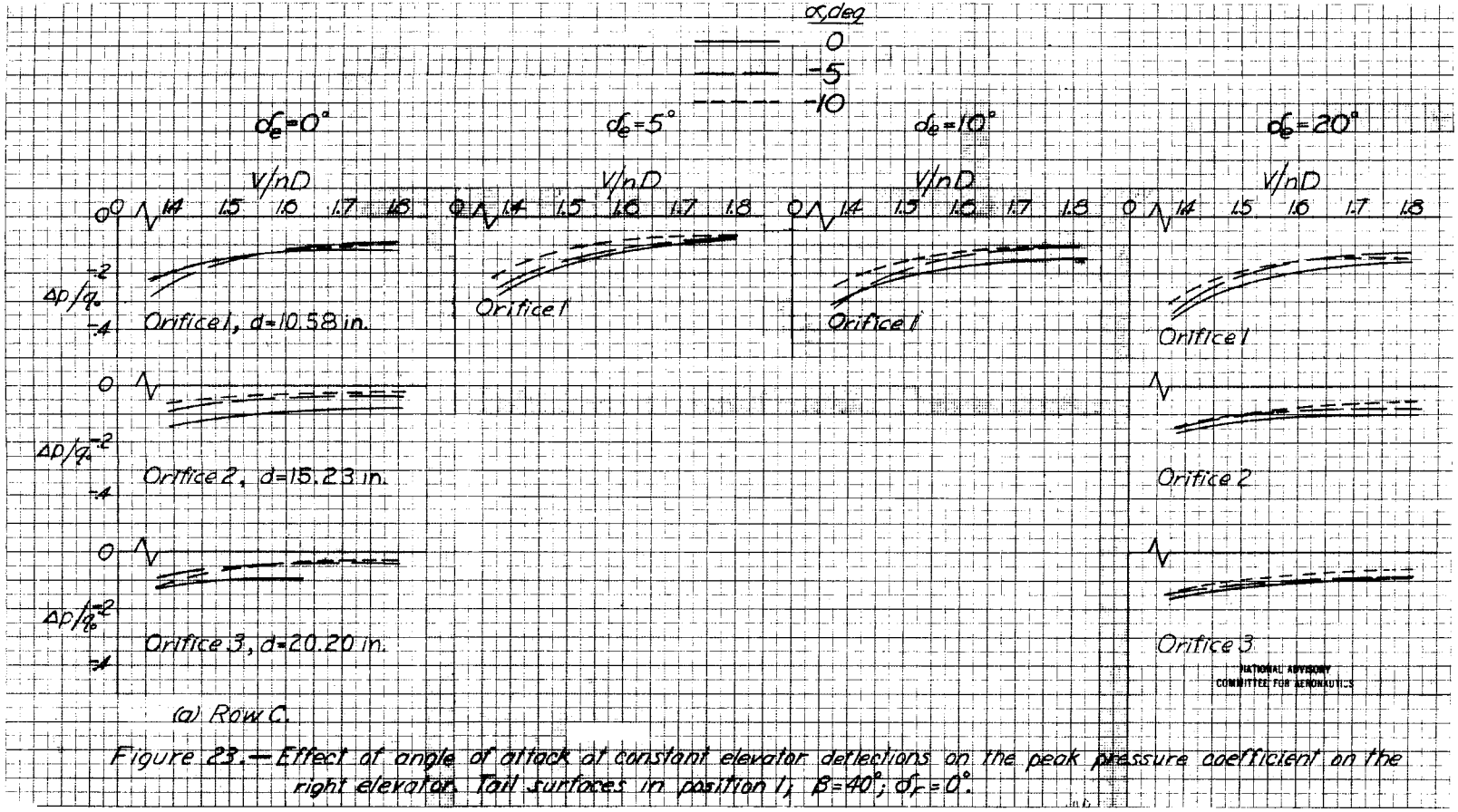

(a) Row C.

Figure 23.— Effect of angle of attack at constant elevator deflections on the peak pressure coefficient on the right elevator tail surfaces in position 1; $\beta=40°$; $\delta_r=0°$.

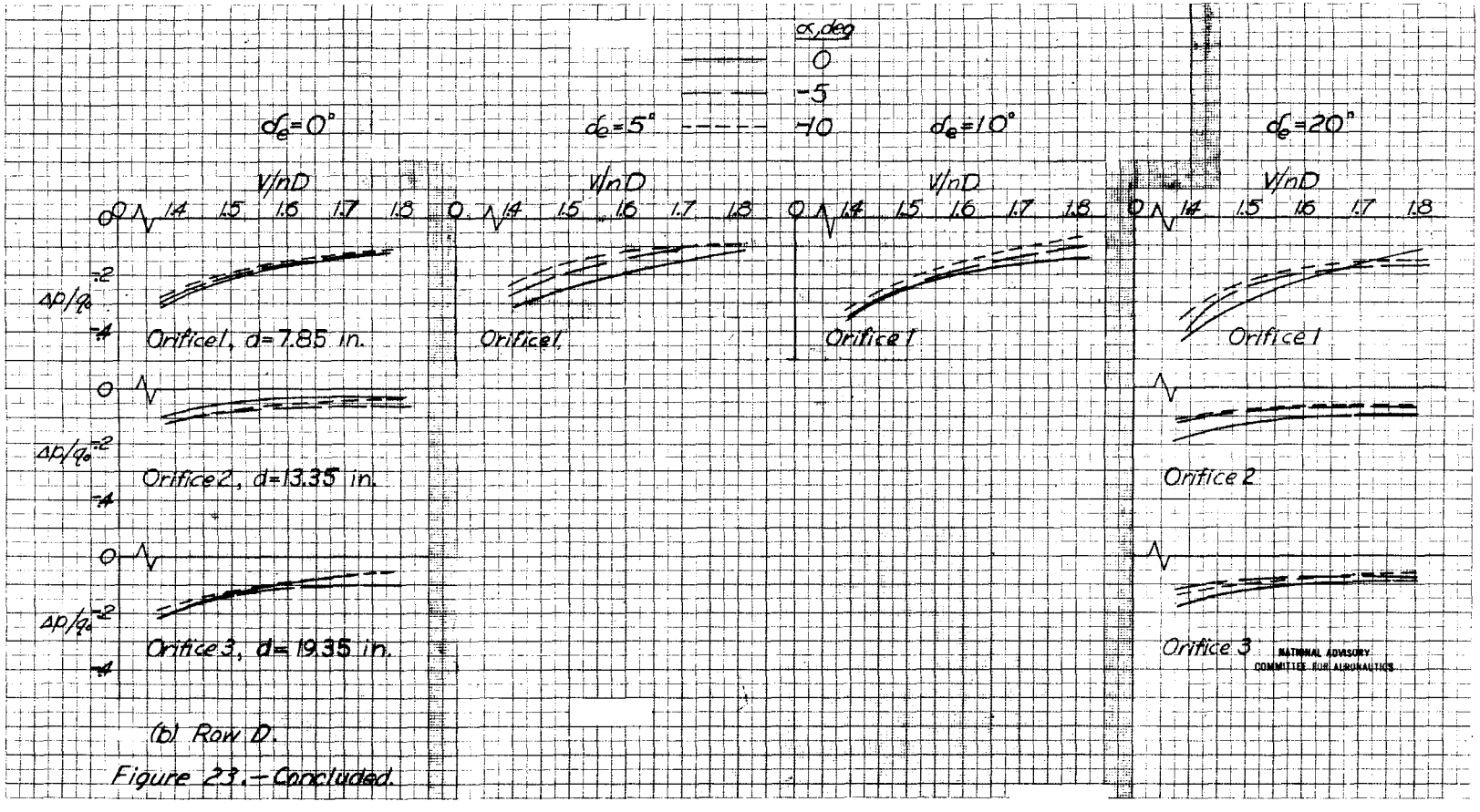

(b) Row D.

Figure 23.- Concluded.

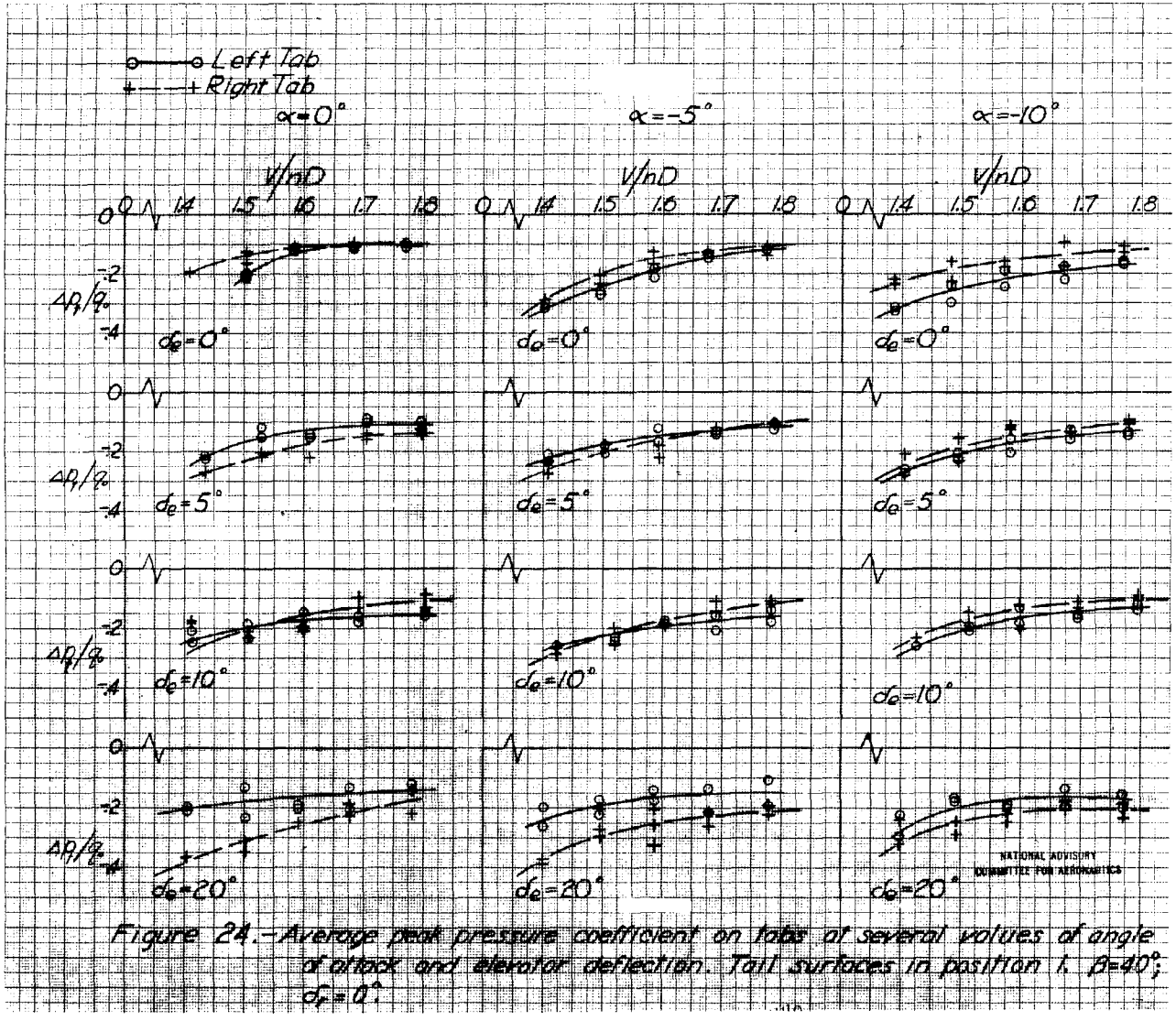

Figure 24.- Average peak pressure coefficient on tabs at several values of angle of attack and elevator deflection. Tail surfaces in position 1. $\beta=40°$; $\delta_r=0°$.

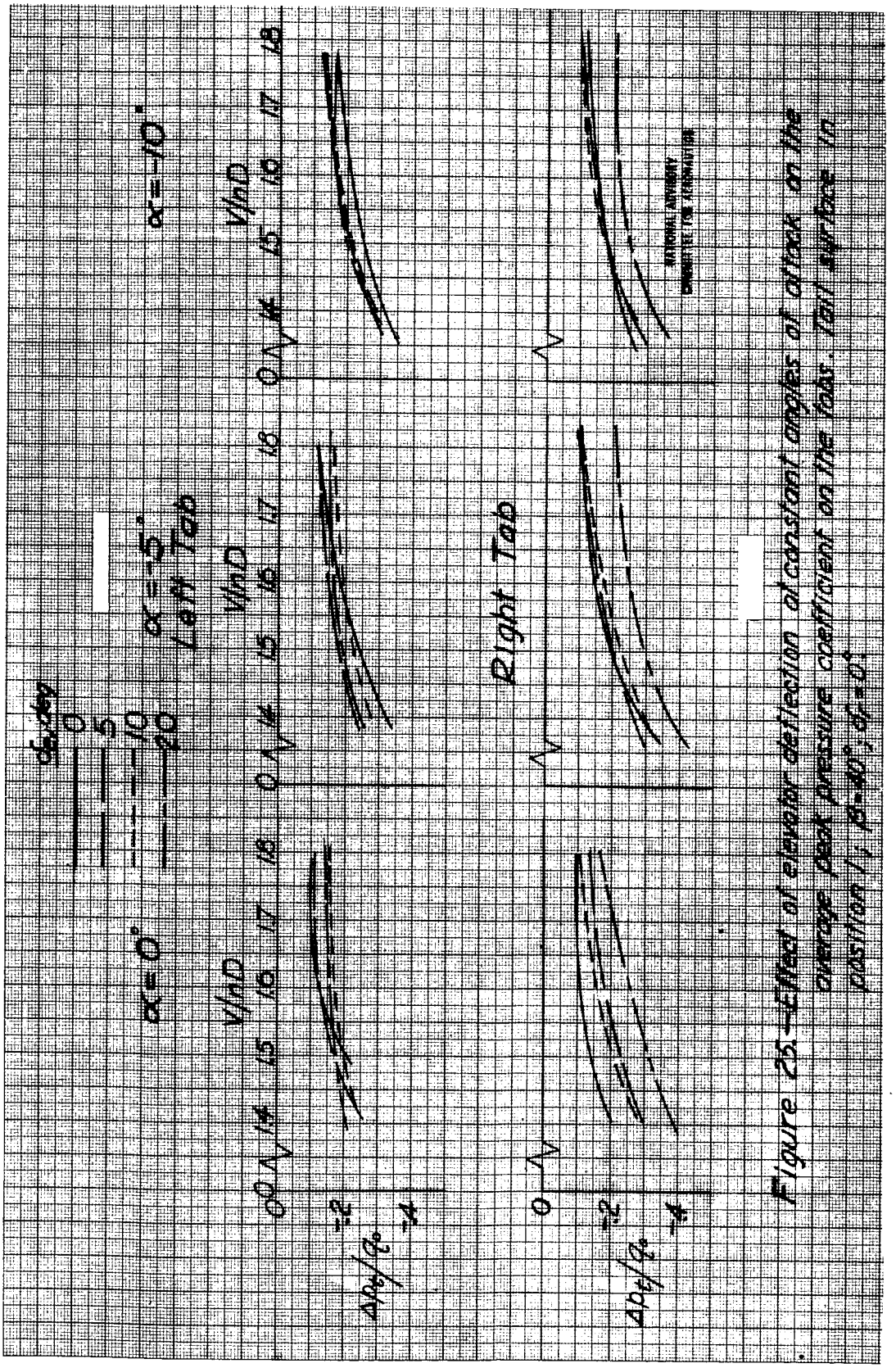

Figure 25.- Effect of elevator deflection at constant angles of attack on the average peak pressure coefficient on the tabs. Tail surface in position I; i_t, -10°; δ_f, 0°.

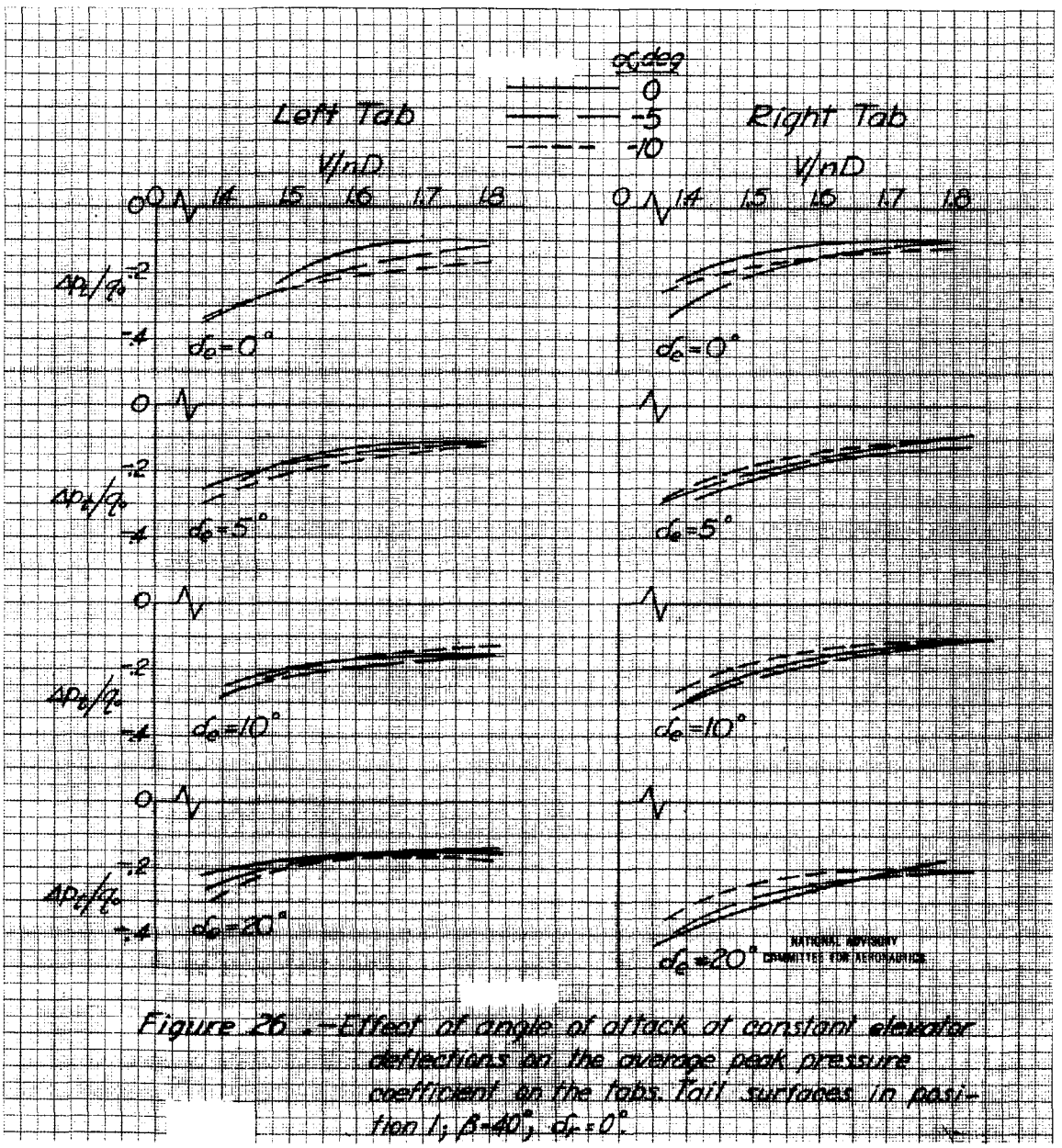

Figure 26.--Effect of angle of attack at constant elevator deflections on the average peak pressure coefficient on the tabs. Tail surfaces in position 1; $\beta=40°$, $\delta_r=0°$.

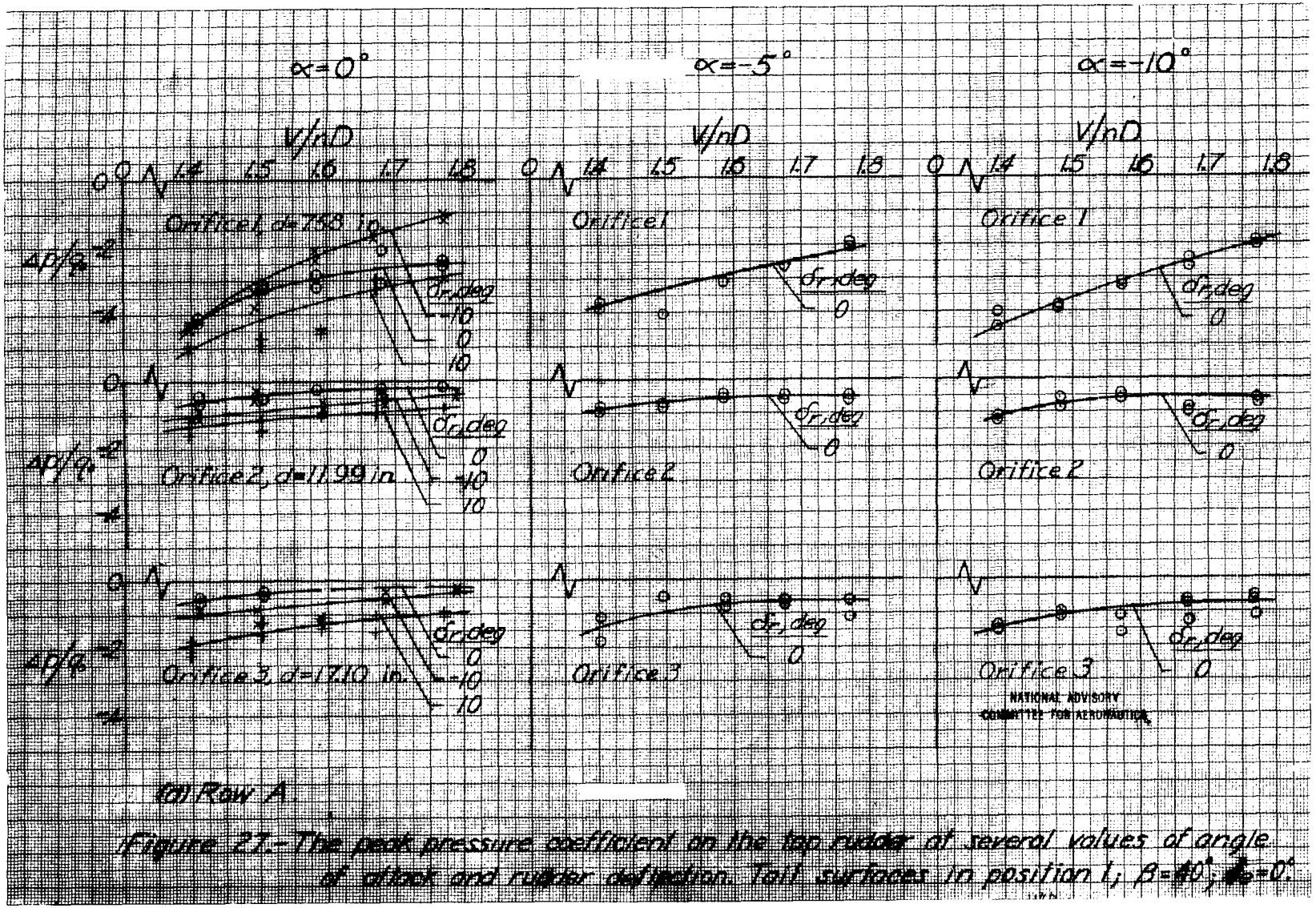

(d) Row A.

Figure 27.- The peak pressure coefficient on the top rudder at several values of angle of attack and rudder deflection. Tail surfaces in position 1; $\beta = 0°$; $\delta_e = 0°$.

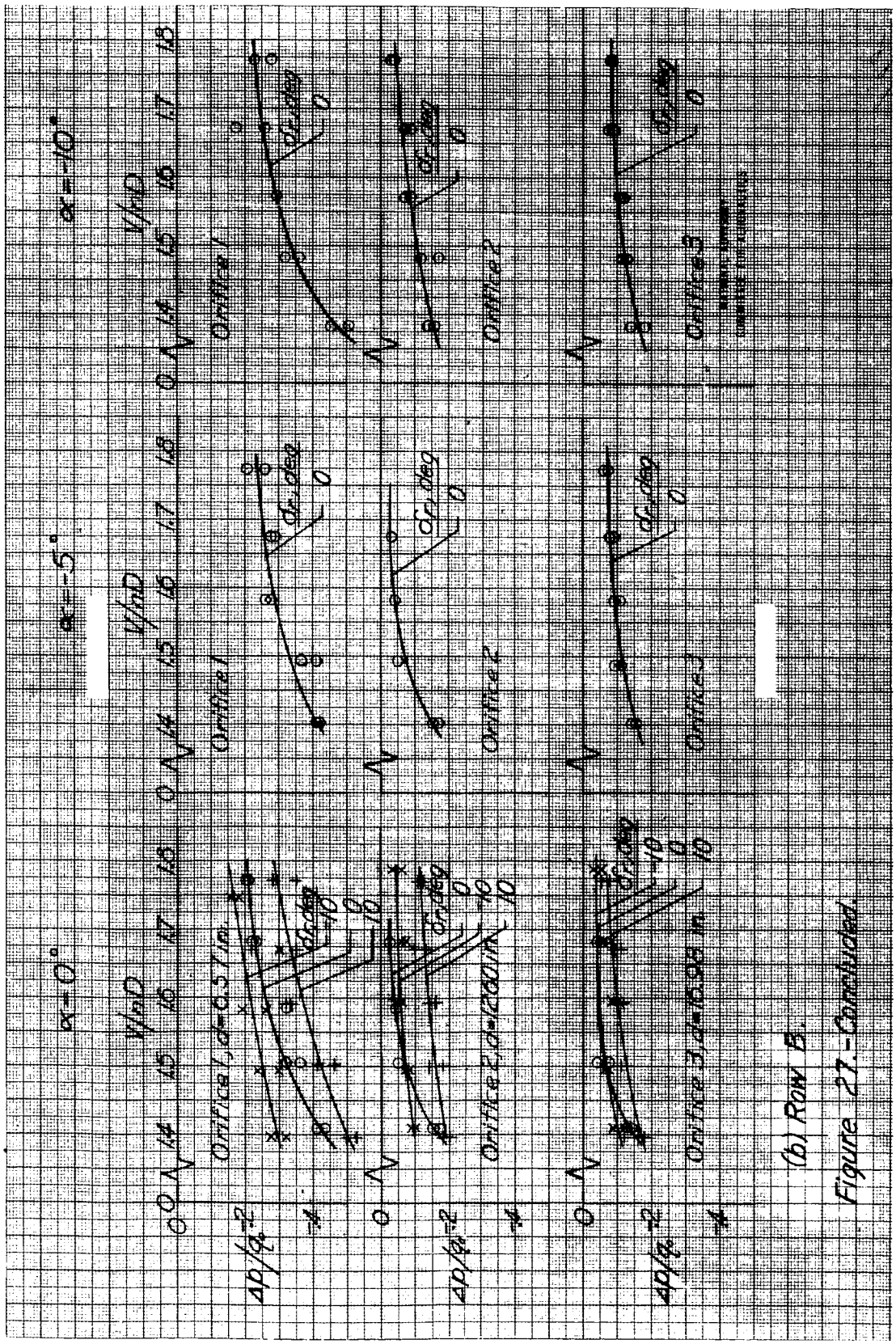

(b) Row B.

Figure 27.- Concluded.

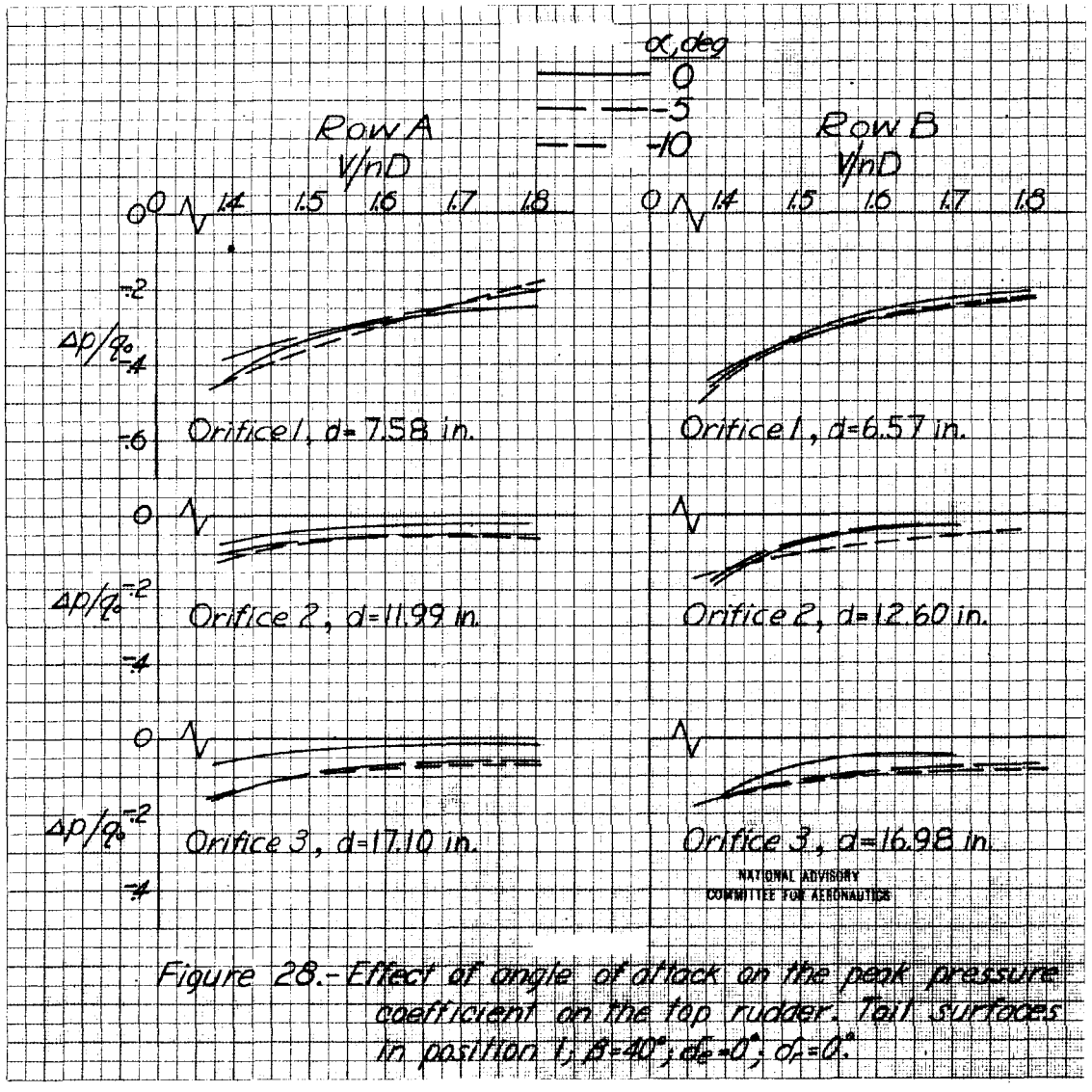

Figure 28.- Effect of angle of attack on the peak pressure coefficient on the top rudder. Tail surfaces in position 1; $\beta=40°$; $d_{f_e}=0°$; $d_{f_r}=0°$.

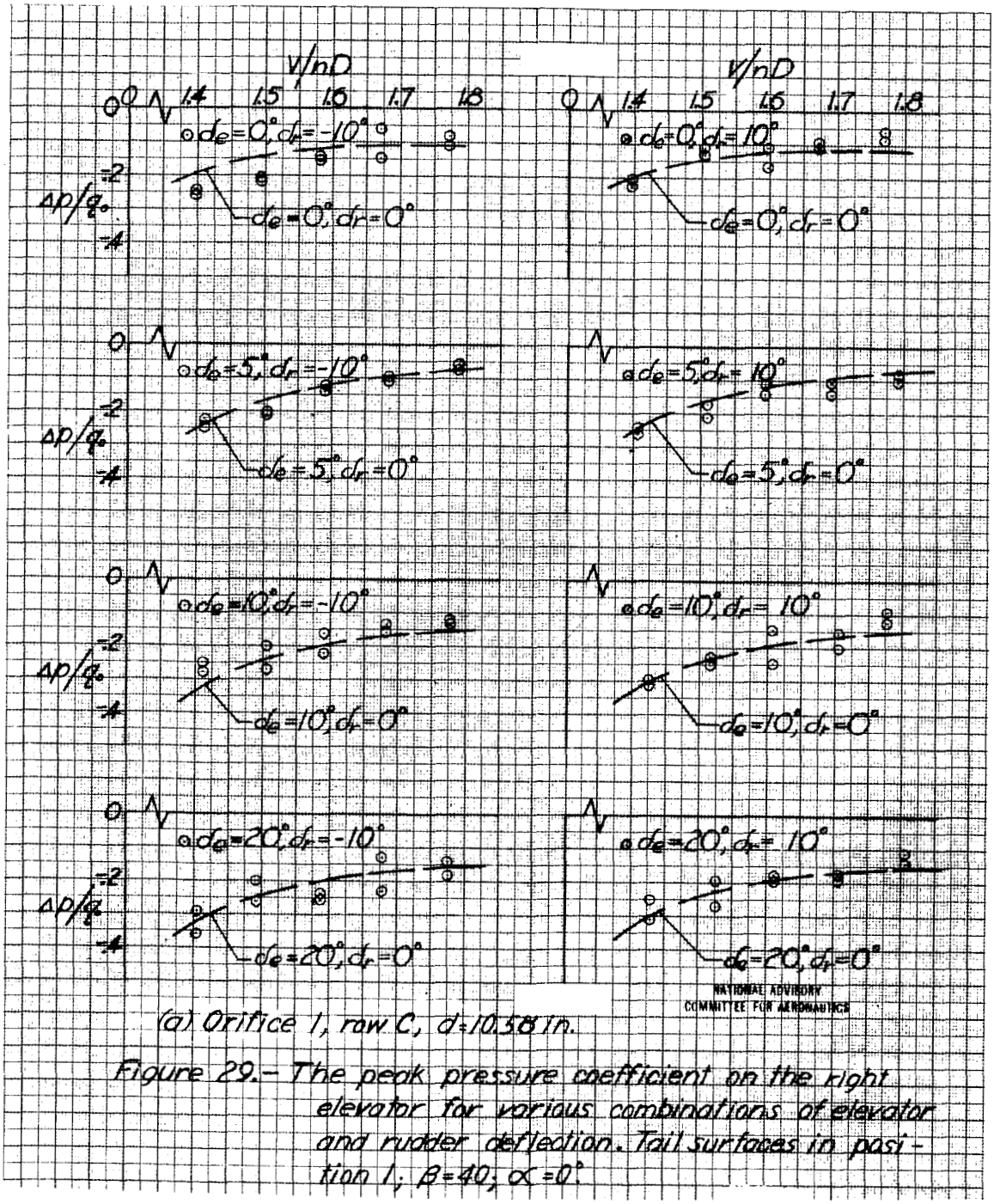

(a) Orifice 1, row C, d=10.38 in.

Figure 29.- The peak pressure coefficient on the right elevator for various combinations of elevator and rudder deflection. Tail surfaces in position 1; $\beta = 4.0$; $\alpha = 0°$.

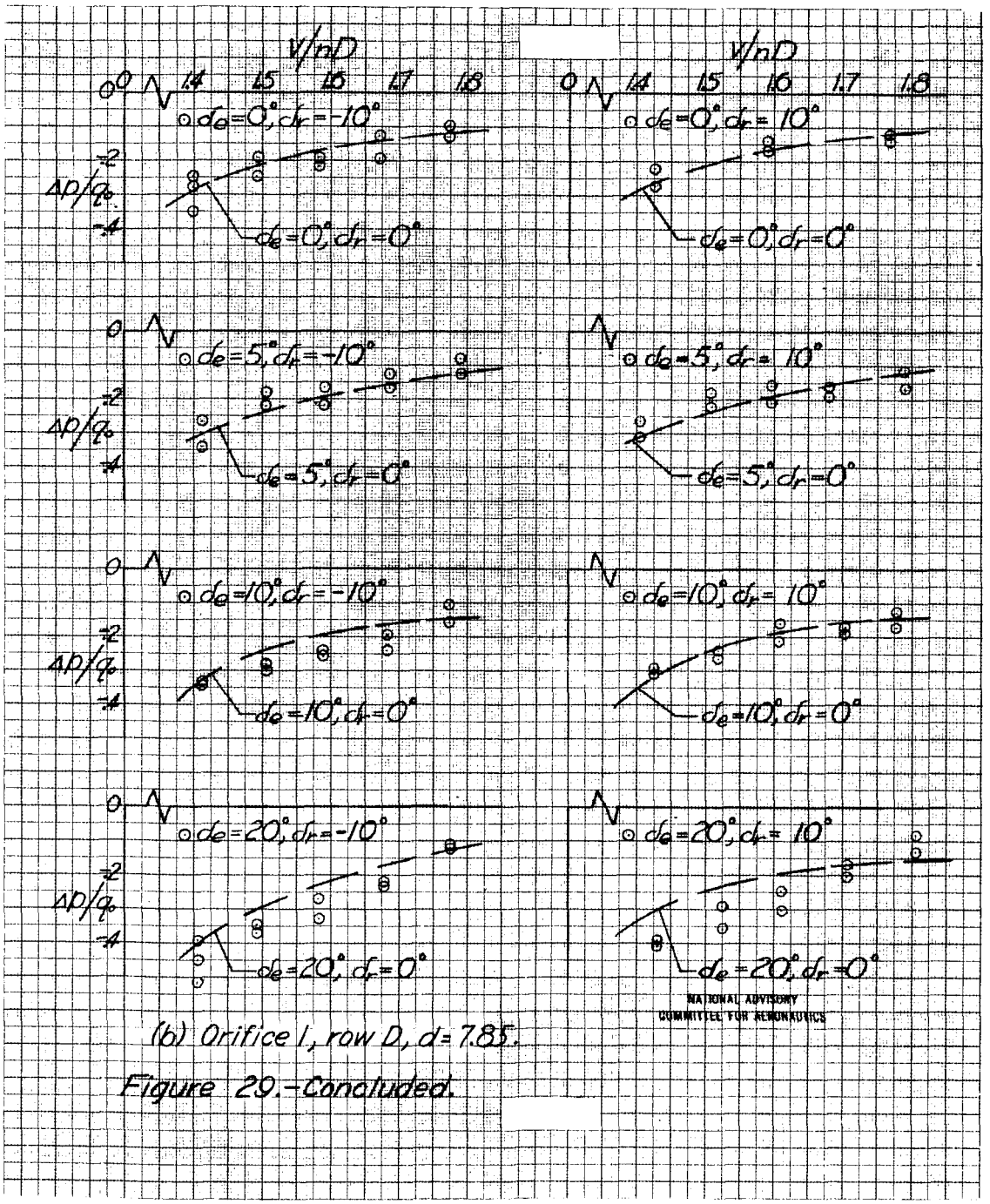

(b) Orifice 1, row D, d = 7.85.

Figure 29.- Concluded.

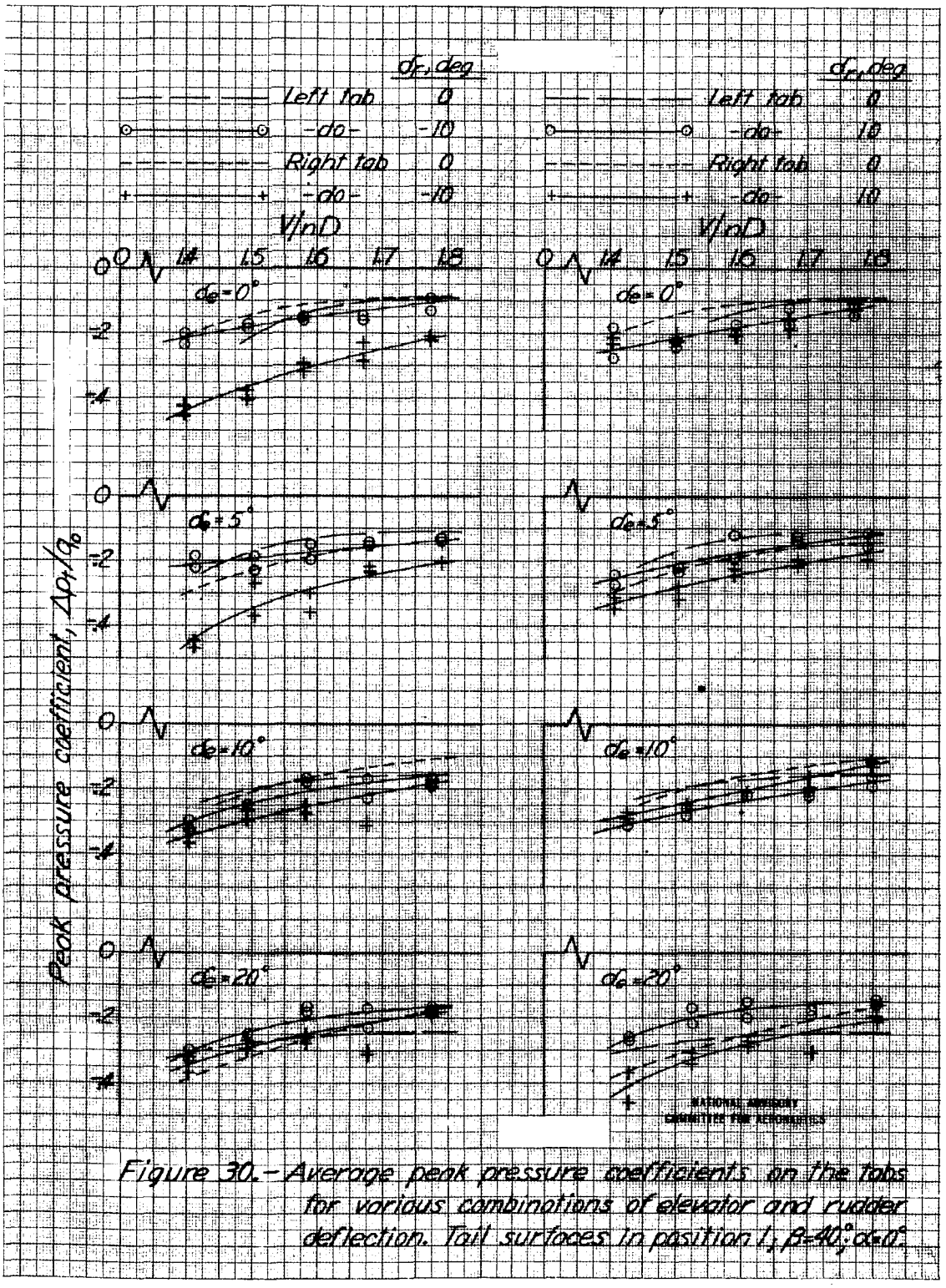

Figure 30.- Average peak pressure coefficients on the tabs for various combinations of elevator and rudder deflection. Tail surfaces in position 1; $\beta = 40°$; $\alpha = 0°$.

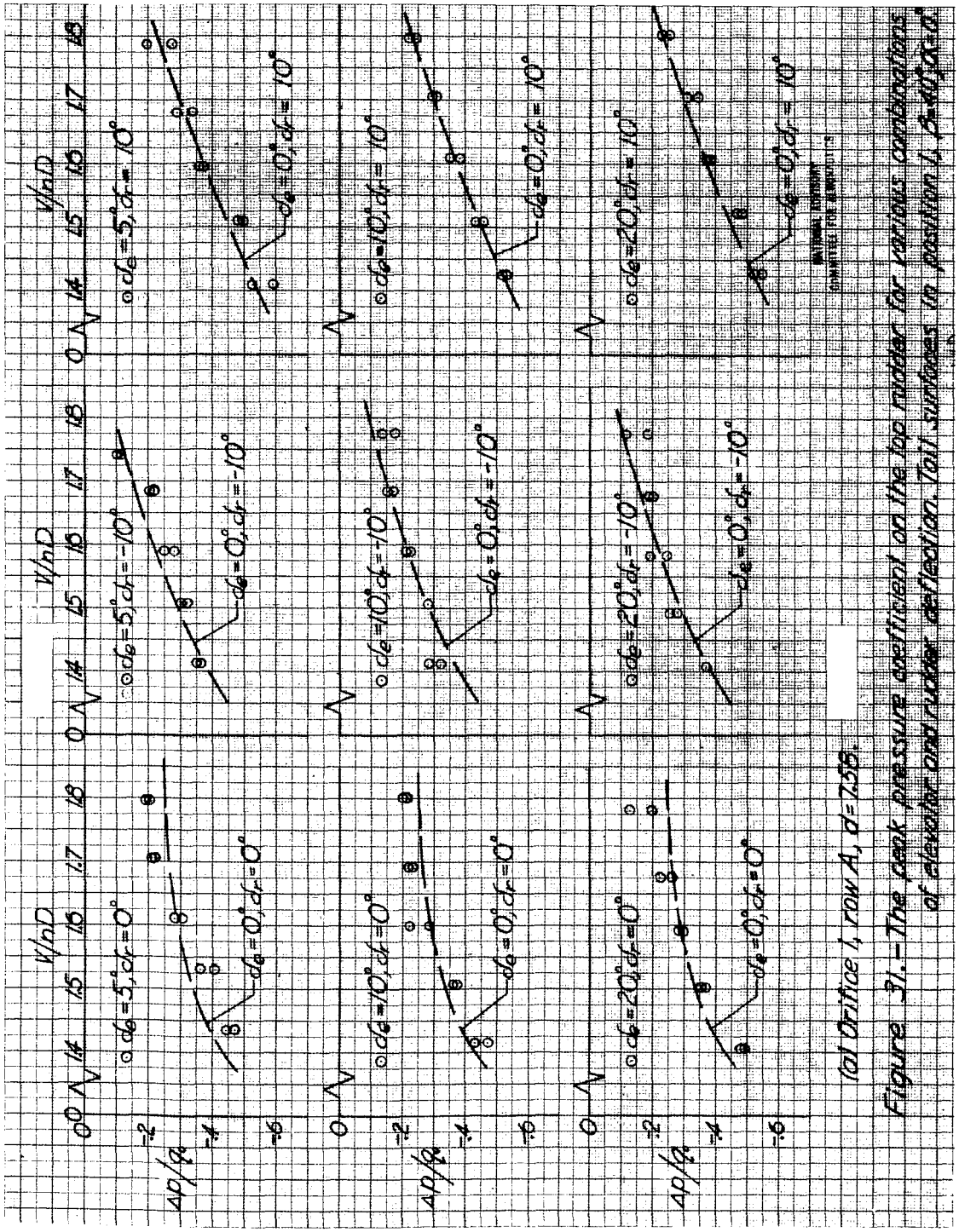

Figure 31.- The peak pressure coefficient on the top rudder for various combinations of elevator and rudder deflection. Tail surfaces in position 1, β=40°, α=0°, tail orifice 1, row A, σ=.758.

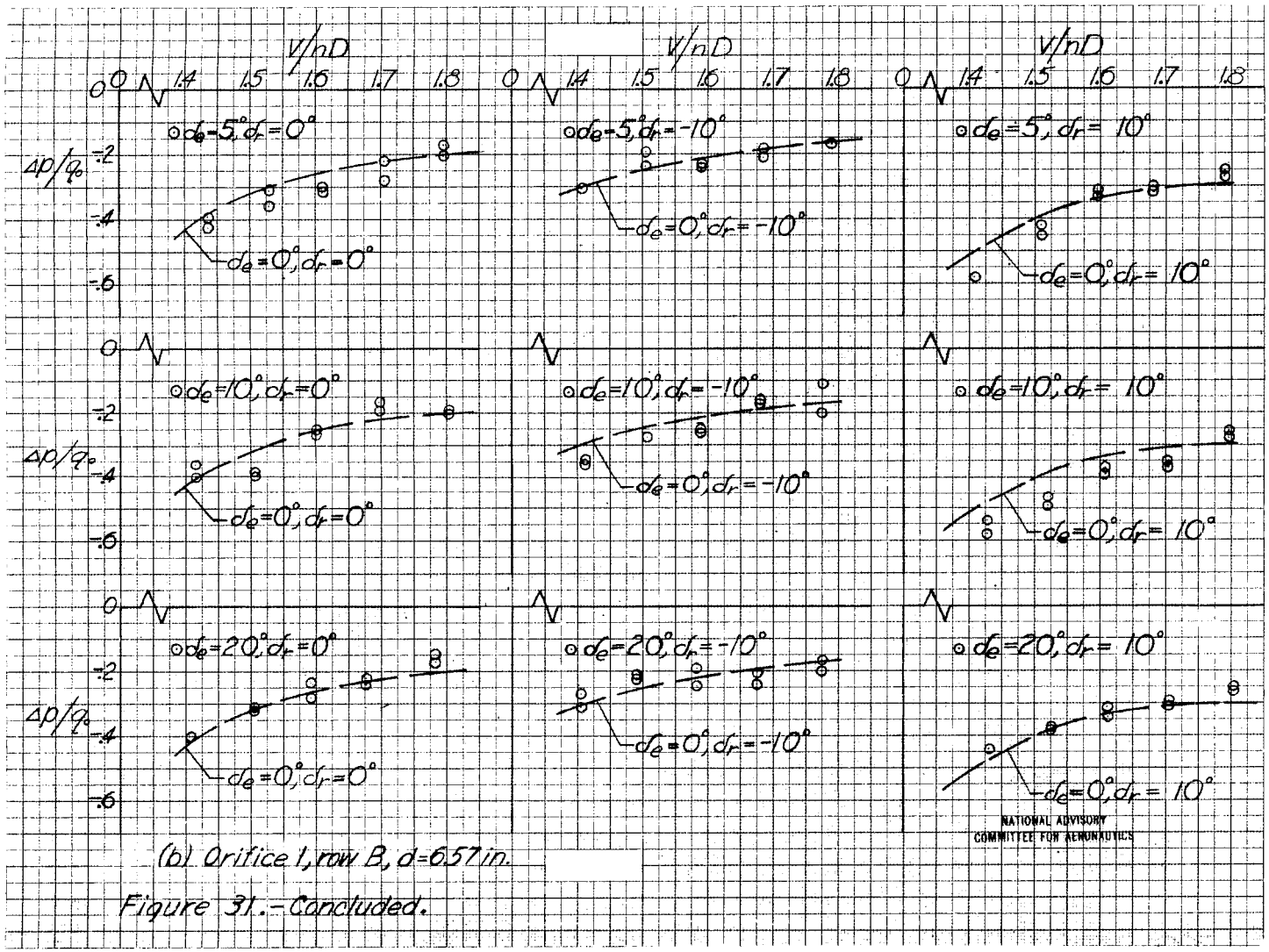

(b) Orifice 1, row B, d=6.57 in.

Figure 31.- Concluded.

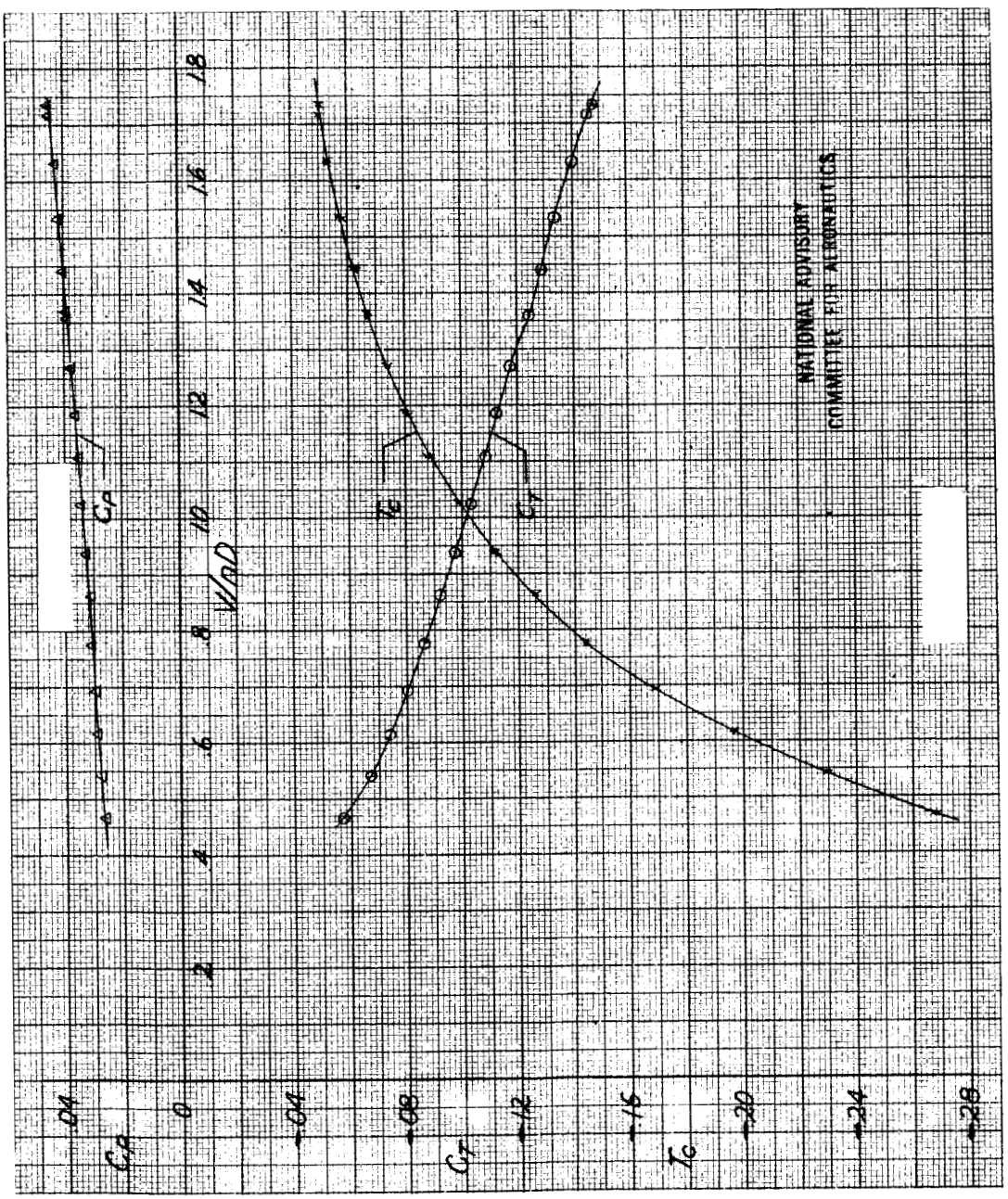

Figure 32.- Negative thrust characteristics of the one-bladed propeller. Tail surfaces in position 1; $\beta = -15°$; $\alpha = 0.4°$; $\delta_e = 0°$; $\delta_r = 0°$.

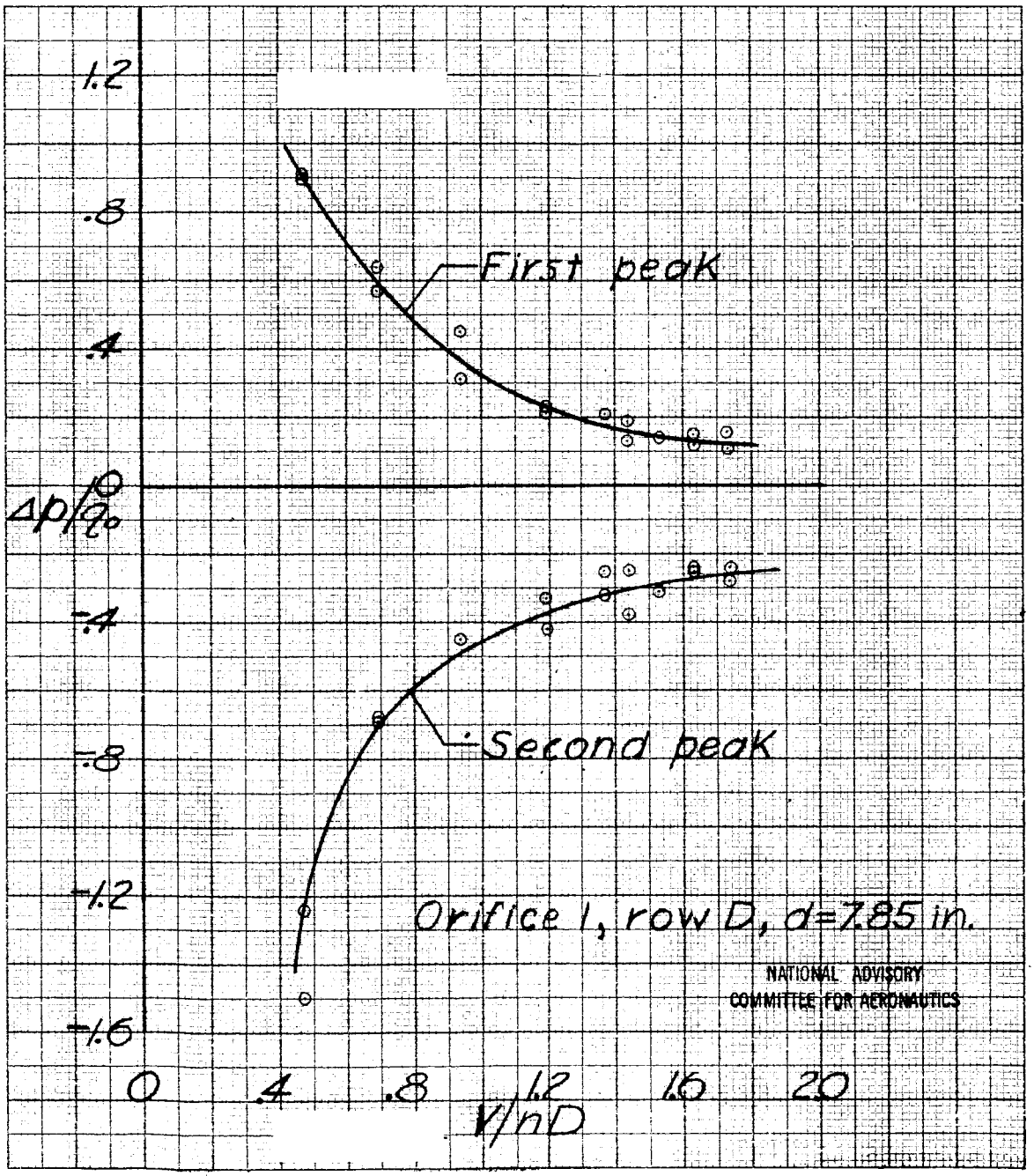

Figure 33.- Representative curves showing the first and second peak pressure coefficients in the negative-thrust condition. Tail surfaces in position 1; $\beta = -15^{\circ}$; $\alpha = 0.4^{\circ}$; $\delta_e = 0^{\circ}$; $\delta_r = 0^{\circ}$.

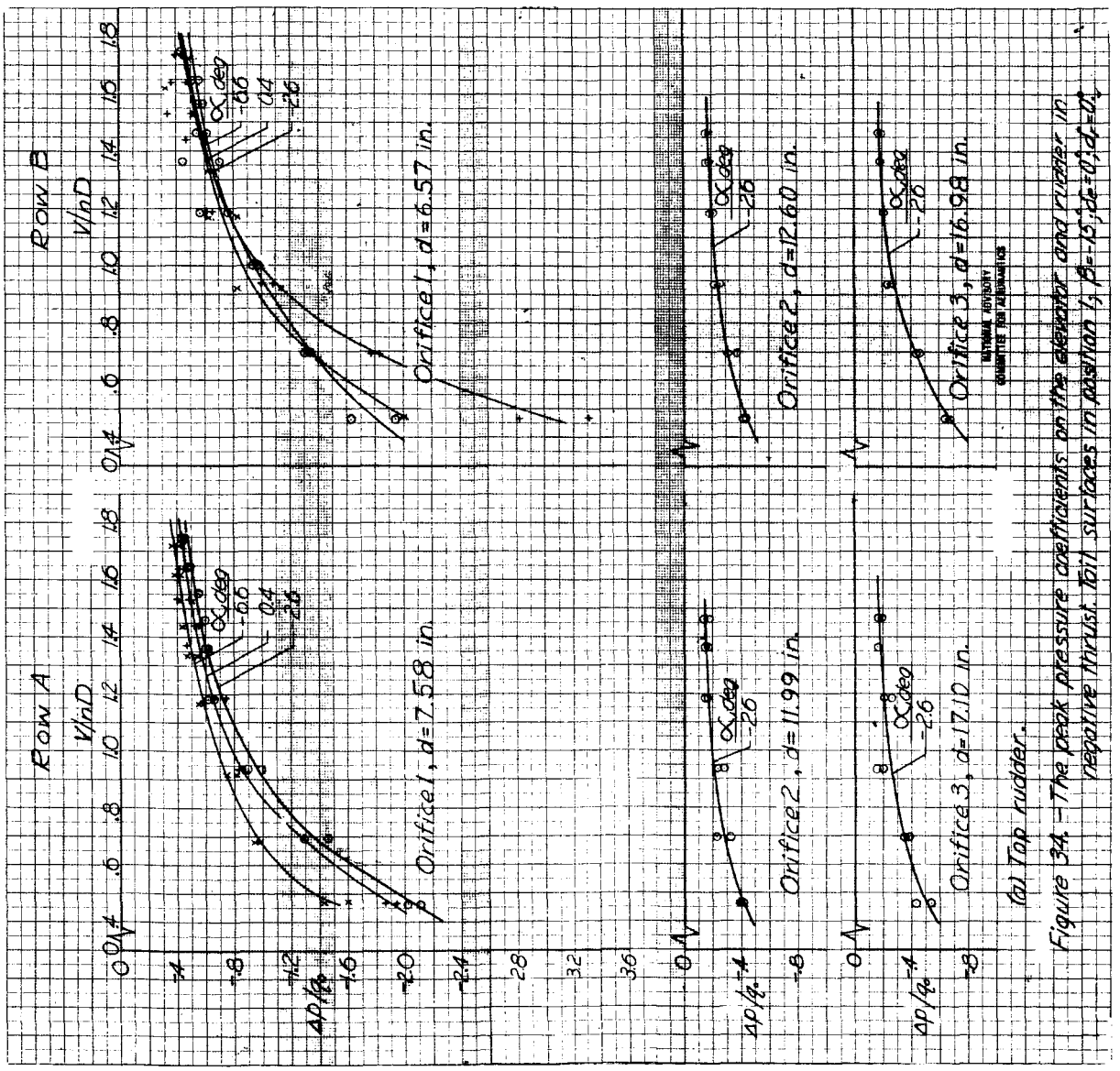

(a) Top rudder.

Figure 34.- The peak pressure coefficients on the elevator and rudder in negative thrust. Tail surfaces in position 1; β_e=-15°, δ_e=0°, δ_r=0°.

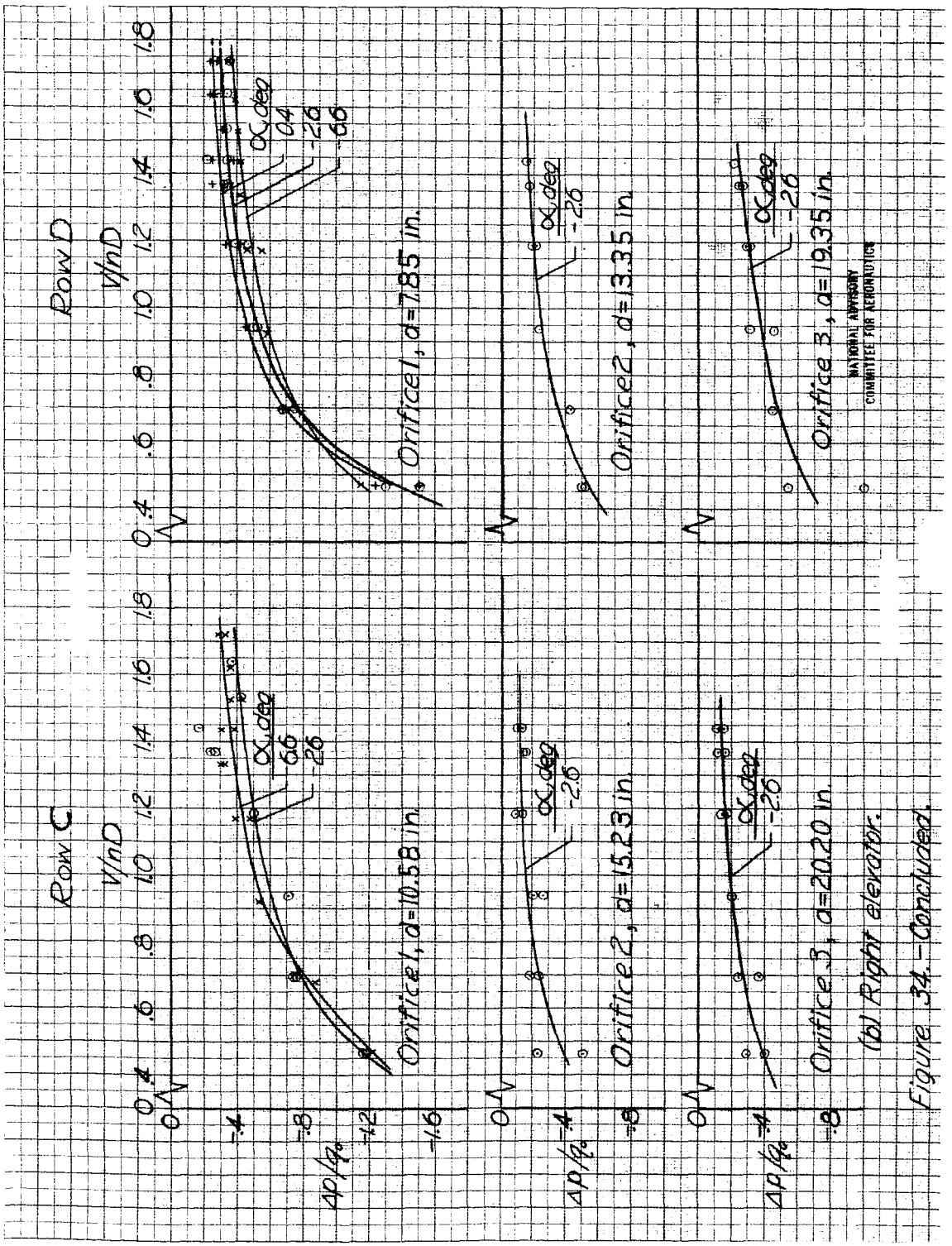

(b) Right elevator.

Figure 34.- Concluded.

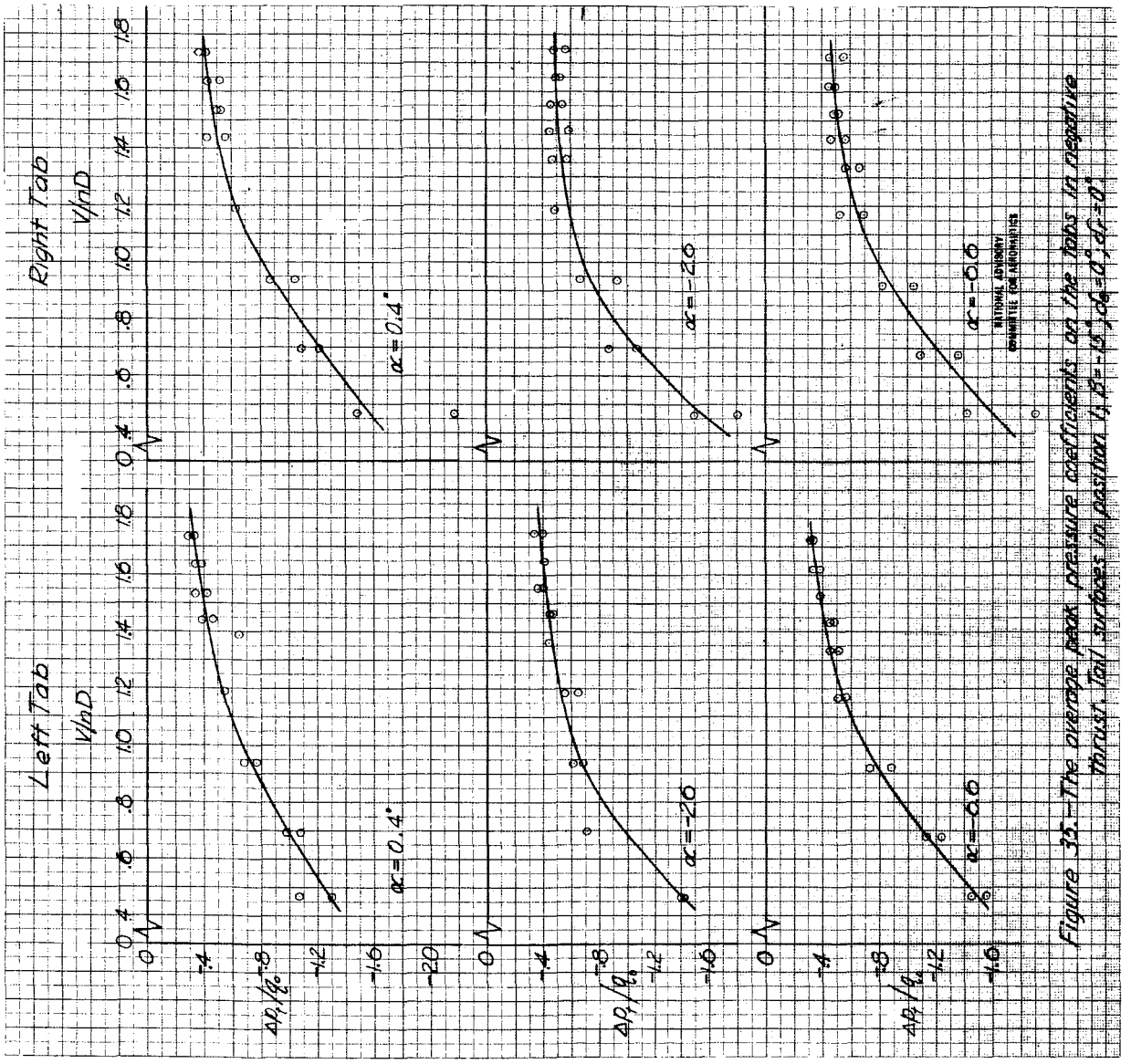

Figure 35.- The average peak pressure coefficients on the tabs in separate thrust, tail surfaces in position 1, $i_t = -1.5°$, $\delta_e = 0°$, $\delta_r = 0°$.

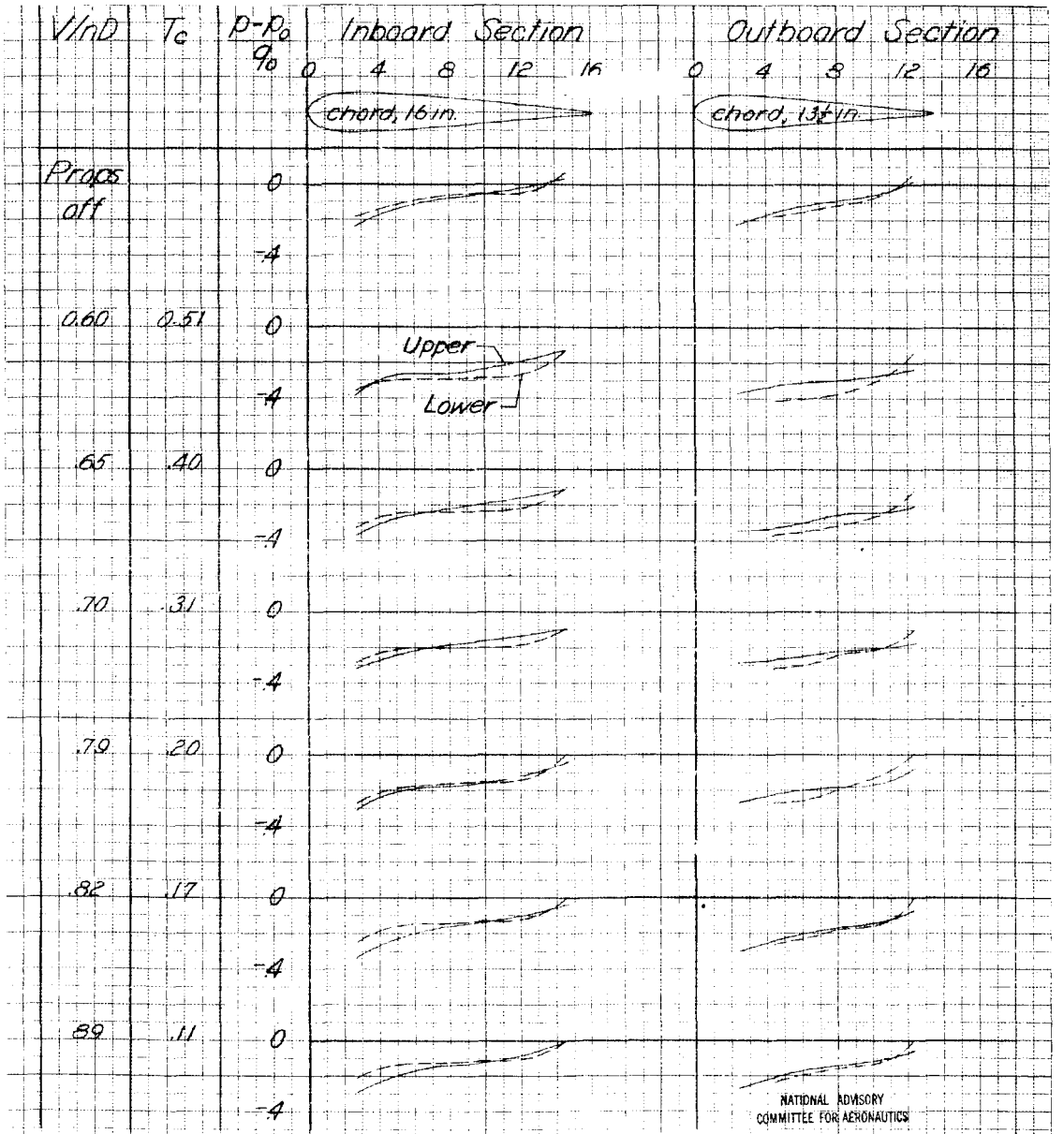

(a) $\delta_e = 0°$.

Figure 36.- Pressure distribution on the left elevator in positive thrust. Tail surfaces in position 4; $\beta_F = 20°$; $\beta_R = 19.9°$; $\alpha = 0°$; $\delta_r = 0°$.

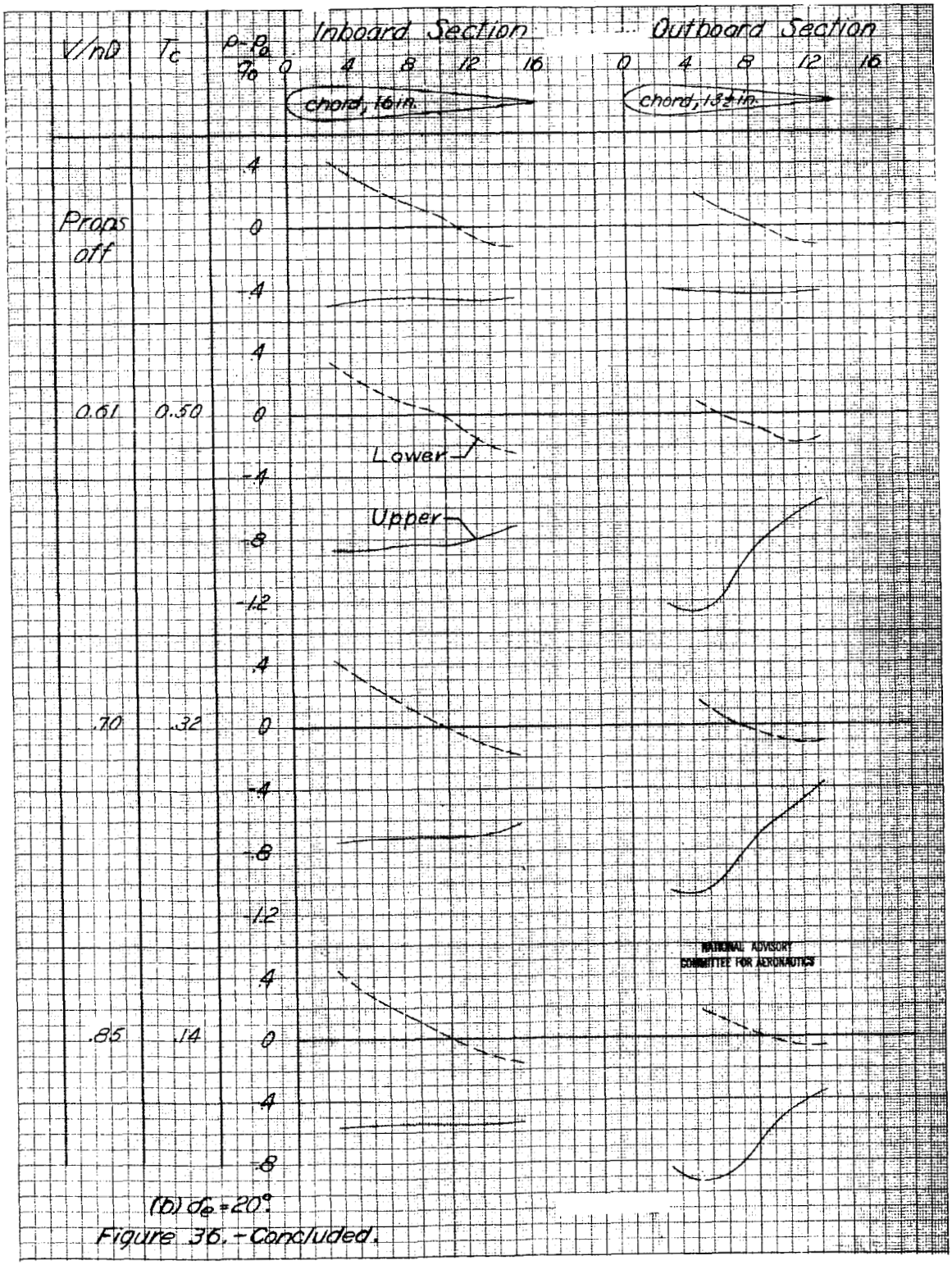

(b) $\delta_e = 20°$

Figure 36.- Concluded.

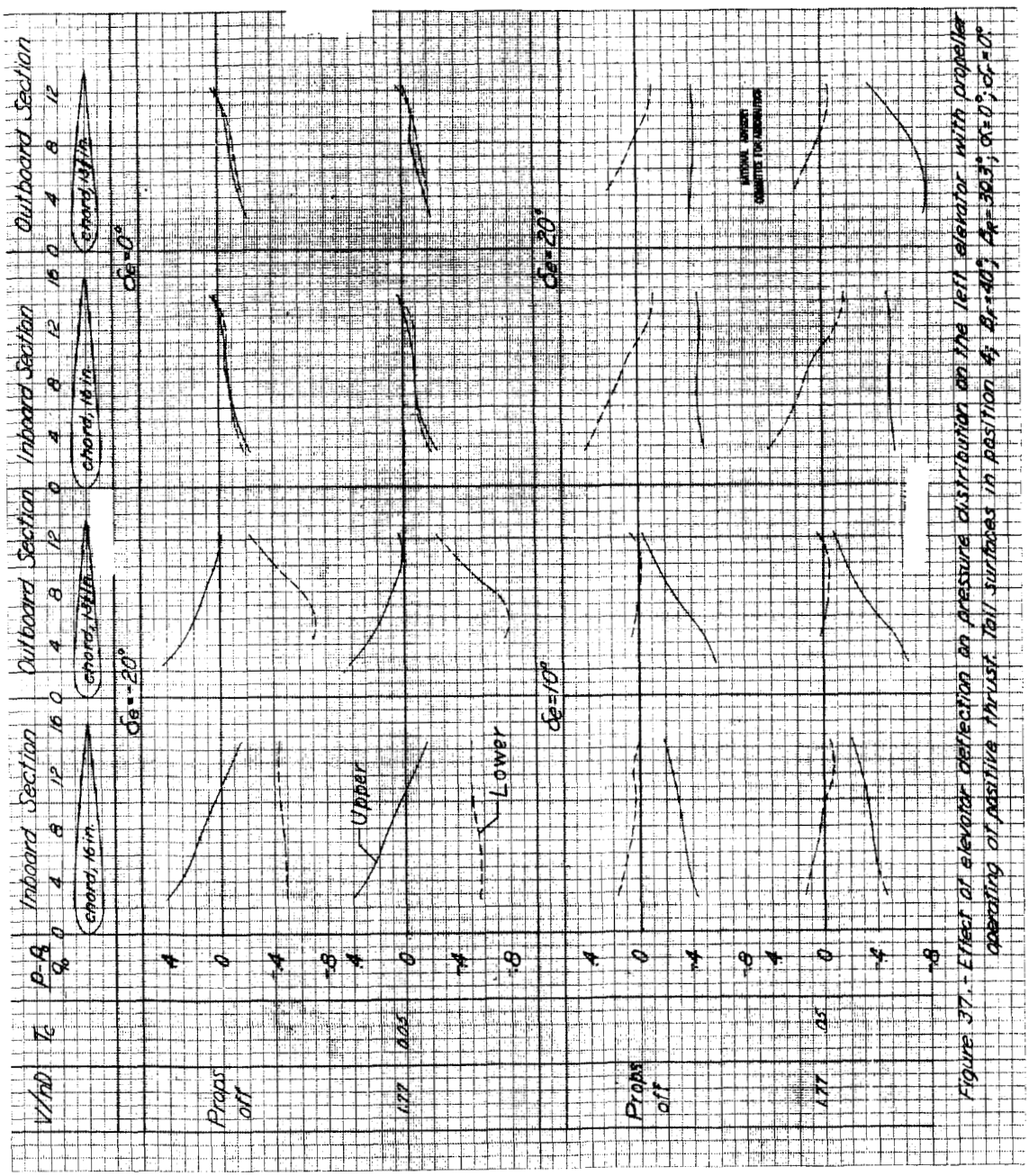

Figure 37.- Effect of elevator deflection on pressure distribution on the left elevator with propeller operating at positive thrust. Tail surfaces in position 4; i_t=-40°; i_p=-30.3°; α=0°; α_c=0°.

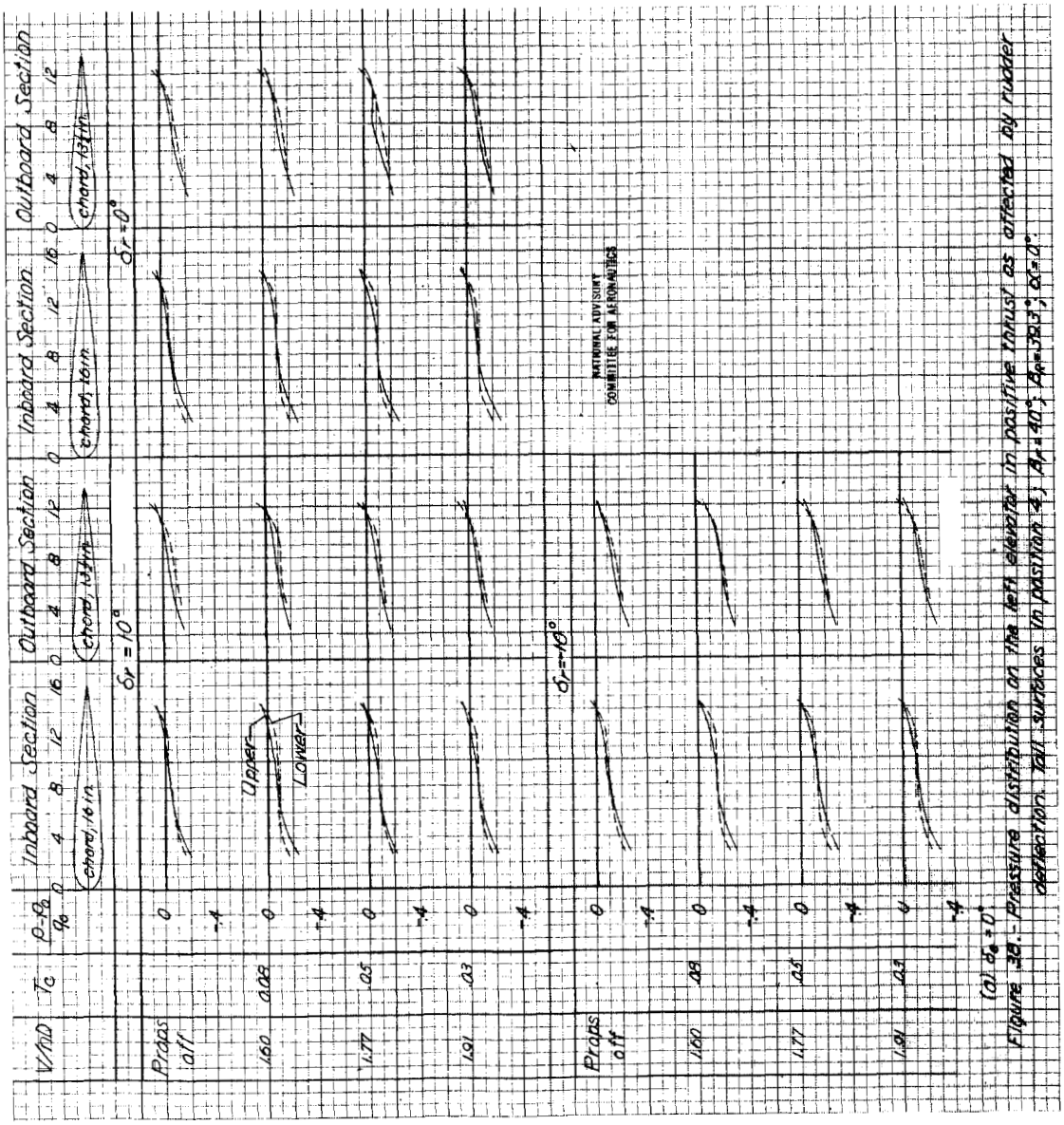

Figure 38.- Pressure distribution on the left elevator in positive thrust as affected by rudder deflection. Tail surfaces in position 4; i_t = 40°; i_w = 3.3°; α_c = 0°.

(a) α_c = 0°.

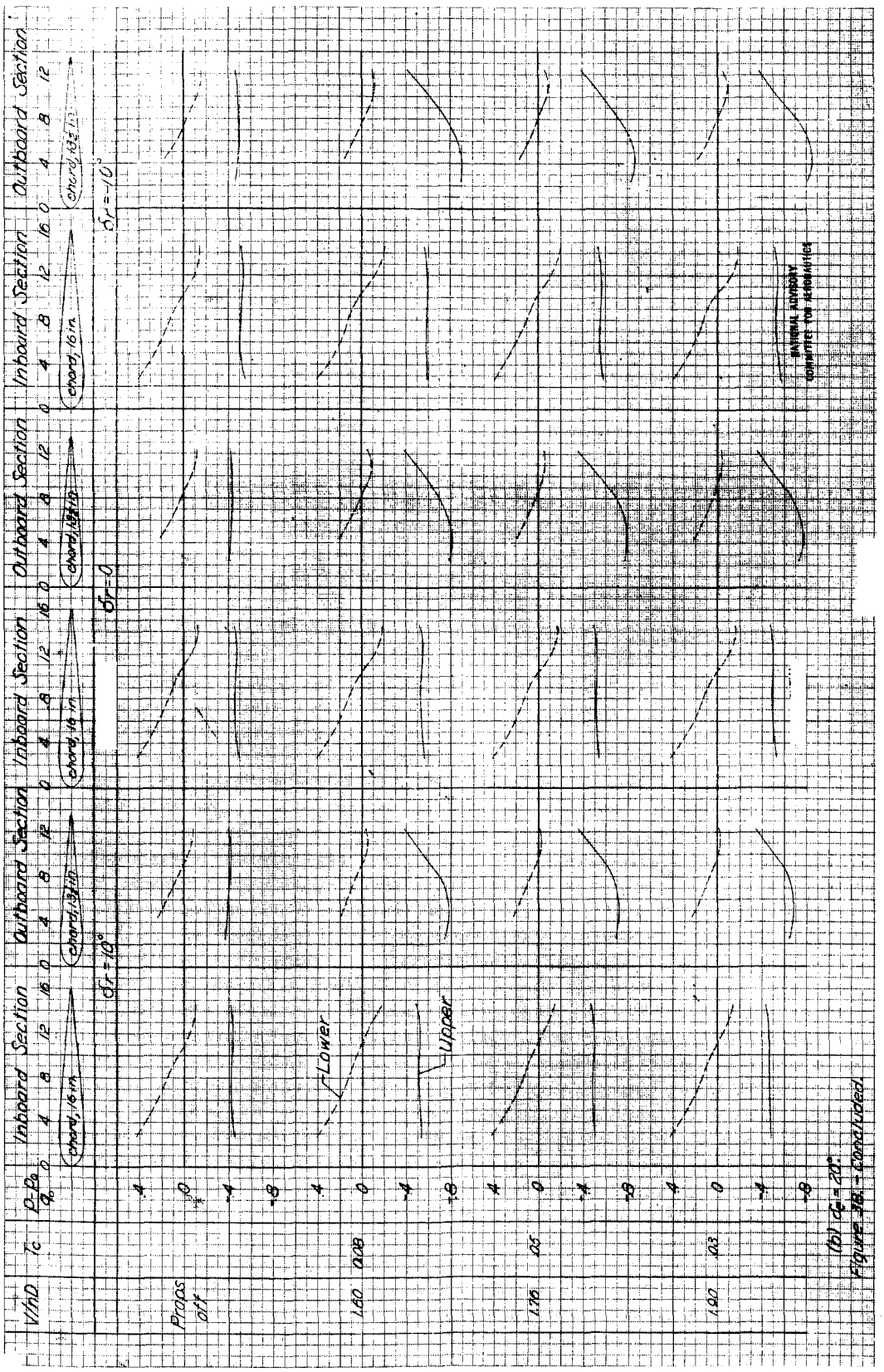

Figure 16.- Concluded.

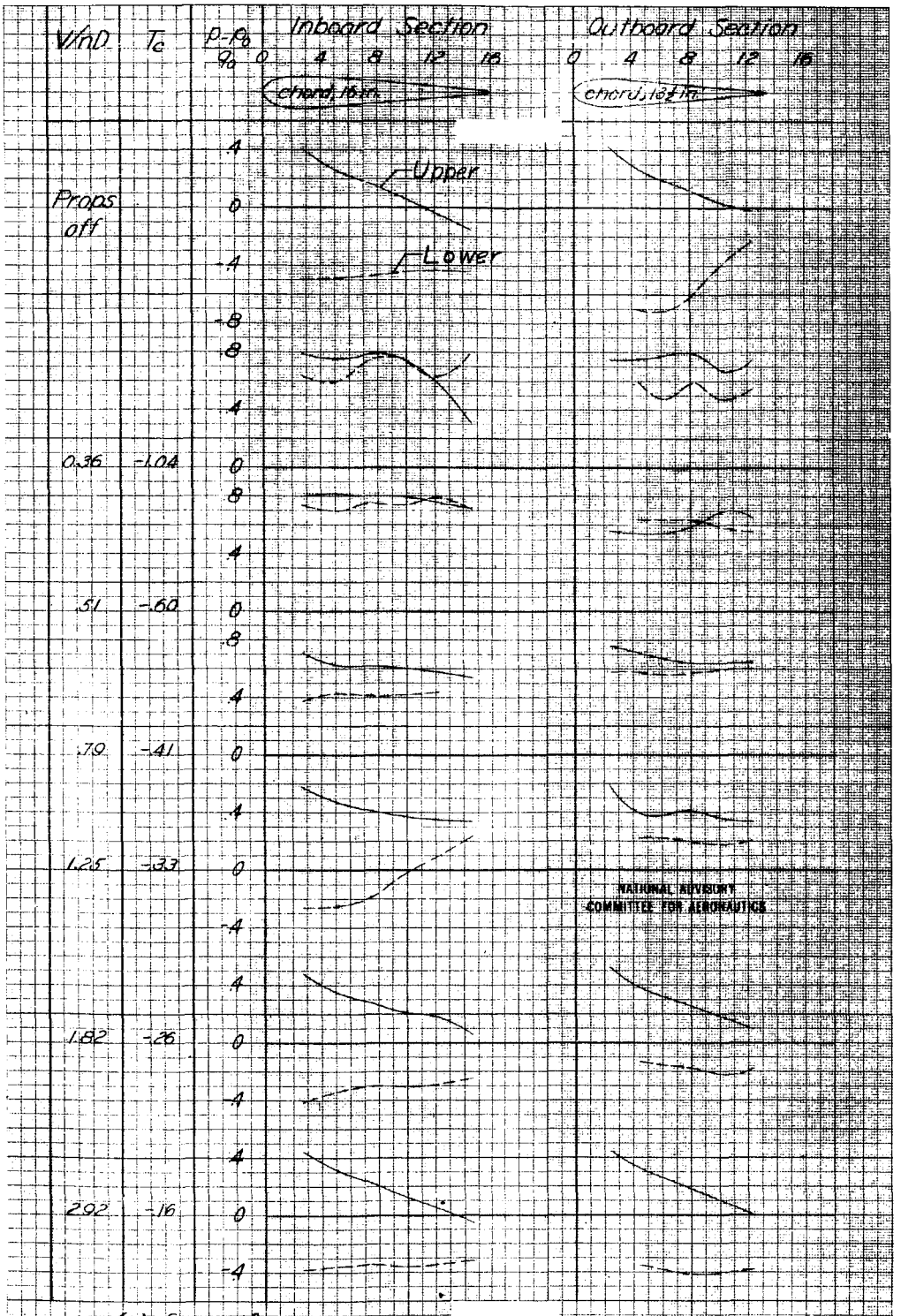

(a) $\delta_e = -20°$.

Figure 39.- Pressure distribution on the left elevator with propeller operating at negative thrust. Tail surfaces in position 4; $\beta_T = \beta_{RP} = -15°$; $\alpha = 0°$; $\delta_r = 0°$.

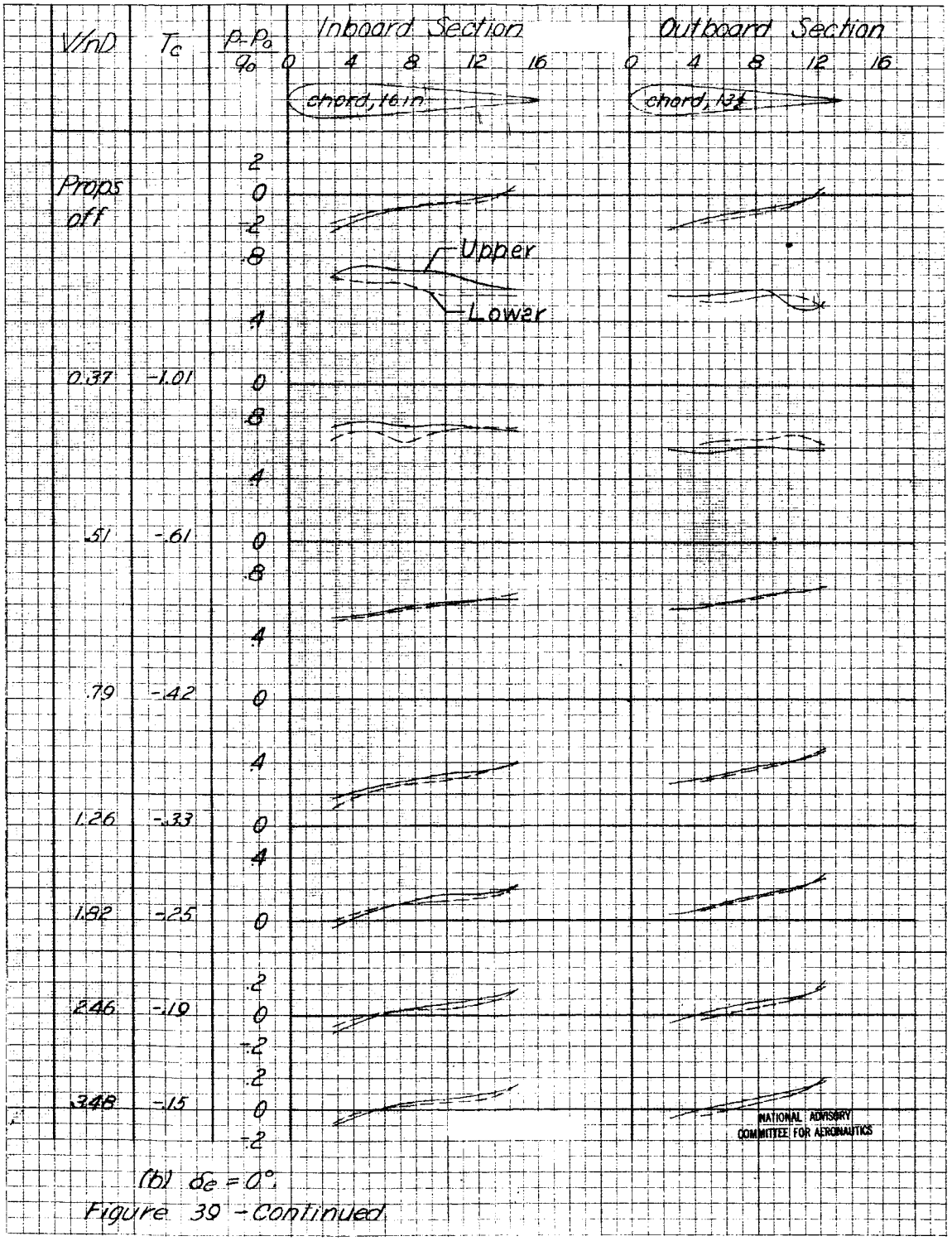

(b) $\delta_e = 0°$

Figure 39 - Continued

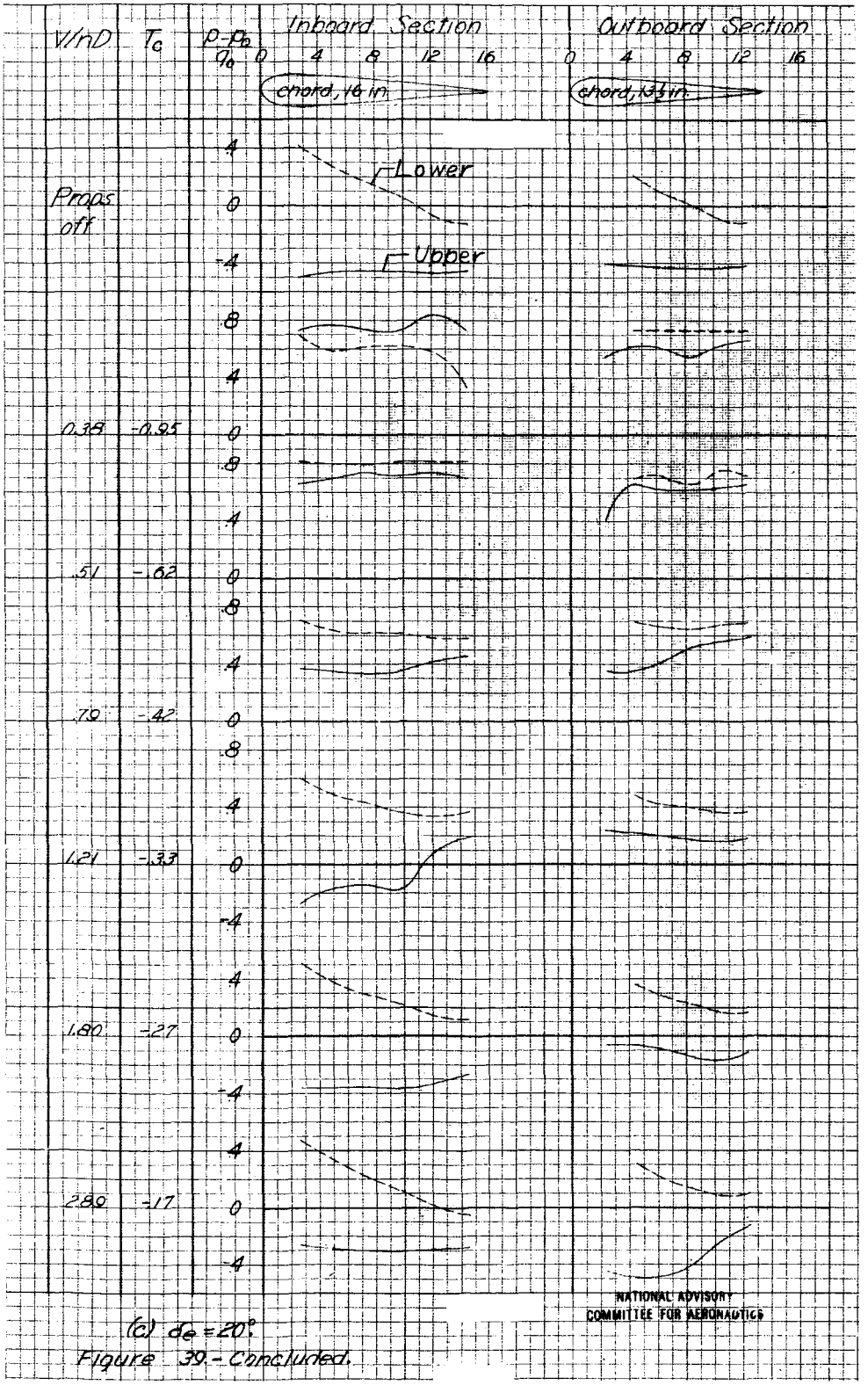

(c) $d_e = 20°$.

Figure 39.- Concluded.

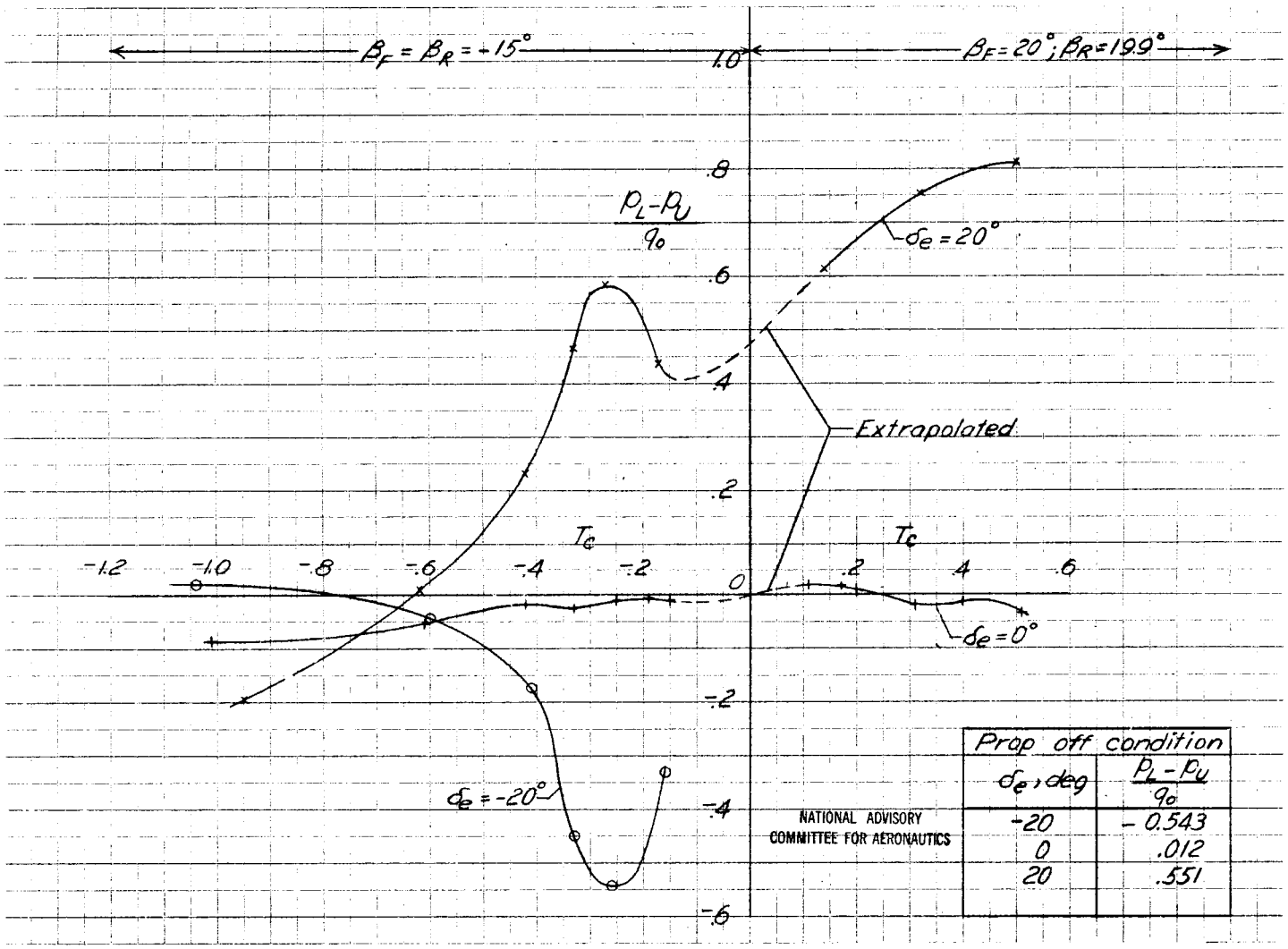

Prop off condition	
δ_e, deg	$\frac{p_L - p_U}{q_0}$
-20	- 0.543
0	.012
20	.551

Figure 40.- Loading on left elevator at the inboard pressure belt for several elevator deflections in both positive and negative thrust.

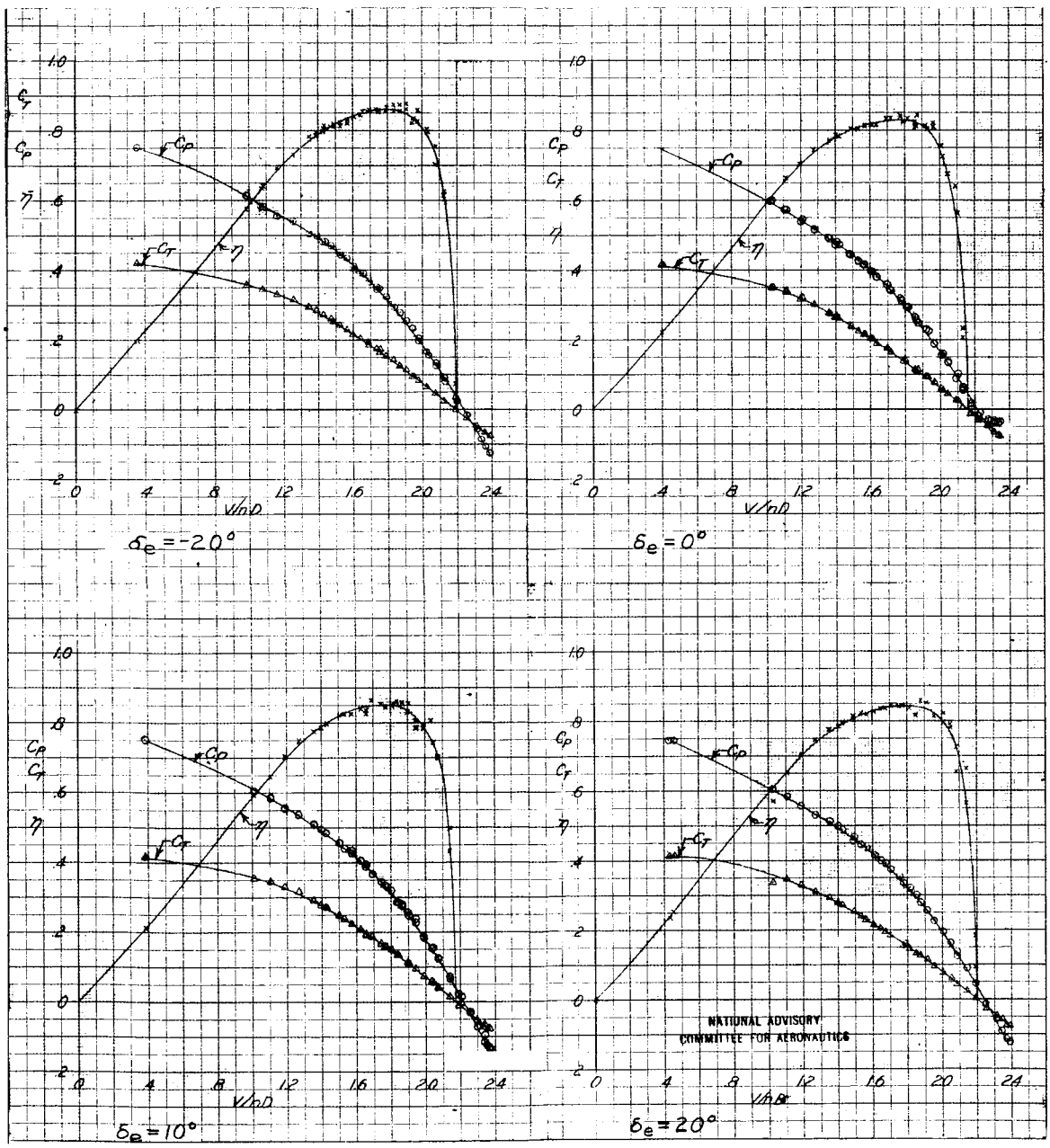

Figure 41.- Aerodynamic characteristics of the six-blade dual-rotating propeller at several elevator deflections. Tail surfaces in position 4; $\beta_F = 40°$; $\beta_R = 39.3°$; $\alpha = 0°$; $\delta_f = 0°$.

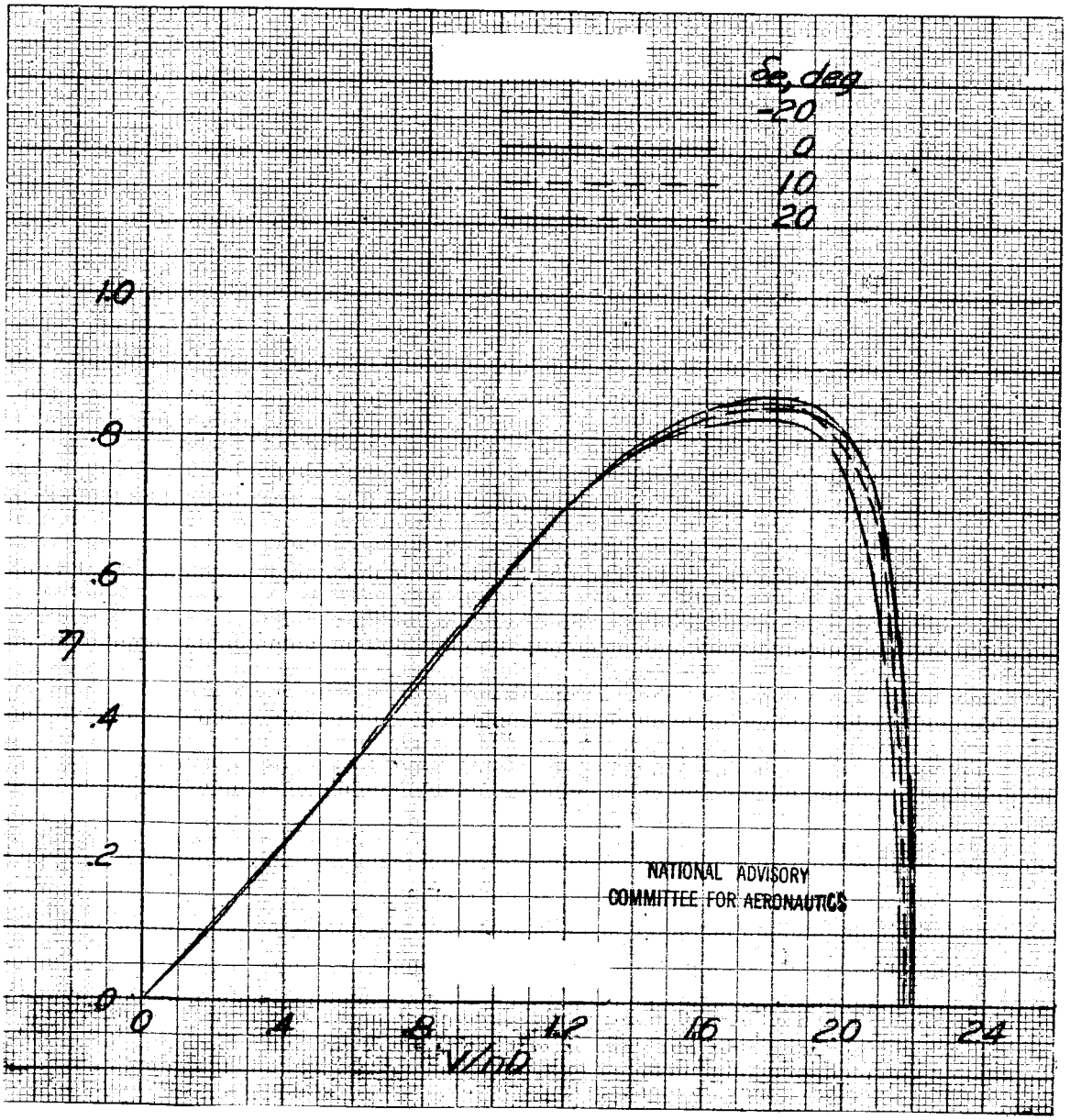

Figure 42.- Effect of elevator deflection on the propulsive efficiency. Tail surfaces in position 4; $\beta_F = 40^\circ$; $\beta_R = 39.3^\circ$; $\alpha = 0^\circ$; $\delta_T = 0^\circ$.

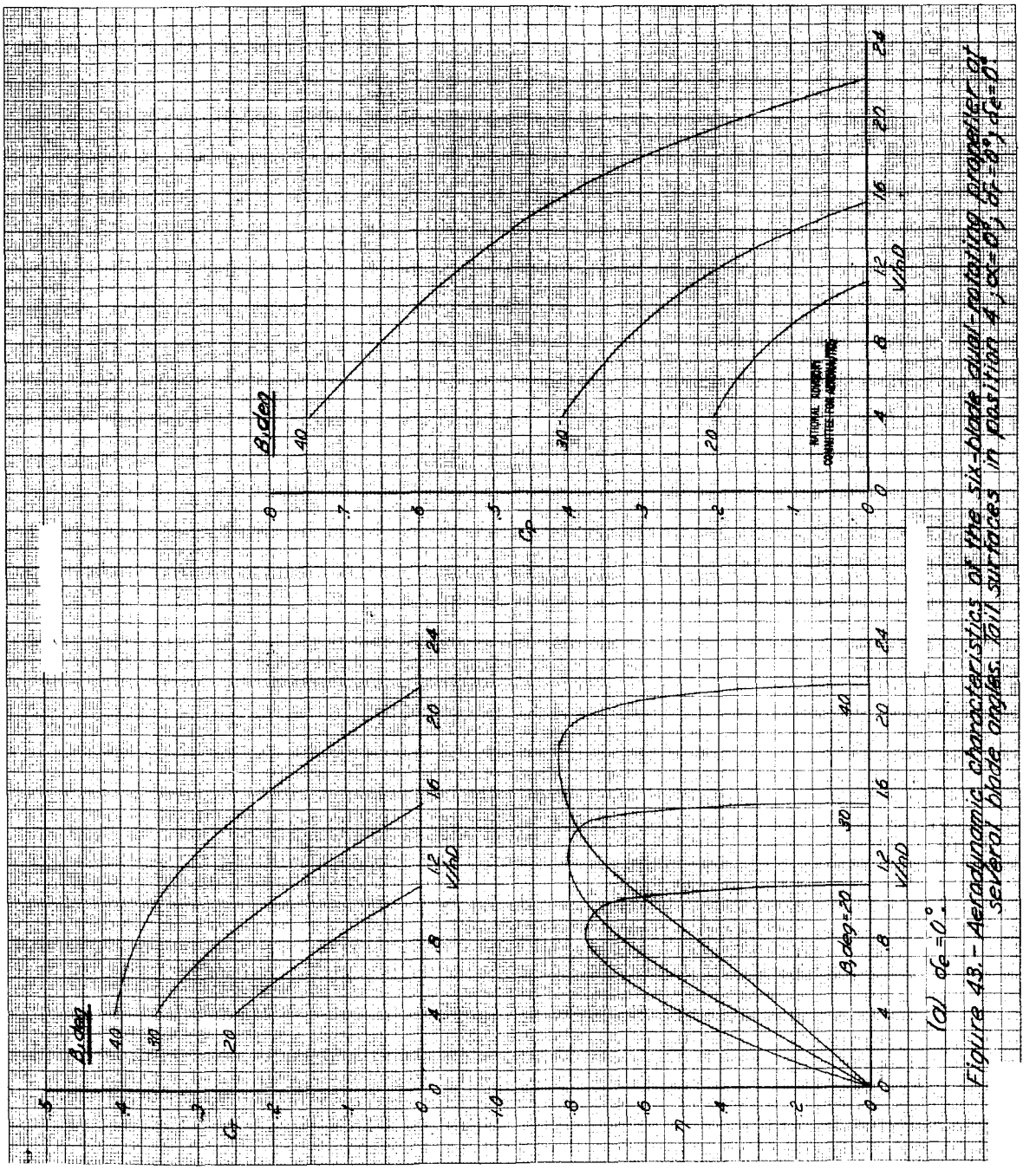

Figure 43.- Aerodynamic characteristics of the six-blade quadrirotating propeller of several blade angles. Tail surfaces in position 4; $i_x=0°$; $\delta_e=0°$; $\delta_r=0°$.

(a) $\alpha_s=0°$.

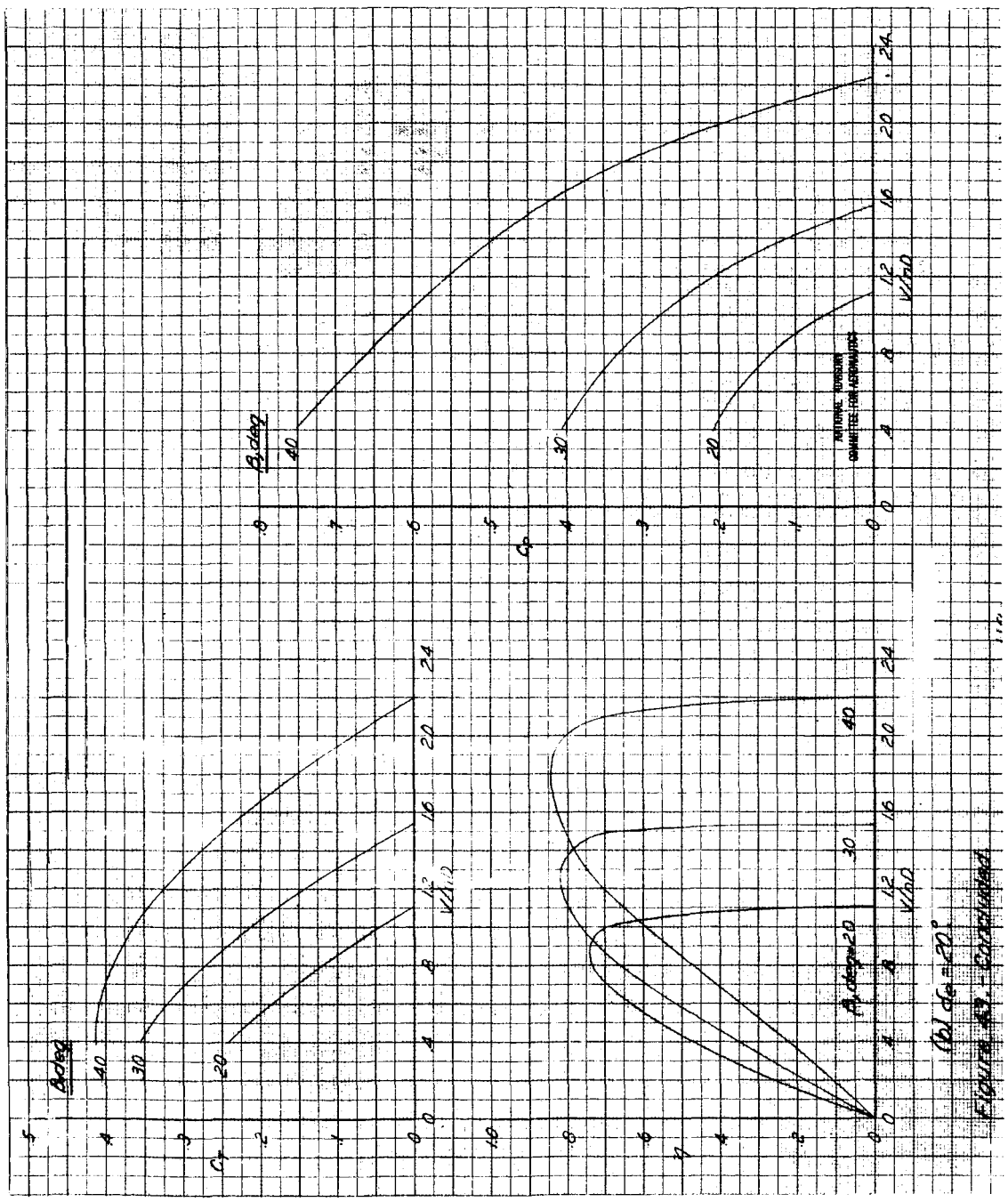
NATIONAL ADVISORY COMMITTEE FOR AERONAUTICS
Figure 13.- Concluded.

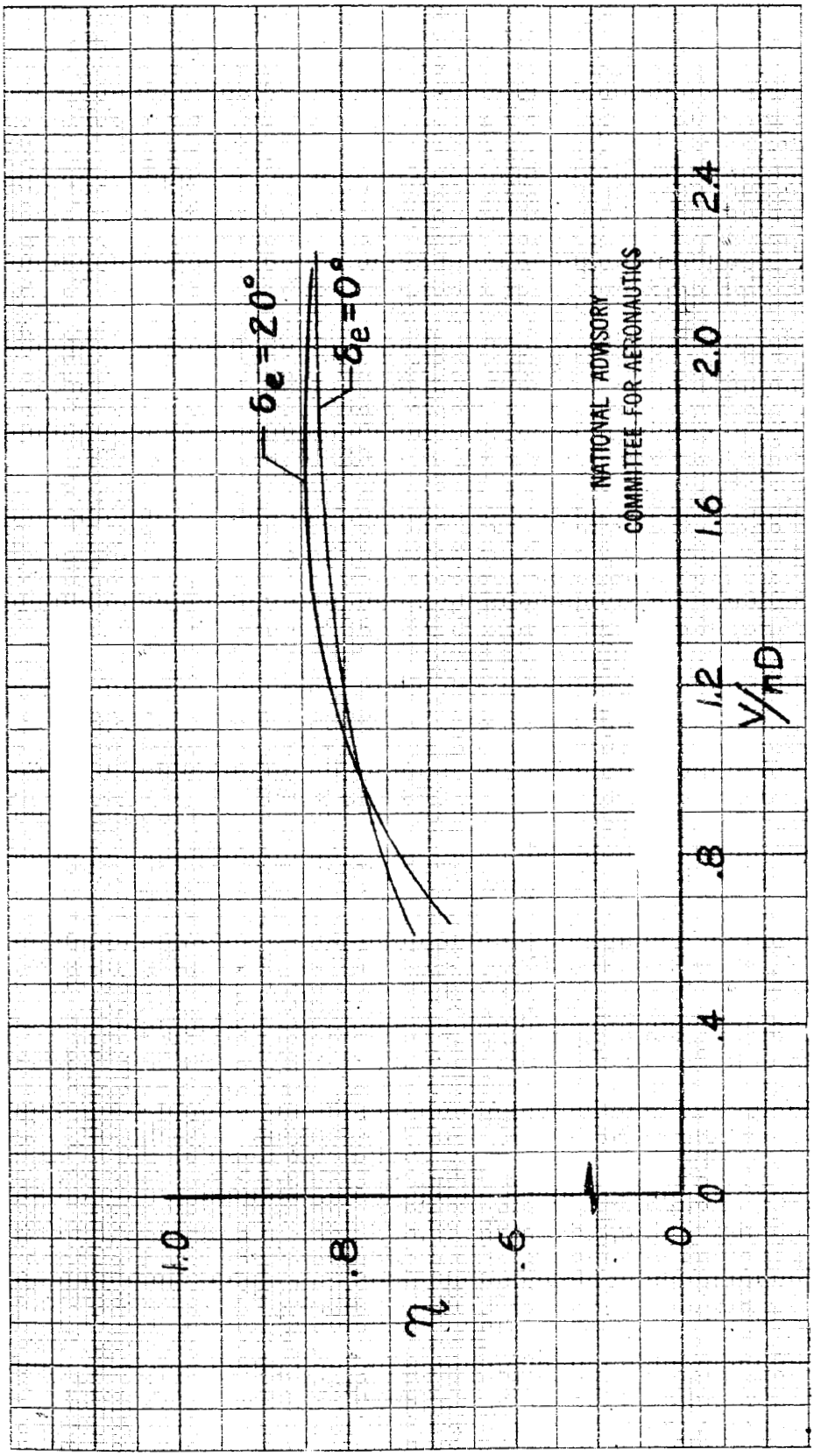

Figure 44.- The effect of elevator deflection upon the efficiency envelopes of the six-blade dual-rotating propeller. Tail surfaces in position 4; $\alpha = 0°$; $\delta_r = 0°$.

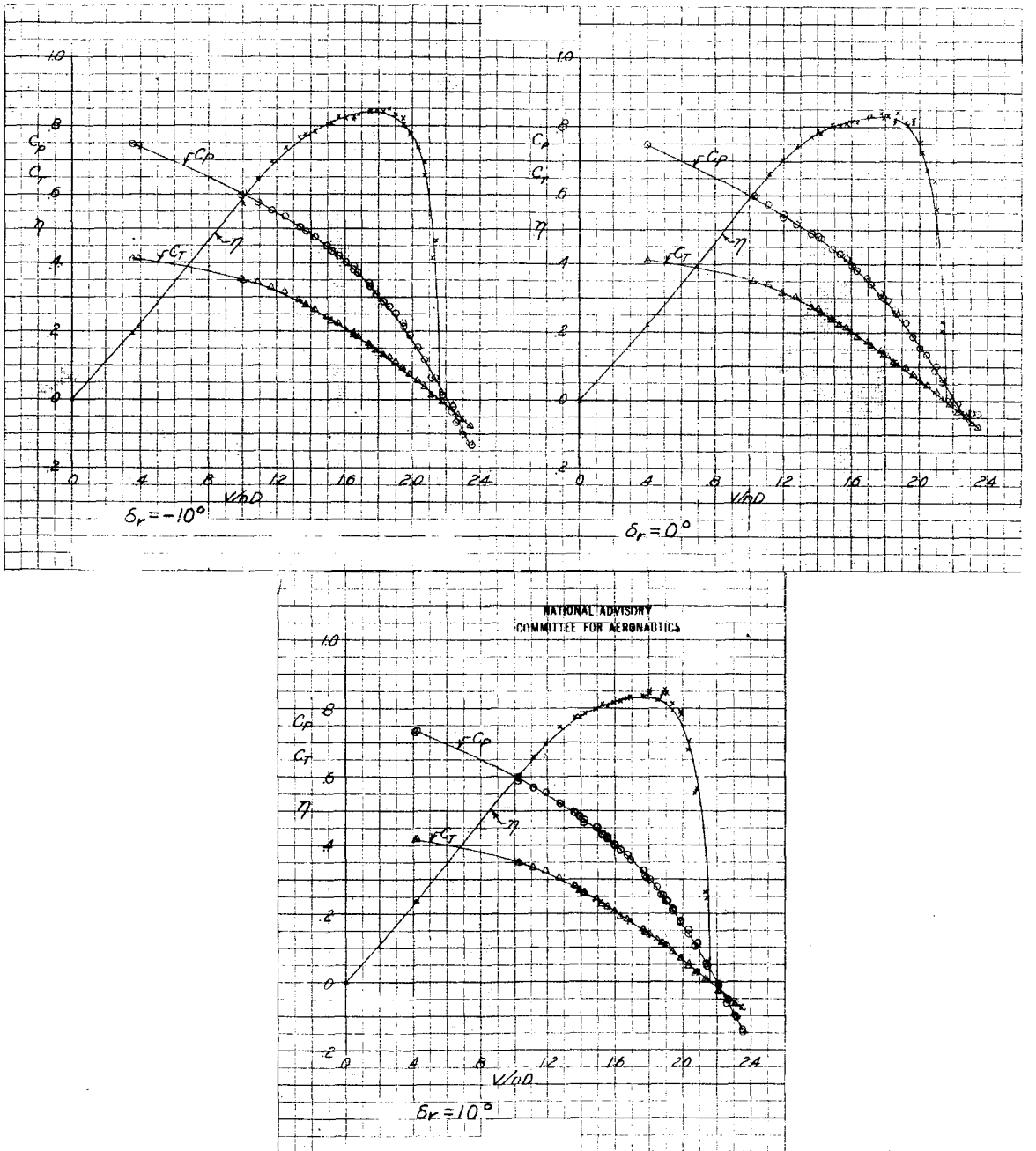

Figure 45.- Aerodynamic characteristics of the six-blade dual-rotating propeller at several rudder deflections. Tail surfaces in position 4; $\beta_F = 40°$; $\beta_R = 39.3°$; $\alpha = 0°$; $\delta_f = 0°$.

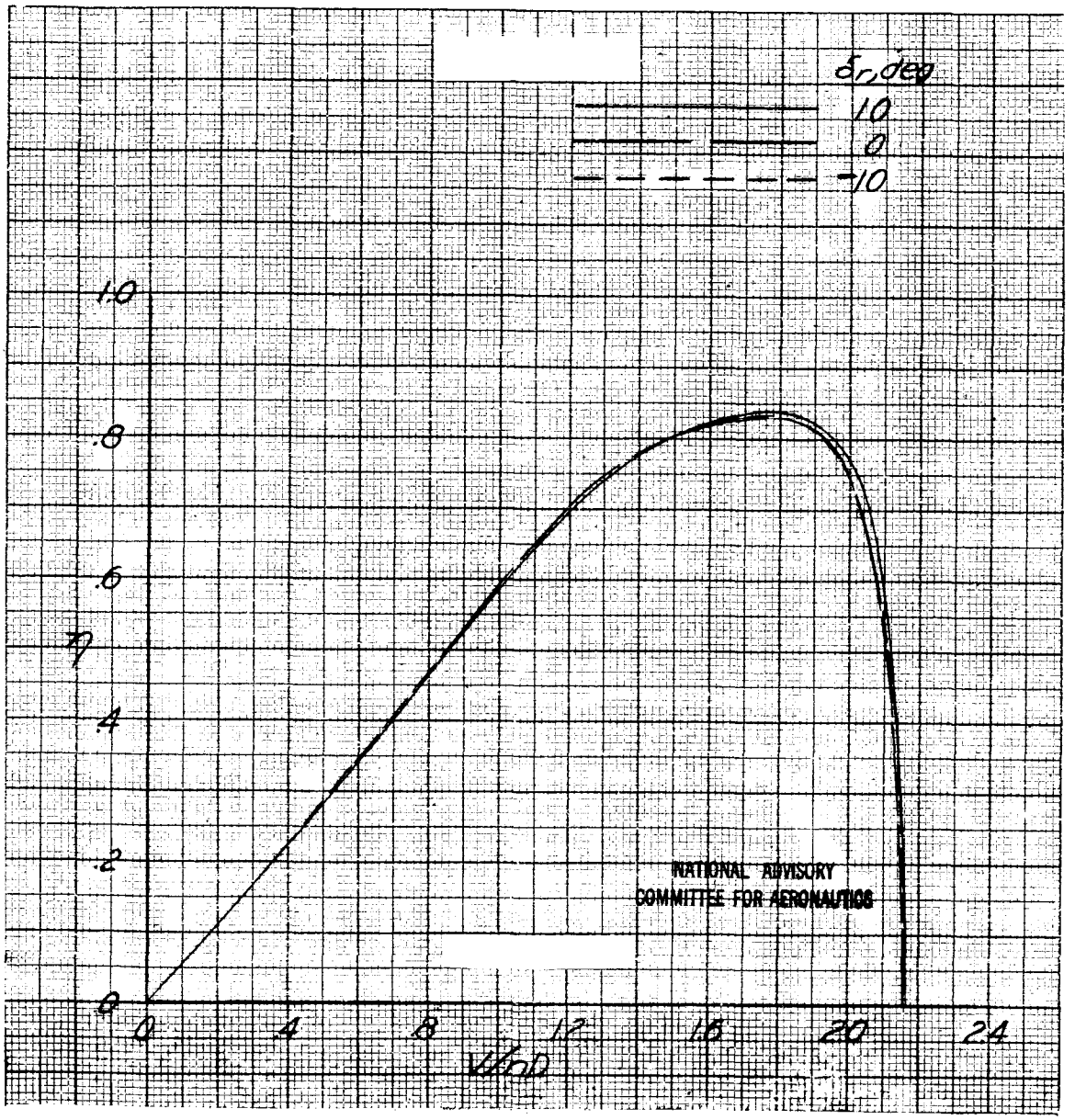

Figure 46.- Effect of rudder deflection on the propulsive efficiency. Tail surfaces in position 4; $\beta_F = 40^\circ$; $\beta_R = 39.3^\circ$; $\alpha = 0^\circ$; $\delta_e = 0^\circ$.

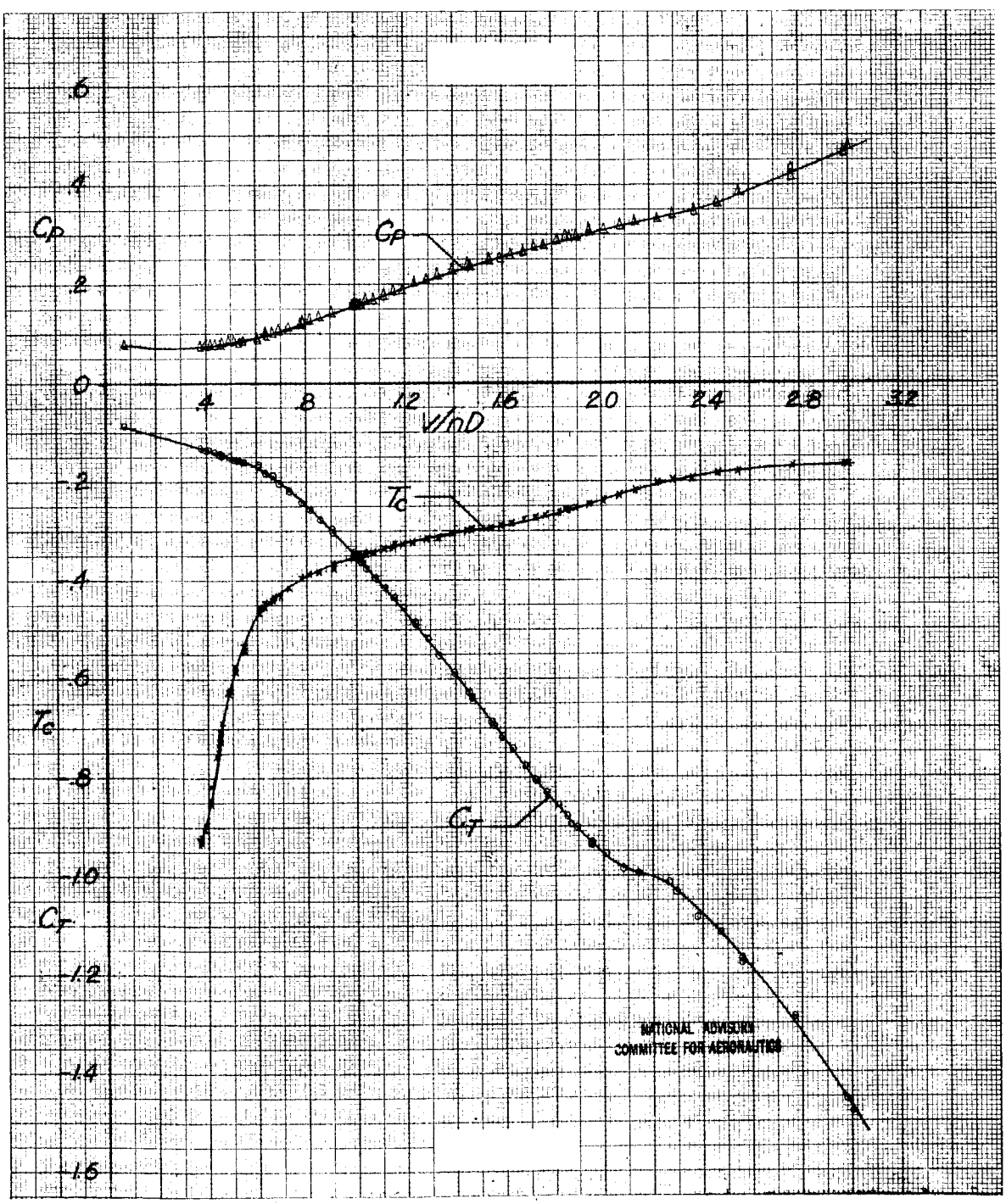

Figure 47 - Negative thrust characteristics of the six-blade dual-rotating propeller. Tail surfaces in position 4; $\beta_F = \beta_R = -15^\circ$; $\alpha = 0.4^\circ$; $\delta_e = 0^\circ$; $\delta_r = 0^\circ$.

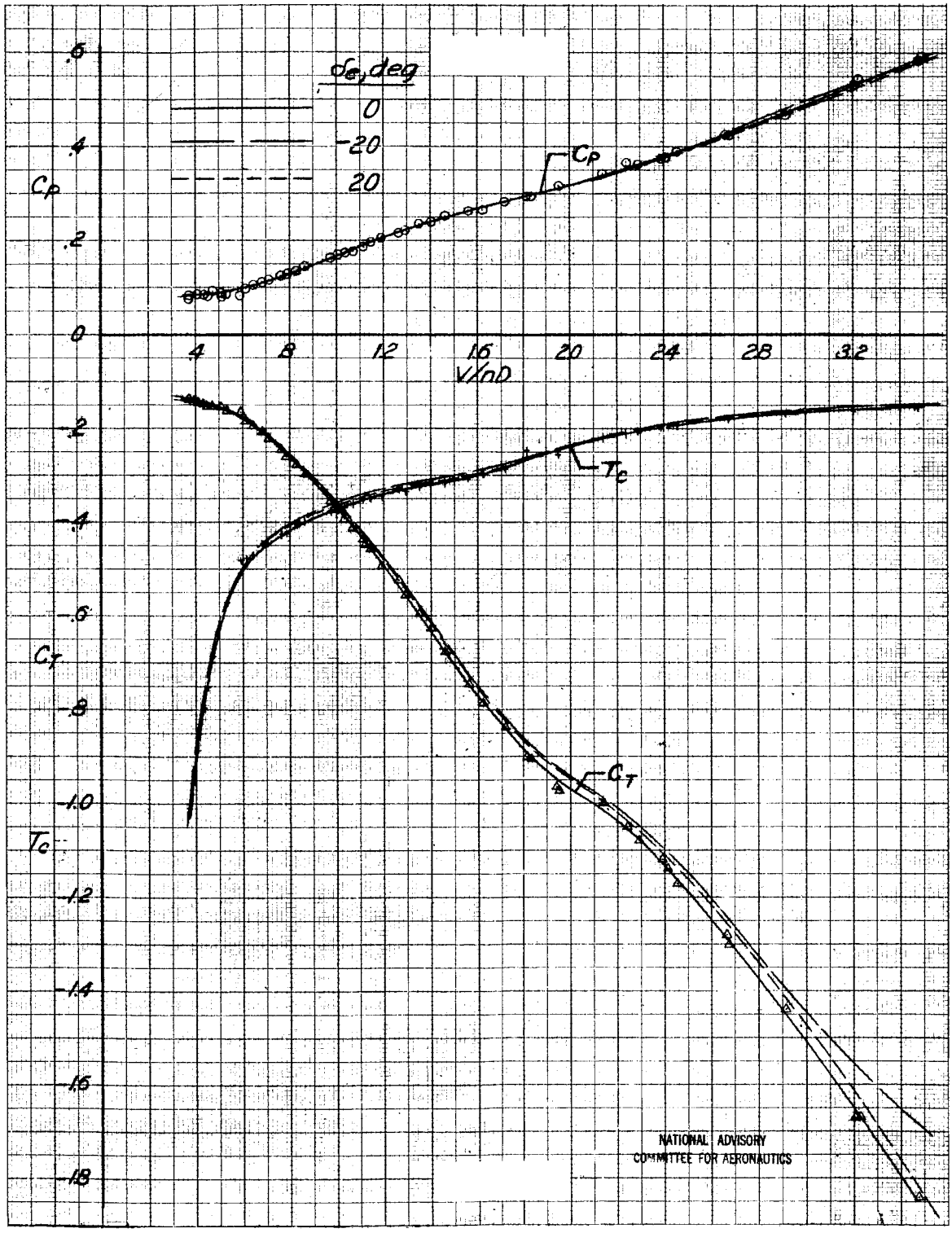

Figure 48.- Negative thrust characteristics of the six-blade dual-rotating propeller as influenced by elevator deflection. Tail surfaces in position 4; $\beta_F = \beta_R = -15°$; $\alpha = 0°$; $\delta_r = 0°$.